DISSERTATION APPROVAL

The abstract and dissertation of HanQun Shangguan for the Doctor of Philosophy in Electrical and Computer Engineering were presented November 15, 1996, and accepted by the dissertation committee and the doctoral program.

COMMITTEE APPROVALS:

Lee W. Casperson, Chair

Scott A. Prahl

W. Robert Daasch

Carl G. Bachhuber

Bradford R. Crain
Representative of the Office of Graduate Studies

DOCTORAL PROGRAM APPROVAL:

Rolf Schaumann, Chair
Department of Electrical Engineering

****

ACCEPTED FOR PORTLAND STATE UNIVERSITY BY THE LIBRARY

by _____ on _____

ABSTRACT

An abstract of the dissertation of HanQun Shangguan for the Doctor of Philosophy in Electrical and Computer Engineering presented November 15, 1996.

Title: Local Drug Delivery with Microsecond Laser Pulses: *In vitro* Studies

Photomechanical drug delivery is a technique for localized drug delivery using laser-induced hydrodynamic pressure following cavitation bubble expansion and collapse. This dissertation presents *in vitro* studies of photomechanical drug delivery. The main goals were investigate the possibility of photomechanical drug delivery as a new means of localized drug delivery to thrombus for enhancement of laser thrombolysis and to address some of the questions regarding the physical processes during photomechanical drug delivery.

A parametric study was performed to characterize laser-induced cavitation phenomena that take place in absorbing liquids or on soft targets using time-resolved flash photography, high-speed shadowgraphy, particle image velocimetry. The laser-induced cavitation bubble dynamics depended where the bubble was formed. The bubble expansion and collapse could cause the surrounding flow motion at a speed of up to 12 m/s. A theoretical model was used to estimate the bubble volumes formed in absorbing liquids. This model assumed vaporization of the entire disk of absorbing liquids under a delivery fiber, rather than vaporization

of a fraction of the disk. Good agreement was found between the model and experimental results.

Photomechanical drug delivery into soft materials (gelatin or thrombus) were studied using solutions of oil and dye or 1 μm fluorescent microspheres. The drug could be driven into thrombus several hundred micrometers and even few millimeters in both axial and radial directions when the gelatin structures were fractured. The results of using thrombus phantoms were comparable to those obtained using porcine clots. The cavitation bubble formation is the governing mechanism for photomechanical drug delivery.

The ablation process is profoundly affected by whether the optical fiber tip is inside a catheter or is in contact with the thrombus when the laser light is delivered through an optical fiber to the thrombus. The contact ablation efficiency of porcine clot was at least three times greater than the non-contact ablation efficiency. The mass ablated was correlated with the expansion pressure of the cavitation bubble. The fluorescent microspheres penetrated the mural clot the same distance for both ablation methods. The kinetic energy generation depended on the total delivered energy regardless of the light delivery methods.

LOCAL DRUG DELIVERY WITH MICROSECOND LASER PULSES: *IN VITRO* STUDIES

by

HanQun Shangguan

A dissertation submitted in partial fulfillment of the
requirements for the degree
Doctor of Philosophy
in
Electrical and Computer Engineering

Portland State University
1996

Acknowledgements

I would like to express my appreciation to my advisor, Dr. Lee W. Casperson who taught me much about lasers and optical systems, whose many excellent questions helped me focus this project. I appreciate his supervision, motivation, and instruction through my graduate studies at Portland State University. He is always very kind to me whenever I needed help.

I would next like to thank Dr. Scott A. Prahl, my second advisor. It would have been impossible for me to finish my studies for Ph.D. in the biomedical field without his ideas and encouragement.

I extend appreciation to Dr. Kenton W. Gregory, the director of Oregon Medical Laser Center, who has provided me with the excellent opportunity to study and work at the center. I would not have been able to achieve so much on this project without his great help.

I thank the members of my dissertation committee, Drs. W. Robert Daasch, Carl G. Bachhuber, and Bradford R. Crain, for their guidance and valuable comments on this dissertation.

My special thanks go to the other members of the "Gregory Team", Dr. Steven L. Jacques, Lisa Buckley, Deb Tuke-Bahlman, Karen Elings, and Ursula

Gilliam for their hospitality, encouragement, and the pleasure we shared at the center; to Alan Shearin for his generous support during this project; to my other fellow graduate students Elaine, Ujwal, Krishna, Sean, Scott, Badri, and John for sharing the experience under Dr. Prahl's supervision.

To Shirley Clark and Laura Riddell of the Electrical Engineering Department staff, my thanks for the many ways they have helped me during my studies.

I gratefully acknowledge the financial support from the Whitaker Foundation and The Murdock Trust.

My sincere thanks to all my family who have supported me spiritually and financially for years.

A heartfelt thank you to my wife, Zhenghong Zhu, for supporting me along the way, willingly sharing the frustrations and exultation of my graduate career, and staying with me. Finally, I thank my daughter, Shirley, for her support, understanding, and her many phone calls during this long trek.

Contents

List of Tables

List of Figures

Chapter 1

Introduction

1.1 Motivation

Laser thrombolysis is an interventional procedure to remove thrombus (blood clot) in occluded arteries using laser energy [1]. One concern for laser thrombolysis is the mural thrombus left after the laser thrombolysis procedure, which may be a potential limitation for this therapy. The research presented in this dissertation was initially motivated by the need for methods to enhance the efficacy and rate of laser thrombolysis.

It was proposed that localized pressure transients generated through laser-induced cavitation or vapor bubble formation may be used to drive drugs into thrombi or vessel walls for the enhancement of laser thrombolysis. The localized delivery of fibrinolytic drugs would be of particular value in enhancing laser thrombolysis in cases with large volumes of thrombus in large vessels such as bypass grafts or peripheral vessels. This potential therapy was initially termed

photoacoustic drug delivery [2]. It was changed to photomechanical drug delivery during the course of this study for three reasons. First, this study showed that the drug was most likely driven by photomechanical effects associated with hydrodynamic flows accompanying bubble expansion and collapse. Second, photomechanical drug delivery should be differentiated from therapies that are actually mediated by acoustic events (laser-induced shockwaves). Third, the acoustic events rapidly propagate through the medium and there is essentially no drug movement during this short time.

In vitro studies would provide basic parameters required before the feasibility, efficacy, and safety of photomechanical drug delivery can be studied in animal and human trials. This research addresses some of the questions regarding the physical processes during photomechanical drug delivery. Knowledge of the basic science involved in these processes is important for understanding photomechanical drug delivery and may make it possible to specify optimal laser parameters for the design of the laser and localized drug delivery systems.

1.2 Research Goals

The global goal of this research is to investigate the possibility of photomechanical drug delivery as a new means of localized drug delivery to thrombus. More specifically, the goals of this research can be divided into three broad categories: First, to characterize laser-induced cavitation phenomena that take place

during photomechanical drug delivery. Next, to identify the mechanisms of photomechanical drug delivery. Finally, to study the effects of contact and non-contact delivery on laser thrombolysis, drug delivery, and kinetic energy generation. To eliminate the biological variation of real thrombus, most experimental work presented here is done on gelatin-based thrombus models. The process of photomechanical drug delivery is studied experimentally and the results are related to theoretical concepts.

1.3 Outline

Following this introduction, this manuscript includes nine chapters. Each chapter deals with a different topic and is relatively independent from others. Most of the chapters have been partially published or presented at conferences [2–10]. They are written in a sequence starting with the background of this study, basic investigations of laser-induced cavitation events, and then applicabilities of these cavitation effects on localized drug delivery. Many supporting experiments have been performed.

Chapter 2 provides a historical background on current therapies for thrombosis in vascular systems and its limitations. A potential therapy–photomechanical drug delivery is introduced.

The topics on characterization of cavitation phenomena that take place in liquids and on soft targets are presented in Chapters 3–5. The experiments are done in a parametric way, where the parameters are the absorption coefficient,

radiant exposure, and the effects of material and boundaries. Several photography techniques such as time-resolved flash photography, high-speed photography, and particle image velocimetry are used for visualizing the cavitation events, and laser-induced acoustic pressure waves were measured using an acoustic transducer.

Chapters 6 and 7 describe a series of experiments for investigating the possibility of photomechanical drug delivery as a new means of localized drug delivery to thrombus. Solutions of oil-dye and 1 μm fluorescent spheres are used as drug models. The presence of the dye or the spheres in the thrombus phantoms simulates the photomechanically delivered drug in thrombus. These studies have provided the proof of principle of photomechanical drug delivery as a new means of localized drug delivery to thrombus.

The effects of contact and non-contact delivery on laser thrombolysis, drug delivery, and kinetic energy generation are described in Chapters 8 and 9. The results demonstrate that the ablation process is profoundly affected by these two modalities, which should be taken into consideration in clinical applications.

Chapter 10 summarizes the most important observations, conclusions, and implications regarding the mechanisms involved in the process of photomechanical drug delivery.

Chapter 2

Background

2.1 The Clinical Problems

Blood clotting is an essential protective mechanism that can prevent external and internal bleeding. However, in certain circumstances this normal homeostatic defense may be exaggerated so that unwanted clotting occurs *in vivo* [11]. Thrombosis and embolism within the cardiovascular system may be life-threatening and cause cardiovascular diseases such as heart attacks and strokes. For example, when a blood clot (thrombus) suddenly develops in one of the heart's arteries, cutting off blood flow and oxygen to part of the heart, a heart attack (myocardial infarction) occurs. Permanent damage to the heart muscle begins within minutes of arterial closure. If a clot forms in a narrowed brain vessel or if emboli (fragments of plaque or blood clots) that break off from the places where they form flow downstream where they plug smaller arteries, a stroke will be initiated. The term "stroke" is used to describe a number of brain disorders with the common feature of an abnormality of the brain's vasculature. Usually, strokes are focal

areas of brain damage, some only a few millimeters in diameter, some destroying a whole hemisphere of the brain.

Heart attack, caused by blood clots in coronary arteries, is the most common cause of death in the United States. Over 1.5 million people suffer from heart attacks annually and approximately 500,000 will die as a consequences [12, 13]. Stroke, brain attack, ranks close behind heart disease and cancer as a leading killer (approximately 200,000 deaths yearly) and leads all other diseases in disabling Americans [11].

Blood clot formation is a fundamental problem in many other life threatening conditions, and the unwanted clotting can occur in any diseased arteries or veins and even healthy vessels as well. The fatal occlusions can cut off the blood supply to vital organs and stop their functions. The importance of thromboembolic disorders as a major cause of morbidity and mortality has been gaining attention in the past two decades [11].

2.2 Current Therapies

The best medicine for vascular diseases is often a change in behavior. A healthy lifestyle is the first line of defense against vascular diseases. Controlling blood pressure, lowering the level of cholesterol in the blood, and quitting smoking can significantly increase the odds of preventing the diseases or at least reduce the progression of the diseases. But for some people the risk of vascular diseases is already too high. The arteries that supply blood to some vital organs have become clogged with plaque and special treatments are necessary.

Thrombolytic therapy intends to restore circulation through a previously occluded vessel by injecting clot-dissolving drugs such as streptokinase and urokinase. All the thrombolytic agents currently in use or under development act directly or indirectly as plasminogen activators [14]. Basically, these drugs convert plasminogen to plasmin. Plasmin proteolytically degrades the fibrin of the blood clot leading to thrombolysis. However, all these drugs can cause severe bleeding complications and strokes, and almost half the time the drugs fail to dissolve the clot. Medication provides another option to try to prevent clots from forming within the arteries or keep clots from enlarging. Antiplatelet medications such as aspirin suppress the platelets in blood that initiate clotting. But they are not effective, except in special circumstances.

An interventional procedure called balloon angioplasty (e.g., percutaneous transluminal coronary angioplasty–PTCA) has become an accepted therapeutic option for the treatment of obstructive vascular disease. No surgery is necessary, and only a local anesthetic is used. In balloon angioplasty, a balloon at the site of stenosis is inflated to stretch the narrowed artery. Unfortunately, this overstretching induces mechanical injuries to the vessel wall such as intimal flaps and dissection, and results in restenosis of vascular lesion, i.e., the blockage recurs. A repeat angioplasty is needed. Recent studies describe restenosis rates ranging from 30% to 40% within six months of the procedure [15]. The process of restenosis following vascular injury may also serve as a paradigm for atherosclerosis (the buildup of fat within the lining of an artery). Additionally, the potential for abrupt thrombotic closure in balloon angioplasty can not be ruled out [16, 17].

Surgery can be used to remove plaque that always initiates thrombosis or to bypass the blockages via an added vein or other graft to reroute the blood when previous treatments fail. The surgery, however, requires general anesthesia and incision through normal tissue to reach the lesion. After five to ten years, the bypass may even be clotted due to the atherosclerosis.

Many studies [1] have explored the potential use of laser energy to remove thrombus since the first study of using laser to remove intravascular thrombus and the effects of laser irradiation on human thrombus *in vitro* was reported by Lee *et al.* in 1983 [18]. The early studies of laser thrombolysis used continuous-wave argon laser light (wavelength of 454 and 514 nm) delivered via cleaved fiber tips to vaporize thrombus or recanalize thrombosed coronary arteries [18–20]. Despite the potential to remove the thrombus, clinical applicability was limited by the thermal effect of continuous-wave lasers with resultant extensive thermal injury to adjacent normal tissue, and mechanical dissection and perforation caused by the sharp profile of the cleaved fibers. Most attempts to achieve laser thrombolysis with continuous-wave lasers were abandoned because of the massive thermal injury [1], although many efforts have been made to improve the light delivery devices [21–26]. Furthermore, a study by Douek *et al.* suggested that the thermal injury can accelerate intimal hyperplasia [27].

To reduce the thermal effects, pulsed lasers were introduced because the zone of thermal damage can be minimized if the laser pulse duration is less than the thermal relaxation time of the initially laser-heated layer of tissue [28,29]. This is the time for heat to diffuse out of the irradiated volume and is determined by the

thermal diffusivity of the tissue and the dimensions of the volume. The thermal relaxation time for most vascular structures is of the order of millisecond, so lasers with pulse duration $< 1\,ms$ are likely to produce little thermal injury to adjacent tissues [30, 31]. Pulsed lasers emitting light at ultraviolet (190–400 nm) [32–36], visible (400–600 nm) [1,37–41], and mid-infrared (1.4–3.0 μm) [42–44] wavelengths have been used in investigations of both angioplasty and thrombolysis. More specifically, the most notable lasers in the medical field are now the excimer: ArF (wavelength 193 nm, pulse duration ∼10 ns) and XeCl (308 nm, 100–200 ns), the pulsed-dye (400–600 nm, 1–2 μs), the Thulium:YAG (2.01 μm, 250 μs), the Holmium:YAG (2.12 μm, 250 μs), and the Erbium:YAG (2.94 μm, 200 μs) lasers.

A study by Rosenfield *et al.* reported that successful thrombus dissolution was observed in each of six patients by use of an excimer laser angioplasty system emitting 308 nm light with 100–200 ns pulse duration without embolization or other adverse events [45]. However, Estella and colleagues reported conflicting results using the same laser and optical delivery systems at a similar energy level [46]. The refinement of the excimer laser, light delivery, and case selection may improve the safety and efficacy of the excimer laser thrombolysis since the current systems are configured to treat atherosclerotic plaque.

The excimer laser theoretically could precisely ablate clots similar to that demonstrated in polymers [47] and atherosclerotic tissues [31, 32] because ultraviolet light at 308 nm is strongly absorbed by the tissue protein in the clot; the penetration depth is ∼30 μm or less. Somewhat contrary to these expectations is the fact that explosive vaporization of hemoglobin was observed [48]. Thus,

the ablation event of pulsed laser differs from previous continuous-wave ablation studies. More efficient removal of thrombus could be achieved because of the cavitation events induced by explosive vaporization than by simple vaporization alone.

Holmium/thulium:YAG lasers emitting a wavelength of 2.1 μm light have been successful for arterial recanalization in selected patients [43, 49]. For clinical use, the major advantages of 2.1 μm radiation over ultraviolet excimer laser radiation are: 1) Infrared radiation doesn't produce known mutagenic or carcinogenic effects [50]. 2) The solid-state holmium/thulium:YAG laser system is smaller, less expensive, and easier to operate than the excimer laser system. Water has a prominent absorption peak near 2.1 μm, and the penetration depth of holmium laser radiation for tissue typically containing 70% water is $\sim$300 μm.

The clinical holmium laser is configured to emit light at 2.1 μm with a pulse duration of 250 μs in the free running mode. Laser energy is delivered by a multifiber laser catheter with a diameter of 1.4–1.7 mm. The clinical trials of the holmium laser thrombolysis were promising. One study by Topaz *et al.* revealed residual stenosis $< 30\%$, adequate thrombolysis, and no acute adverse procedural complications in each patient after delivering 53–164 pulses at an energy of 250–600 mJ and a pulse repetition rate of 5 Hz, and balloon angioplasty as a follow-up procedure [49]. However, the effects of stress waves and cavitation bubbles have been shown to induce damage to adjacent tissue [48,51]. Formation of thrombotic occlusions during holmium laser angioplasty was also observed [52]. Another potential limitation may be the poor selectivity of holmium laser ablation, because

the holmium laser is strongly absorbed by water, whereas water is present in roughly the same proportions in all tissues. Therefore, the holmium laser can not discriminate between the normal tissues and the thrombus, so that both perforations and dissections may occur due to inadvertent ablation of arterial wall.

To achieve the goal of removing the thrombus with laser energy and reducing the possibility of damaging the adjacent normal tissue, selectively targeting the thrombus is desirable. LaMuraglia *et al.* reported that the absorption coefficient for thrombus is more than ten times greater than that for arterial tissue in the 400–600 nm wavelength [53]. The differing absorption properties of thrombus and arterial tissue afford a degree of selective laser ablation since less energy is needed to ablate the thrombus than that needed to ablate the artery. Thus, laser radiation at visible wavelengths could be used to selectively and safely remove thrombus or emboli at radiant exposures between the thresholds for arterial tissue and thrombus. Gregory *et al.* successfully applied this concept for selective laser thrombolysis of coronary artery thrombi in 18 patients [54]. A pulsed dye laser emitting light at 480 nm in 1 μs duration pulses was used at an energy of 60–75 mJ per pulse and a repetition rate of 3 Hz. Laser energy was delivered through a unique fluid-core catheter, which allowed delivery of light while washing away ambient blood and fluoroscopic monitoring of the establishment of vessel patency during the procedure due to the use of a radiographic contrast as the optical core fluid [55]. Effective thrombus removal has been achieved in 16 of the 18 patients and improved coronary flow following delivery of 240–600 laser pulses.

Unfortunately, the current techniques of completely removing a large thrombus burden in arteries are limited. Any mural clot left behind will be a potential stimulus for reocclusion of the arteries. It is very difficult to precisely control its position within a vessel once the catheter is inserted into clots, and the catheter most likely retraces its first path as multiple manipulations of the catheter are required, so there a mural clot is always left. Another potential disadvantage of laser thrombolysis is the difficulty of removing the clot that posses adequate fibrin content. It will be problematic if clear fibrin can not be removed along with the red blood. More laser energy is needed to ablate the clear fibrin after the red blood is removed since the absorption of red blood is much higher than that of the clear fibrin. It is likely that the perforation and dissection of the artery would occur if laser energy above the ablation threshold of normal tissue is used to completely remove the clot.

Despite the limitations mentioned above, laser thrombolysis has emerged as a promising method for thrombus removal [56] since the ability to deliver laser energy to arteries through optical fibers offers the possibility of unclogging obstructed arteries without the trauma or general anesthesia. Furthermore, laser thrombolysis may be an alternative therapy for some vascular diseases such as coronary bypass graft thrombosis and stroke, in which no other effective therapies are avaliable [57]. It is desirable, therefore, to develop new techniques to enhance the laser thrombolysis.

My hypothesis was that the combination of laser thrombolysis and localized

intramural delivery of clot-dissolving drugs during the procedure may be a solution to these limitations. More specifically, the majority of clots is removed during laser thrombolysis, whereas the mural clot left can be dissolved by the drugs delivered during the procedure.

2.3 Local Drug Delivery

The possibility of increasing thrombolysis without causing bleeding has motivated efforts to locally deliver drug with a very high concentration as quickly as possible and to maintain a high level long enough to affect dissolution of the thrombus but short enough to limit the likelihood of bleeding. There are several potential advantages of local drug delivery over systemic drug delivery. First, local delivery may achieve high local concentrations of drug, even of agents that are rapidly degraded when administered systemically. Second, unwanted systemic effects can be minimized by concentrating the drug at the target site. Finally, it is possible to increase the penetration of delivered drug compared with systemic delivery by passive diffusion from the blood stream. Current approaches for localized drug delivery fall into three broad categories: affinity-based, locally-activated, and pressure-based delivery.

Affinity-based drug delivery uses an agent with its greatest binding affinity for fibrin or thrombus to achieve selective thrombolysis [58]. The drug is intravenously administered and then localized to the thrombus due to the specific affinity. However, this technique is limited by the long infusion time and the risk of producing a systemic fibrinolytic state [59–61]. Locally-activated drug delivery

uses an inert agent that is delivered systemically, but becomes locally activated through administration of delivered light or activating agents. One typical example of this second method is photochemotherapy of intimal hyperplasia in which a photoactive drug (psoralen) is administered and activated with ultraviolet light (e.g., 365 nm) [62]. The risk of side-effects due to systemic administration of drug can not be ruled out at high concentration, e.g., incidentally exposing to light can cause bleeding complications.

Pressure-based delivery uses static pressure to drive drugs into thrombus through balloon-based catheters. To deliver a thrombolytic agent onto or even into a thrombus after guide-wire penetration is most appropriate for treatment of downstream arterial occlusions, since the offending thrombus is usually localized to a single vessel, and catheterization for angiographic diagnosis provides ready access to the site of occlusion. Several designs of local delivery balloon catheters have been investigated [63, 64]. The double-balloon catheter was the first percutaneous drug delivery device [65]. Drug can be instilled through a small hole into the chamber thus formed between the balloons by inflating two small balloons in an artery. However, prolonged dwell times are required to achieve significant drug levels by passive diffusion. This prolonged period of total occlusion may be problematic when applied to coronary arteries due to distal myocardial ischemia.

The Wolinsky perforated-balloon catheter was designed to overcome some of the limitations associated with the double-balloon. There are 300 holes 25 μm in size placed at center 12 mm of 20 mm-long balloon. By inflating the balloon, the drug is delivered into an adjacent vessel wall through the holes. A major

disadvantage of this device is the potential for vascular trauma from the jets. For example, one study revealed that only 5% of canine arteries treated with this device *ex vivo* had no apparent traumatic effect [66]. To minimize the trauma induced by the perforated-balloon, a microporous balloon was developed [66]. This balloon material consist of a membrane with thousands of holes with a diameter of $< 1\,\mu$m. The microporous membrane can reduce the jet effect and substantially enhance the homogeneity of infusion, but the risk of arterial injury due to the jet effect can not be ruled out [67].

Locally delivering urokinase, a clot-dissolving agent, directly to the angioplasty site to achieve intracoronary thrombolysis using urokinase-coated, hydrogel balloons was reported by Azrin *et al.* [68]. The high concentration of urokinase resulted in enhanced local thrombolysis. However, this technique was limited by the several factors: the limited amount of drug that can be absorbed by the hydrogel polymer, wash-off of the drug from the balloon surface in the intact circulation, and the short times of drug delivery required because of ischemia from complete vessel occlusion.

To overcome these limitations associated with the catheters mentioned above, a catheter called Dispatch catheter was developed and approved by the Food and Drug Administration for intracoronary drug infusion [64]. This catheter consists of an over-the-wire, nondilation device with a helical inflation coil on its distal tip. With a spiral contour to the inflatable supporting struts, the areas between these struts provide close spaces for drug infusion through a lumen distributing

through five eccentrically placed ports. This catheter thus functions as a temporary stent during drug delivery, allowing periods of infusion in excess of 30–60 minutes without clinical evidence of resultant myocardial ischemia. Recently, Groh *et al.* used this type of catheter to treat two patients with threatened closure related to coronary dissection or acute closure with thrombus formation at a site of recent dilation [69]. Good clinical outcomes were obtained after 4-hour localized infusion of urokinase at the site of dissection and extensive clot formation respectively. Mitchel *et al.* also reported a successful study of enhanced intracoronary thrombolysis with urokinase using a similar catheter from the same manufacturer [70]. However, the primary problems with the modified balloon catheter designs are their cumbersome size and long inflation times required, as well as the risk of medial injury occurring during the balloon inflation process, thus potentially limiting the benefits of local drug delivery.

Ultrasound has been used to disrupt thrombi in the cardiovascular systems [71, 72]. The ultrasound was delivered through catheters to prevent damage to normal tissue near the sites of occlusions. Some studies demonstrated that exposure of whole blood clots *in vitro* to intermittent ultrasound combined with thrombolytic agents (e.g., tissue-type plasminogen activator) caused a significant enhancement of thrombolysis compared with the agents alone [73,74]. Although the mechanism of this effect is unknown, it was hypothesized that fluid motion resulting from ultrasound-induced cavitation accelerate fibrinolysis by promoting the transport of activators and plasminogen to their target sites on fibrin within the clot [75]. The ultrasound approach to accelerate thrombolysis process is effective, but it

may not be feasible in many clinical situations where small vessels (e.g., brain vessels) are involved due to the less flexible and larger ultrasound probe.

Therefore, there is a challenge in the development of a new technique for local drug delivery that can deliver sufficient drugs to the site of interest in arteries without significant injury or systemic effect.

2.4 Photomechanical Drug Delivery

One observation by Dr. Gregory and his colleagues at Oregon Medical Laser Center suggested that the hydrodynamic pressure due to laser-induced cavitation events (e.g., the expansion and collapse of cavitation bubbles) may be used as a driving force to deliver drug into clot and vessel wall. During laser thrombolysis, laser pulses from a pulsed-dye laser operating at 480 nm with a $\sim$1 μs duration were delivered into thrombus by a fluid-core catheter. The thrombus absorbed the laser energy and then was ablated through vaporization and cavitation. A portion of vessel wall in the treated area was found to be visible fluoroscopically even after flow of the contrast medium was stopped. Evidently contrast media in the flowing-fluid catheter stream was driven into the vessel wall resulting in a residual radiographic image of the vessel wall. Thus, localized drug delivery using laser-induced pressure transients was proposed as a potential therapy for enhancement of laser thrombolysis, which was termed photoacoustic drug delivery. However, it was changed to photomechanical drug delivery during the course of this study due to the reasons mentioned in Chapter 1.

Although no studies of photomechanical drug delivery have been reported,

the observations that explosive ablation of tissue in blood fields could result in craters stained with red blood cells were reported, which may be attributed to the explosive bubble formation [41, 76]. Flotte *et al.* also demonstrated that laser-induced shock wave could be used to enhance drug cytotoxicity [77].

Photomechanical drug delivery uses a laser pulse to generate a cavitation or vapor bubble in a fluid-filled blood vessel due to the absorption of laser energy by either surrounding liquids (e.g., blood and saline) or absorbing target (e.g., clot). The bubble expansion and collapse can cause rapid displacement of intravascular fluid such that radial and longitudinal pressures are created sufficient to drive drug into thrombus or vessel wall tissue.

The significant advantages of photomechanical drug delivery compared with other localized drug delivery methods are 1) high concentrations of drugs could be delivered with little or no damage to the vessel wall, 2) it can be performed during a therapy process (e.g., laser thrombolysis), which would be the best time and place to introduce pharmacologic agents for enhancing the therapy, and 3) the flexibility of delivery system in the size make it possible to deliver drug into a destination with small geometry.

Chapter 3

Threshold Study of Laser-induced Bubble Formation in Absorbing Liquids

3.1 Introduction

Removal of thrombus in a fluid-filled blood vessels by a pulsed laser is a complicated problem involving a number of the most significant issues that have been encountered in laser ablation of tissue [1]. There are several mechanisms proposed for laser tissue ablation: photothermal, photochemical, and photomechanical effects [32, 37, 53]. Photothermal effects are due to conversion of the laser energy into heat and diffusion of that heat within the tissue. When the laser pulse duration is less than the thermal relaxation time of the initially laser-heated layer of tissue, then the zone of damage is minimized [78]. A simple model based upon a thermal relaxation time, τ_R, given by

$$\tau_R = \frac{\delta^2}{4\alpha} \tag{3.1}$$

where δ is the penetration depth of laser light in tissue (i.e., the reciprocal of absorption coefficient of tissue), α is the thermal diffusivity of tissue (typically $0.13\,\mathrm{mm}^2/\,\mathrm{s}$ [79]), leads to the prediction that a pulse duration less than τ_R is needed to minimize thermal damage. If laser pulses longer than the thermal relaxation time, the thermal energy popagates into the tissue during the laser pulses. Thus, the thermal effect is less than with continuous wave lasers owing to short pulse duration and long thermal relaxation time. Pulsed laser ablation may also lead to vaperization if the temperature of tissue reaches above 100℃ [80].

A typical example of the photomechanical effect is the thermoelastic expansion of tissue because of heating of the target tissue by the laser energy, and recoil caused by ejection of the ablated material [81, 82]. Large stress waves develop if the heating is so rapid that the pressure transients do not have enough time to leave the irradiated volume. This critical time it takes for pressure waves to propagate out of the irradiated volume is given by

$$\tau_s < \frac{\delta}{V_s} \tag{3.2}$$

where δ is the penetration depth of laser light in tissue, and V_s is the speed of sound in tissue ($\sim$1500 m/s).

Confinement (thermal or stress) depends on the laser pulse duration and the absorption coefficient. In the case of blood and clot, the optical penetration depth ranges from 5–1,600 μm in the 400–600 nm wavelength. Times for thermal confinement are longer than those for stress confinement. Thus, pulse duration (τ_P) broadly falls into three regimes: stress ($\tau_p < \tau_s$), thermal confinement ($\tau_s < \tau_p < \tau_R$), and no confinement ($\tau_R < \tau_p$).

The microsecond dye-laser pulse operating at 400–600 nm wavelength does not meet the stress confinement, but it does follow the thermal confinement condition. No heat is diffused out of the irradiated volume during the laser pulse. When laser energy deposited in tissue is above the threshold radiant exposure to vaporize the tissue, the vaporization commences [80].

Previous studies demonstrated that laser-induced cavitation bubble formation depends on the laser energy, absorption of the liquids, and radiant exposure [83, 84]. Establishing the minimum laser energy required to initiate vaporization of liquids is crucial for clinical applications, since the radiant exposure has to be maintained above the threshold for bubble formation in surrounding liquids to generate hydrodynamic pressure for photomechanical drug delivery [6] and below the threshold to ablate arterial wall tissue. Determination of threshold will also be helpful for understanding the microsecond bubble dynamics. Although no parametric study of the threshold for bubble formation in light absorbing liquids, especially in oil, using pulsed-dye lasers has been reported, several investigators have extensively investigated the threshold for cavitation bubble formation in water using the ultraviolet excimer laser (XeCl at 308 nm, pulse duration = 115 ns) and the mid-infrared holmium:YAG laser (wavelength = 2.12 μm) [83, 84]. The aims of this study were to establish minimum laser energy to initiate the bubble formation in light-absorbing liquids with different physical properties (e.g., heat capacity, latent heat, and viscosity) using a pulsed-dye laser and to investigate the effects of absorption and radiant exposure on the thresholds. Therefore, the threshold radiant exposures for bubble formation in water and oil under various

conditions were compared.

3.2 Materials and Methods

3.2.1 Experimental Setup

All experiments were performed with a flashlamp excited dye laser (Palomar Medical Technologies). The laser generated pulses with a pulse duration of 1.3 μs (full width at half maximum) at a wavelength of 504 nm (Figure 3.1). The laser pulses were delivered into a transparent container (a 50×50×50-bottle) filled with the liquids via an optical fiber, and the pulse energy was increased until a cavitation bubble commenced at the fiber tip by use of flash photography. The threshold energy was defined as the minimal energy per pulse needed to create a rapidly expanding and collapsing bubble, whose maximal diameter equaled the diameter of the fiber tip. The pulse energy was determined using a joulemeter (Molectron). The pulse-to-pulse stability of the energy was better than 5%.

The experiments for determining the threshold radiant exposure at absorption coefficients ranging from 6–300 cm^{-1} were performed by using a 1000 μm fiber to deliver laser pulses into the solutions. The experiments for determining the threshold generated by different fibers (200–1000 μm) were performed in solutions of 6 cm^{-1} and 300 cm^{-1} respectively.

3.2.2 Absorbing Liquids

Two liquids (water and mineral oil from Paddock Lab) were used in this study. Dyes (Direct Red 81 from Sigma and D&C Red #17 from Warner-Jenkinson) were

added to water and oil respectively to achieve the desired absorption. Both of the dyes, chromophores, were photostable and had a peak absorption around 504 nm. The absorption coefficients of the solutions had a nearly linear relationship with the concentration of chromophore in the solutions: 0.0837 g of Direct Red 81 in 30 mL water gave an absorption coefficient of 300 cm^{-1}, while 0.0367 g of D&C red #17 was added into 30 mL oil to obtain the same absorption. Direct Red 81 is easily dissolved in water after stirring several minutes at room temperature. Heating was needed to make the oil solutions. The dye-oil mixture was heated to 100℃ with stirring until the appearance became uniform, and then cooled to room temperature before the experiments. The absorption coefficient μ_a was calculated from absorbance A measured with a diode-arry spectrophotometer (8452A, Hewlett Packard) and path length d using the relation :

$$\text{transmission} \equiv 10^{-A} = e^{-\mu_a d} \tag{3.3}$$

3.2.3 Flash Photography

The setup for time-resolved flash photography is shown in Figure 3.2. The bubble formation at the fiber tip was visualized using a triggerable CCD camera (CV-251, Protec). A stereomicroscope (SZ60, Olympus) was used for magnification. Each picture was a single event and reproducible with 5% variation. A strobe (MVS–2601, EG&G) with a 5 μs pulse duration (full width at half-maximum) was used for illumination. The delay times were controlled by a digital delay generator (DG535, Stanford Research Systems). The generator was triggered by the laser pulse by use of a photodiode (UDT Instruments) that was

attached to the laser delivery fiber, so flash photographs were taken at variable delay times of 5–500 μs after the laser pulse. A laser filter was positioned in front of the microscope to avoid saturating the CCD camera.

3.2.4 Data Analysis

Assuming a threshold radiant exposure, F_{th} (mJ/mm^2), and a flat profile at the fiber tip, the absorbed energy density $F(z)$ in a liquid layer of infinitesimal thickness z (mm) in front of the fiber tip is given by

$$F(z) = \mu_a F_{th} e^{-\mu_a z} \tag{3.4}$$

where μ_a is the absorption coefficient of the liquid (cm^{-1}). The energy density needed to vaporize liquid is given by [83]

$$F_{vapor} = \rho c(T_c - T_0) + \rho L_v \tag{3.5}$$

where ρ is the density of the liquid (mg/mm^3), c is the specific heat of the liquid (mJ/(mg°C)), T_c is the critical temperature of the liquid (°C) (i.e., the liquid starts the phase change at this temperature), T_o is the initial temperature of the liquid (°C), L_v is the latent heat of vaporization (mJ/mg), and A is the surface area of the fiber tip (mm^2). If all the absorbed light is converted into heat, equation (3.4) is equal to equation (3.5). Thus, the threshold radiant exposure for bubble formation at the surface ($z = 0$) is given by

$$F_{th} = \frac{\rho c(T_c - T_o) + \rho L_v}{\mu_a} \tag{3.6}$$

Equation (3.6) is also known as the "blow off" model [85]. Threshold radiant exposure for vaporization can be estimated by assuming that the threshold is

determined by the energy needed for uniform vaporization over the entire surface area of the delivery fiber. In practice, however, the delivered radiant exposure is 1–10 times the threshold radiant exposure for vaporization. van Leeuwen *et al.* and Jansen *et al.* proposed a partial vaporization theory in which the latent heat of vaporization for the phase change of the entire irradiated area is not required and the vaporization of water commences at 100°C [83, 84], such that the theoretical threshold radiant exposure can be determined by

$$F_{th} = \frac{\rho c(T_c - T_o)}{\mu_a} \tag{3.7}$$

Temperature of a liquid layer beneath a fiber tip was estimated using equation (3.6) by assuming L_v=0. The temperature at the threshold is given by:

$$T_c = \frac{\mu_a F_{th}}{\rho c} + T_o \tag{3.8}$$

The measured radiant exposures were compared with those calculated using the blow-off model and partial vaporization model, since it was unclear whether these models are applicable to predict the threshold radiant exposure for the bubble formation in light absorbing liquids with one microsecond pulsed-dye laser.

3.3 Results

3.3.1 Threshold Radiant Exposure as a Function of Absorption

Figure 3.3 shows that a small bubble is formed at the threshold 5 μs in water and 10 μs in oil after a laser pulse. When the laser energy was below threshold, only minor disturbances were observed beneath the fiber tip. The bubble

grew quickly as the laser energy was increased above the threshold. For both water and oil solutions, the threshold radiant exposure decreased with increasing absorption coefficient (Figure 3.4). Surprisingly, the thresholds for water were higher than those for oil although both the boiling point and viscosity of oil are higher than those of water (see Table 3.1). The differences in the threshold between water and oil decreased with increasing absorption coefficient. The threshold radiant exposures for water ranged from $94\pm2\,\mathrm{mJ/mm^2}$ at $6\,\mathrm{cm^{-1}}$ to $12\pm1\,\mathrm{mJ/mm^2}$ at $300\,\mathrm{cm^{-1}}$. The thresholds for oil ranged from $46\pm2\,\mathrm{mJ/mm^2}$ at $6\,\mathrm{cm^{-1}}$ to $9\pm1\,\mathrm{mJ/mm^2}$ at $300\,\mathrm{cm^{-1}}$.

3.3.2 Threshold Radiant Exposure as a Function of Fiber Size

Figure 3.5 shows the threshold radiant exposure as a function of fiber diameter using solutions with absorption coefficients $6\,\mathrm{cm^{-1}}$ and $300\,\mathrm{cm^{-1}}$. The threshold radiant exposures for both water and oil were independent of the fiber size (diameter). The differences in the threshold between water and oil for the solutions with an absorption coefficient of $6\,\mathrm{cm^{-1}}$ were significant. There were no differences in the threshold between water and oil when the solutions with an absorption coefficient of $300\,\mathrm{cm^{-1}}$ were used.

3.3.3 Temperature Estimation

The temperature of the liquid layer area in front of the fiber tip at the threshold was estimated using equation (3.8) by assuming the values for water and oil

from Table 3.1). The initial temperature (T_o) was 25°C for both water and oil. Figure 3.6 shows the calculated threshold temperature as a function of absorption coefficient. The threshold temperature as a function of fiber size was plotted in Figure 3.7. The temperature increased with increasing absorption, while the differences in the temperature between water and oil also decreased as the absorption increased. The threshold temperature was roughly independent of the radiant exposure (except the data for the oil solution at the absorption $300\,\mathrm{cm}^{-1}$). No differences in threshold temperature for water and oil was found at $6\,\mathrm{cm}^{-1}$. The threshold temperatures were significantly different at $300\,\mathrm{cm}^{-1}$.

3.4 Discussion

The aim of this study was to determine the threshold radiant exposure for the bubble formation in light absorbing liquids (water and oil) with significantly different physical properties (see Table 3.1) using one microsecond pulsed-dye laser. The absorption coefficient of the absorbing liquids varied from 6–$300\,\mathrm{cm}^{-1}$ corresponding to the absorption of blood at the wavelengths ranging from 450–600 nm. Dyes (Direct Red 81 or D&R #17) as chromophores were added into water and oil to achieve the desired absorption coefficients. One microsecond laser pulses were delivered into absorbing liquids through 200, 300, 600, and 1000 μm fibers. The ablation threshold was determined by visualizing the bubble formation at the fiber tip using flash photography.

Threshold for both water and oil decreased as the absorption increased (Figure 3.4) and the differences in the threshold between water and oil decreased as well.

The ablation thresholds for water were surprisingly higher than those for oil solutions although the viscosity and boiling point for oil are higher than these for water (see Table 3.1). It is unlikely that the differences are due to the heat diffusion out of the irradiated volume, since the microsecond pulse is well within the thermal confinement regime (in $300\,\mathrm{cm}^{-1}$ solutions, τ_R is 0.8 ms water vs. 1.4 ms oil).

I hypothesize that the bubble dynamics may be different when the incident laser energy is above the threshold since other factors such as latent heat, volume expansion coefficient, and vapor content of the liquid would affect the bubble formation [83, 84]. To verify this hypothesis, I compared the maximal bubble volume generated in water and oil as a function of laser energy at supra-threshold energies from the threshold up to 100 mJ (i.e., 5 times above the threshold for water solution, while 8 times for oil solution). By assuming an ellipsoidal bubble and taking into account the volume occupied by the fiber tip inside the bubble, the measured bubble volume, V_{bubble}, was calculated by

$$V_{bubble} = [\frac{\pi H D^2}{6}] - [\pi h (\frac{d}{2})^2] \tag{3.9}$$

with diameter (D), height (H), fiber diameter (d), and length of the fiber inside the bubble (h). The maximum diameter and height were measured from the flash photographs.

Bubbles generated in water solution grew much faster than those in oil solution (Figure 3.9). This is not caused by the difference in the latent heat, since the latent heat of oil is an order of magnitude lower than that of water (see Table 3.1), less energy is required for oil than that for water to vaporize a similar volume of

solutions. This suggests that the process of bubble formation above the threshold does not solely depend upon the latent heat, and the differences in other factors such as vapor content of the bubble and volume expansion coefficient should be taken into account to simulate the complicated process of the bubble formation in absorbing liquids. I used a simple model to estimate the differences in the volume expansion coefficient between water and oil (see the appendix at end of this chapter). The calculations showed that the volume expansion coefficient of the water solution was about 1–2 orders of magnitude higher than that of the oil solution. The volume expansion coefficients varied by a factor of 4 (e.g., $6.3 \cdot 10^5$ for small bubbles with a diameter of 1.8 mm generated by delivering 40 mJ pulses into a 100 cm^{-1} water solution and $2.9 \cdot 10^6$ for larger bubbles with a diameter of 5 mm by using 100 mJ), while there was good agreement between the calculations and the measurements for the oil solution by assuming the volume expansion coefficient $\Omega = 10000$ (Figure 3.10). However, whether this model is applicable to estimate the bubble dimension under different conditions remains a subject for further investigation, and it is beyond the scope of this study.

The threshold was nearly independent of the fiber configuration except for the data using a 1000 μm fiber. This shows that radiant exposure dominates the onset of bubble formation rather than energy. The discrepancy at the data using the 1000 μm fiber may be caused by the tensile stress effect induced by the edge of the fiber [86]. The thresholds in water solutions were similar to those reported by de la Torre for bubble formation in lysed blood at various hematocrits [87]. Similar thresholds were also reported by van Leeuwen *et al.* and

Jansen *et al.* for vapor bubble formation in OBP-HCl solutions ($30\,\mathrm{cm}^{-1}$) using a 308 nm excimer laser and in water ($30\,\mathrm{cm}^{-1}$) using a Q-switched holmium laser with $1\,\mu$s pulse duration [83, 84]. Evidently, the absorption coefficient affects the threshold radiant exposure significantly. However, the threshold radiant exposure is relatively independent of the fiber configuration.

The measured threshold values for water solutions are about an order of magnitude lower than those estimated by the blow-off model, while they are of the same order as those predicted using the partial vaporization model. This finding may imply that the latent heat is negligible for the onset of bubble formation. The discrepancy between the calculation and measurement decreased as the absorption coefficient increased (Figure 3.4). Specifically, there was good agreement in a $300\,\mathrm{cm}^{-1}$ solution. This may be due to the fact that at low absorption coefficients a microsecond pulse becomes close to the stress confinement regime (e.g., $\tau_s \approx 1.1\,\mu s$ when the absorption coefficient is $6\,\mathrm{cm}^{-1}$). Pulse transients, therefore, could affect the onset of bubble formation and this effect, however, reduced as the absorption coefficient increased.

The calculation of threshold temperature shows that it is not required to heat the water layer in front of the fiber tip up to 100℃ for the onset of bubble formation (Figures 3.6 and 3.7). This finding suggests that the onset of bubble formation could be initiated at temperature below the boiling point at low absorption coefficient due to the stress wave induced by the stress confinement and the boundary of the fiber tip that could force the thermoelastic expansion only to the forward direction. A study by Paltauf *et al.* suggested that when the fiber

diameter is comparable to the penetration depth cavitation could be produced even at very low temperatures due to the tensile stress effect [86].

3.4.1 Implications

Photoacoustic drug delivery uses laser-induced hydrodynamic pressure arising from the expansion and collapse of a cavitation or vapor bubble in a fluid-filled vessel to drive the clot-dissolving drug into thrombus to enhance the thrombolysis process. It has been shown that the rapidly expanding and imploding bubble may cause mechanical damage [88]. Reducing bubble dimensions has been proposed as a promising strategy for minimizing the photomechanical effect [89–91]. The use of a liquid that has a low volume expansion coefficient may reduce the bubble dimension. Figure 3.9 shows that the difference in bubble volume using water and oil is by a factor of 7 at an energy twice as much as the threshold energy. This study also suggests that a small fiber may be used to create the same displacement of intravascular fluids with lower energy as that created by a larger fiber with higher energy, since the threshold is relatively independent of the fiber size.

3.4.2 Limitations of This Study

In this study thresholds for bubble formation in solutions (water and oil) containing dyes were investigated. The chemical structure of these two dyes were different, which may cause different chemical reactions when irradiated by a laser pulse. Therefore, the difference in the thresholds may not be solely caused by the difference in the physical properties of water and oil. Furthermore, in our study

dye (Direct Red 81) was used as the chromophore in water solutions, *in vivo* the results will be different.

In conclusion, thresholds for bubble formation in light absorbing liquids have been measured as a function of the absorption coefficient and a function of fiber size (diameter) as well. The experimental results suggests that the threshold for bubble formation depends on the heat capacity of the liquid, while the bubble volume may be dominated by vapor content of the bubble and volume expanding coefficient at supra-threshold radiant exposure. The thresholds are proportional to the absorption coefficient and are relatively independent of the fiber configuration. The differences in thresholds between water and oil solutions decease as the absorption coefficient increases.

Appendix

If all the pulse energy is absorbed a cavitation bubble is not formed during the laser pulse. Based on Beer's law, the attenuated radiant exposure at a certain depth (z) is given by

$$E(z) = E_o \exp(-\mu_a z) \tag{3.10}$$

where E_o is the incident pulse energy.

If the incident pulse energy, E_o, is larger than a threshold (E_{th}), the laser pulse will penetrate a depth $z = d$. The attenuated pulse energy at a depth d is the threshold pulse energy:

$$E_{th} = E_o \exp(-\mu_a d) \tag{3.11}$$

Consequently, the depth, d, can be determined by

$$d = \frac{1}{\mu_a} \ln(\frac{E_o}{E_{th}}) = \frac{1}{\mu_a} \ln(\frac{F_o}{F_{th}}) \tag{3.12}$$

where F_o and F_{th} are the incident radiant exposure and the threshold radiant exposure respectively.

If the volume of the liquid in which the laser energy is deposited can be uniformly vaporized by the excess energy above the threshold, the energy required for vaporization is given by

$$E_{vaporization} = \mu_a(E_o e^{-\mu_a z} - E_{th}) = \Delta V_{vaporized}\ \rho L_v \tag{3.13}$$

where $\Delta V_{vaporized}$ is the volume of an infinitesimally thin layer dz in front of the fiber tip, ρ is the density of the liquid, and L_v is the latent heat of vaporization.

Therefore, the infinitesimal volume vaporized is given by

$$\Delta V_{vaporized} = \frac{\mu_a(E_o e^{-\mu_a z} - E_{th})}{\rho L_v} \tag{3.14}$$

Unlike the partial vaporization model [83,84], I assume that the entire area in front of the fiber tip is uniformly vaporized rather than the fraction of the disc. For the pulse with a flat energy profile at the fiber tip, the depth of the layer will be constant across the entire layer and the whole volume of the liquid will be

$$V_{vaporized} = \int \Delta V_{vaporized}\, dz \tag{3.15}$$

By substituting equation (3.14) and integrating $\Delta V_{vaporized}$ from $z = 0$ to $z = d$ one obtains the volume of the liquid beneath the fiber tip that is vaporized:

$$V_{vaporized} = \int_{z=0}^{z=d} \frac{\mu_a(E_o e^{-\mu_a z} - E_{th})}{\rho L_v} dz \tag{3.16}$$

with d provided by equation 3.12. Thus, the volume of the liquid that is vaporized by the excess pulse energy above threshold can be estimated by

$$V_{vaporized} = \frac{AF_{th}}{\rho L_v}[\frac{F_o}{F_{th}} - 1 - ln(\frac{F_o}{F_{th}})] \tag{3.17}$$

The volume of vaporized liquid $V_{vaporized}$ will expand to a much larger volume, which depends on the pressure of the bubble at maximal dimensions, the rate of condensation during the expansion, and the fiber configuration. To simplify this complex process, I assume

$$V_{bubble} = \Omega\, V_{vaporized} \tag{3.18}$$

where Ω is the volume expansion coefficient, such that the bubble volume can be estimated by

$$V_{vaporized} = \Omega\frac{AF_{th}}{\rho L_v}[\frac{F_o}{F_{th}} - 1 - ln(\frac{F_o}{F_{th}})] \tag{3.19}$$

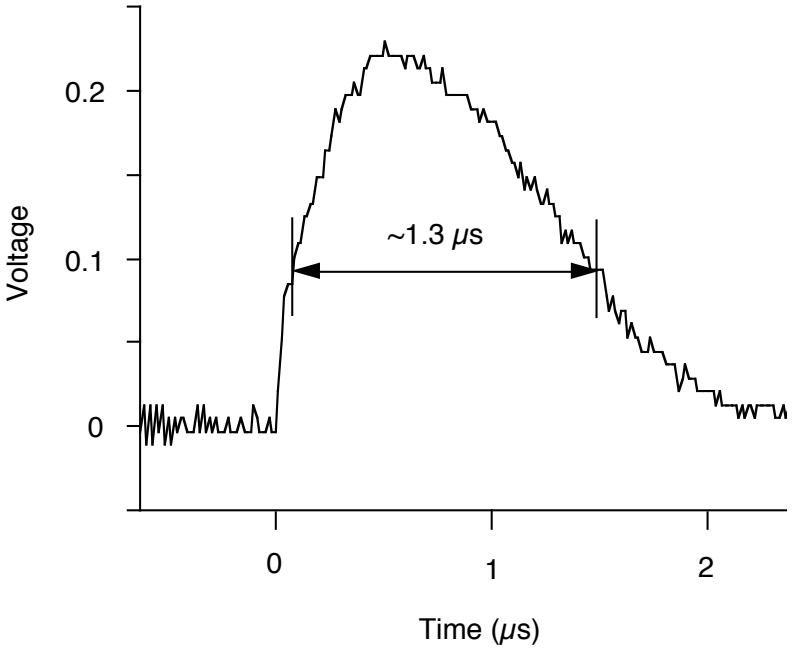

Figure 3.1: Profile of laser pulse.

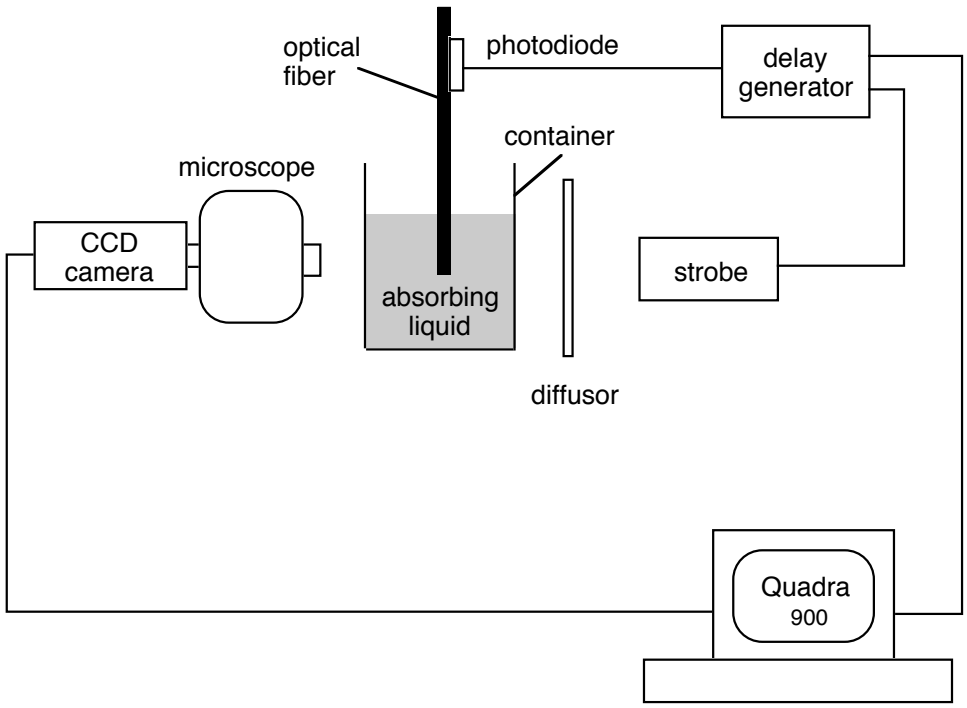

Figure 3.2: Experimental setup for time-resolved flash photography of laser-induced bubble created at the fiber tip in absorbing liquids (water and oil).

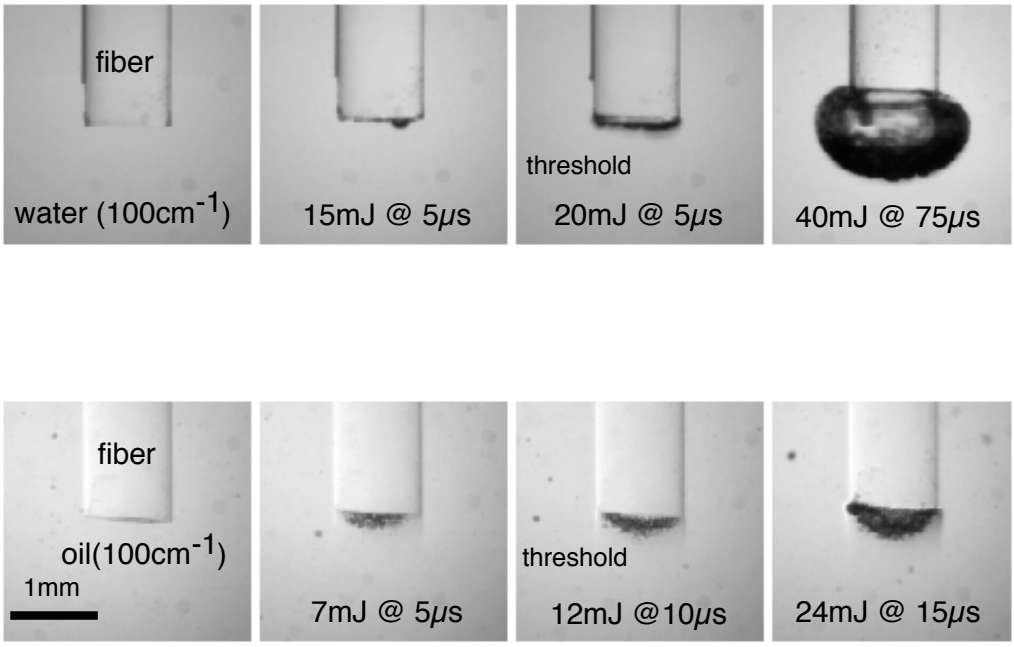

Figure 3.3: Bubble formation at the fiber tip in$100\,\mathrm{cm}^{-1}$ water and oil.

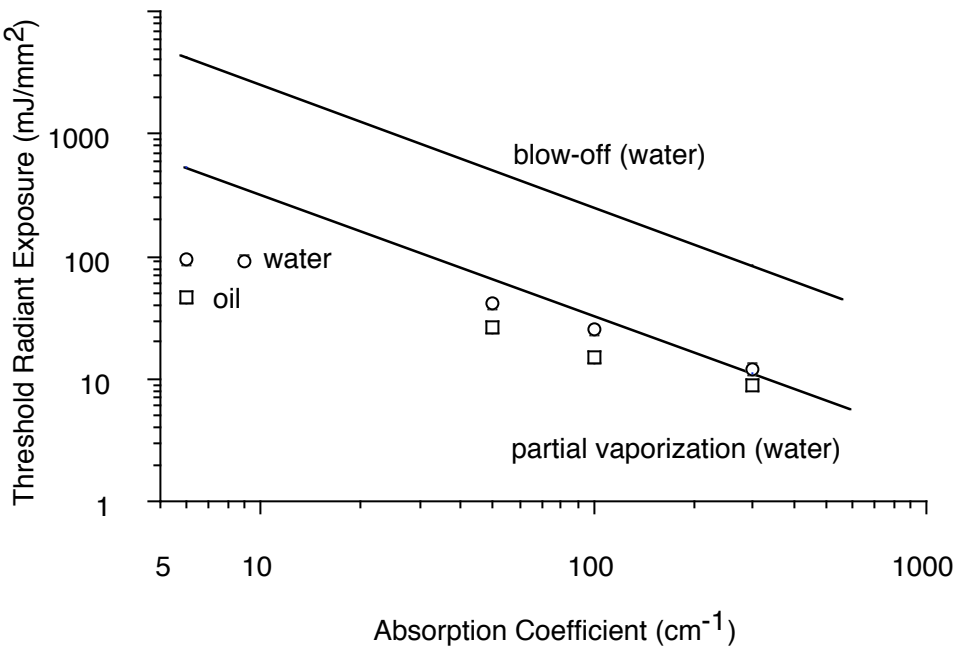

Figure 3.4: Threshold radiant exposures for absorbing liquids (water and oil) with different absorption coefficients. The laser pulse was delivered via a 1000 μm fiber. The upper line represents the thresholds for water predicted by the blow-off model (equation 3.6), while calculated by the partial vaporization model (equation 3.7) are also shown (lower line). Error bars are smaller than symbols.

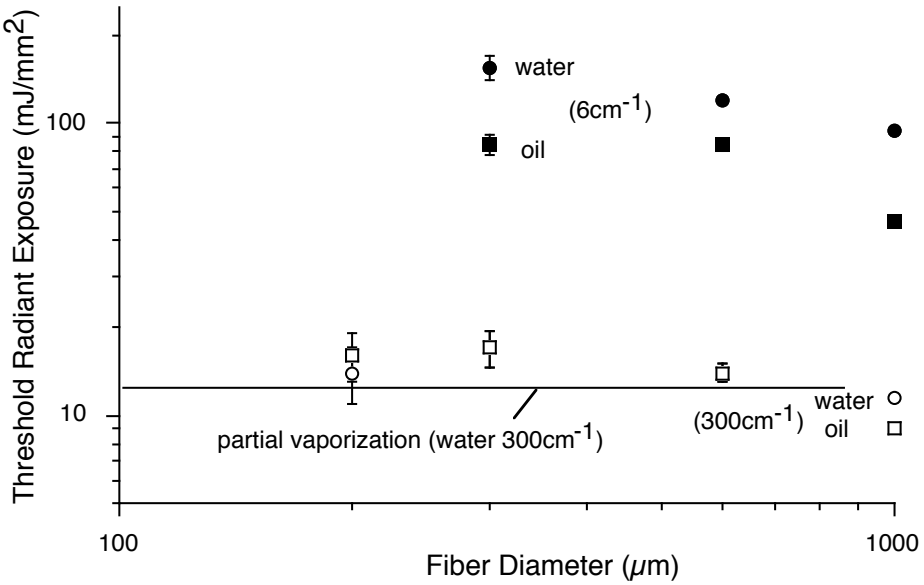

Figure 3.5: Threshold radiant exposure as a function of fiber size (diameter) using the solutions with absorption coefficients of $6\,\mathrm{cm}^{-1}$ and $300\,\mathrm{cm}^{-1}$. The thresholds were similar for both water and oil at $300\,\mathrm{cm}^{-1}$. The solid line represents the thresholds predicted by the partial vaporization model. The threshold for $6\,\mathrm{cm}^{-1}$ water solution predicted by the partial vaporization model was $525\,\mathrm{mJ/mm}^2$. The threshold for water solutions of $6\,\mathrm{cm}^{-1}$ and $300\,\mathrm{cm}^{-1}$ predicted by the blow-off model were $4{,}300\,\mathrm{mJ/mm}^2$ and $86\,\mathrm{mJ/mm}^2$ respectively. Some error bars are smaller than symbols.

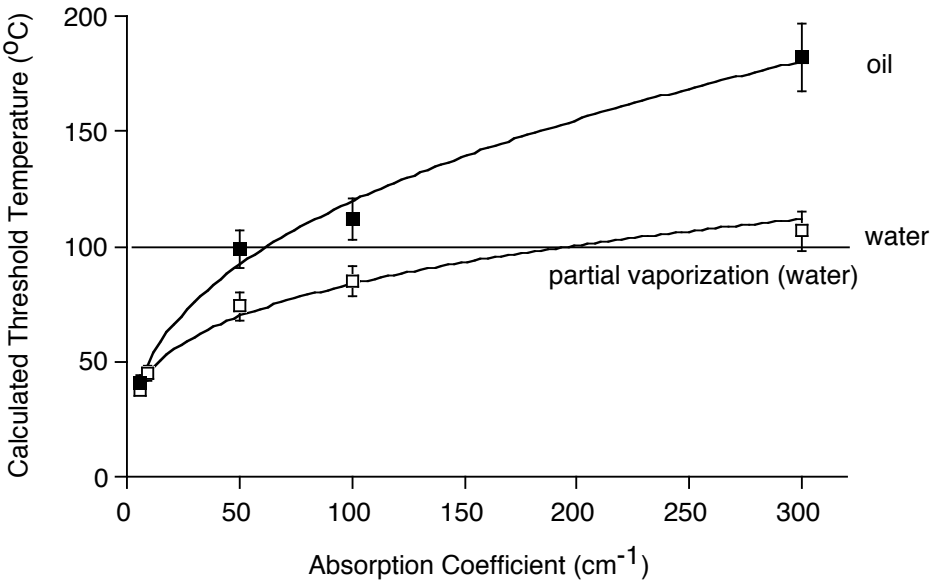

Figure 3.6: Calculated temperature of the liquids at threshold directly using equation (3.8). Ambient temperature was assumed to be 25°C.

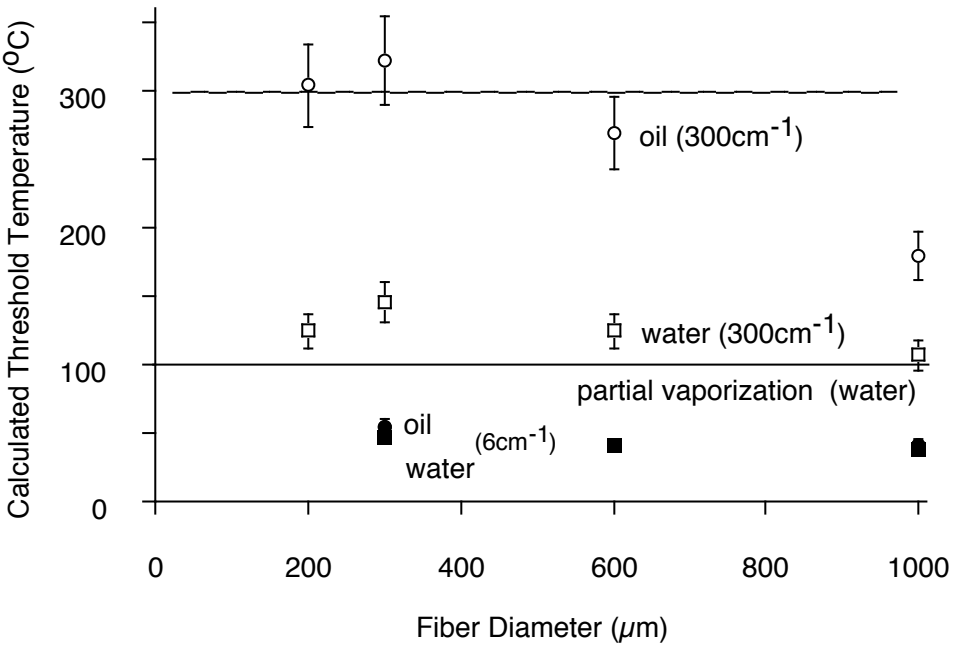

Figure 3.7: Calculated temperature of the liquids at threshold directly using equation (3.8. The solutions with absorption coefficients $6\,\mathrm{cm}^{-1}$ and $300\,\mathrm{cm}^{-1}$. Ambient temperature was assumed to be 25°C. There were no significant differences in the temperature between water and oil at the lower absorption (i.e., $6\,\mathrm{cm}^{-1}$).

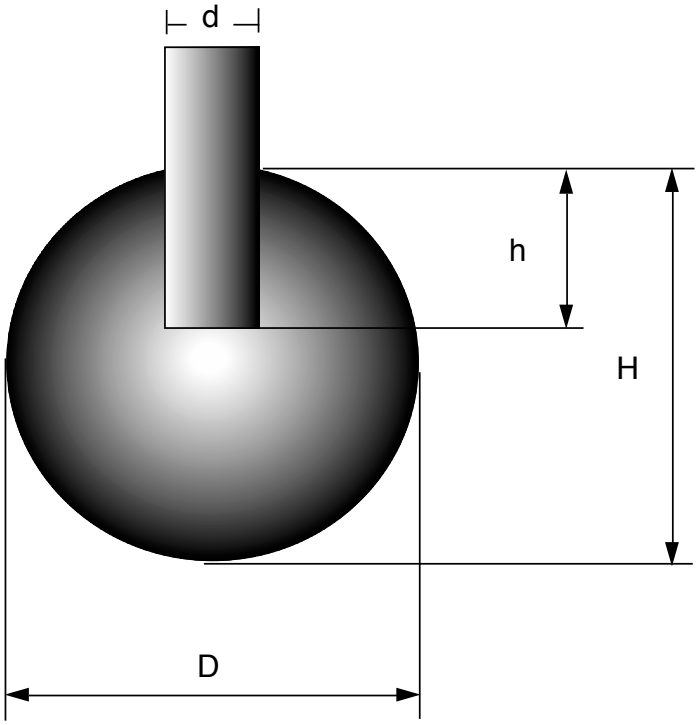

Figure 3.8: Schematic of a cavitation bubble with diameter (D), height (H), fiber diameter (d), and length of the fiber inside the bubble (h). The volume of the bubble is estimated by assuming an axial symmetric ellipsoid with equation (3.9).

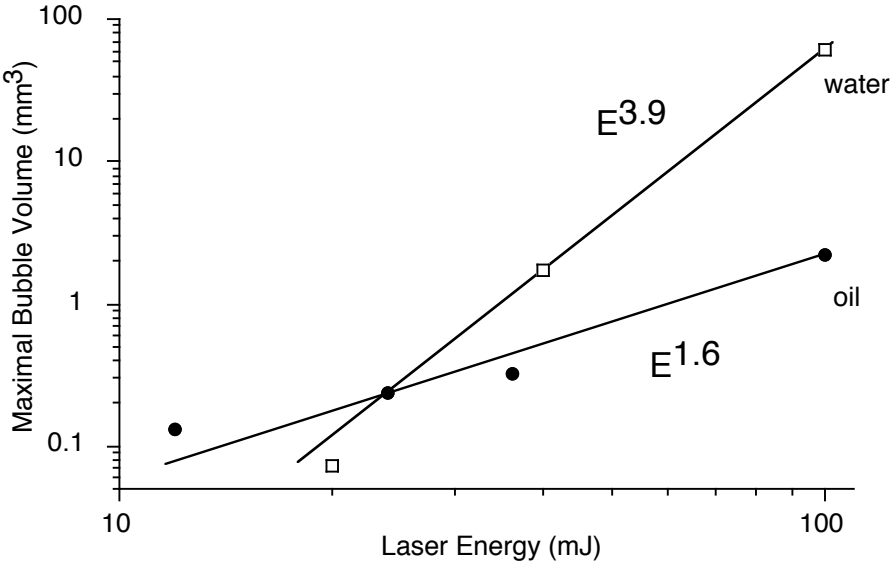

Figure 3.9: Maximum bubble volume as a function of laser energy. Laser pulses were delivered into the solutions at the absorption $100\,\mathrm{cm}^{-1}$ through a $1000\,\mu\mathrm{m}$ fiber.

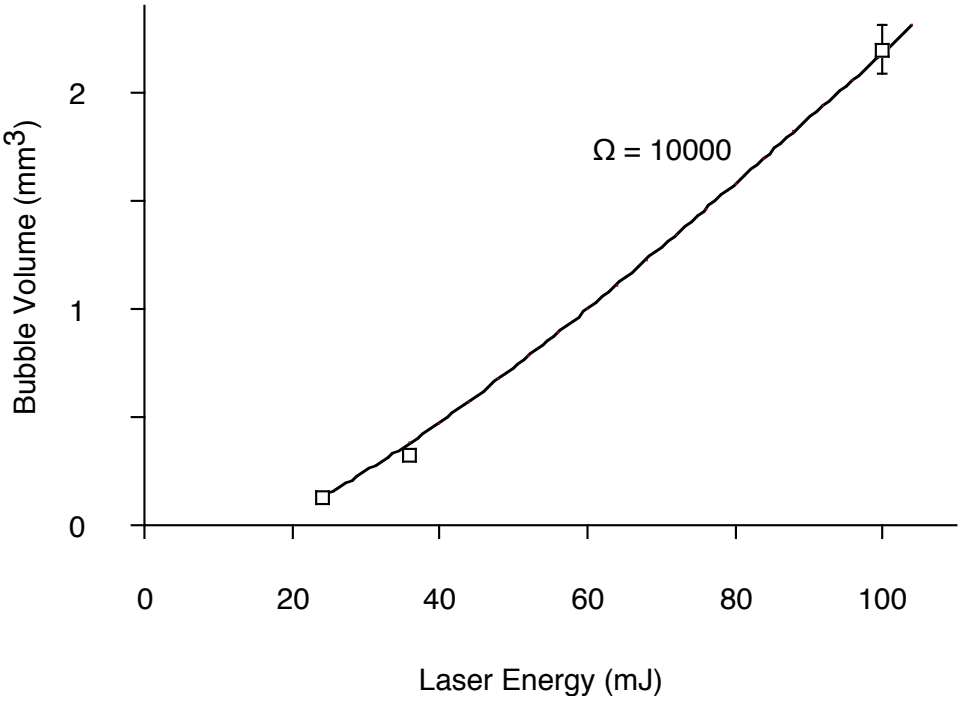

Figure 3.10: Bubble volume as function of laser energy. The open squares represent the experimental results, and the line represents the data estimated by theoretical calculation using equation (3.19) assuming the volume expansion coefficient $\Omega = 10000$. Laser pulses were delivered into a $100\,\mathrm{cm}^{-1}$ oil solution via a $1000\,\mu$m fiber. The measured threshold radiant exposure was $25.3\,\mathrm{mJ/mm}^2$.

Table 3.1: Some physical properties of water and oil.

MATERIAL	density (mg/mm^3)	viscosity (cP)	specific heat (mJ/(mg ℃))	latent heat (mJ/mg)	boiling point (℃)
water	1	0.653	4.2	$2.26 \cdot 10^3$	100
mineral oil	0.86	29.67	1.87	$2.83 \cdot 10^2$	300

Chapter 4

Dynamic Behavior of Laser-induced Cavitation Bubbles in Liquids and on Soft Targets

4.1 Introduction

Cavitation is the formation and activity of bubbles (or cavity) in a liquid [92]. The interest in the dynamics of cavitation bubbles in liquids initially arose from their destructive effects on ship propellers and in hydraulic machinery. Cavitation erosion is attributed to the action of acoustic transients emitted during bubble collapse and to the impingement of the high-speed liquid jet that develops when a bubble collapses into the vicinity of a solid boundary [93]. It was shown that cavitation occurs in a liquid when irradiated with laser light soon after the invention of laser [94]. This form of cavitation is called optical cavitation. Early studies of laser-induced cavitation focused on the investigation of acoustic

transient emission due to plasma formation at the laser focus [95] and the jet formation [96]. Laser-induced bubbles can be high spherically and free from mechanical distortions, thereby facilitating comparison of experimental results with numerical investigations.

Pulsed lasers have been used to induce cavitation or vapor bubbles in ophthalmology, cardiology, and urology. For example, laser pulses are used to produce a plasma with subsequent bubble formation for ocular surgery by photodisruption [97] and laser-induced lithotripsy [98]. Tissue disruption and stone fragmentation are related to the mechanism of cavitation erosion. Laser pulses are also used to remove thrombus in obstructed arteries [1].

Pulsed laser ablation of blood clots in a fluid-filled blood vessel is accompanied by an explosive evaporation process. The resulting vapor bubble rapidly expands and collapses to disrupt the thrombus (blood clot). A study by de la Torre and Gregory demonstrated that laser energy absorption by blood produced rapidly expanding cavitation bubbles and high-pressure acoustic transients of between 10 and 1200 atmospheres [87]. Thus, the laser-induced bubble formation plays an important role in the thrombus removal process.

Previous studies of laser-induced cavitation focused on four topics:

1. the fundamental studies of laser-induced bubble formation: investigations of bubble formation in light absorbing liquids or on absorbing targets [90, 91, 98–101];

2. tissue removal: selective removal of diseased tissue without damage to the

adjacent normal tissue [30, 32, 39];

3. tissue damage: effects of laser parameters on the tissue damage [76,102,103], and

4. effect of pressure on the membrane: enhancement of drug cytotoxicity by laser-induced shock waves [77, 104].

Three methods using laser have been used to generate cavitation or vapor bubbles. The first method generates bubbles by optical breakdown at the focus of the laser beam and the plasma formation [97, 105]. This method is commonly used for intra-ocular microsurgery. For example, Nd:YAG laser has proven so successful at sectioning opacified posterior lens capsules that it has completely replaced the traditional surgical approach for the often equally debilitating secondary cataracts [105]. The second method generates bubbles in light absorbing liquids using optical fiber for pulsed beam delivery, the bubbles are formed at the fiber tip. The third method generates bubbles by delivering pulsed laser light to light absorbing solid targets. The bubbles are formed on the target surface submerged in clear liquids (e.g., water or saline).

These last two methods have been used for laser thrombolysis [1, 106, 107] and the subsequent cavitation phenomena are important for understanding photomechanical drug delivery process. Although several studies have been focused on the laser-induced cavitation or vapor bubble dynamics [90, 91, 99], no detailed study has been done on the dynamic behavior of laser-induced cavitation bubble in light absorbing liquids or on soft targets with the pulsed dye laser. The aims

of this study were

- To elucidate the role of laser energy, radiant exposure, and absorption in the bubble formation at supra-threshold.
- To investigate how the different liquids surrounding a fiber tip or on a target surface affects the bubble formation and how mechanical strength of thrombus affects the removal process.
- To study the effects of boundaries of the fiber and container on the bubble formation to simulate the effect of clinically relevant boundary conditions (vessel walls and the laser catheter) upon cavitation bubble formation or thrombus ablation.

4.2 Materials and Methods

4.2.1 Sample Preparation

Thrombus was simulated using 3.5–5% gelatin (60–300 bloom, Sigma Chemicals). The percentage was determined by the weight ratio of gelatin to water. The bloom number is the standard method for indicating the toughness of gelatins and is a measure of surface tension. Higher bloom numbers indicate stronger gelatins. No attempt was made to correlate the bloom number with the strength of any specific clots in this study, although the range studied was similar to that of typical clot toughness. The gelatin-water mixture was heated to 60°C with stirring until it became clear. Liquid gelatin samples were poured into 1 cm cuvettes and molded to form 2–3 cm thick thrombus models with flat surfaces. Dye

solution (0.07 g of Blue 15 from Sigma in 40 mL water) was placed on the gelatin surface for 5 minutes and a blue layer ($\sim$300 μm thick with a $\sim$100 cm^{-1} absorption coefficient at 577 nm) was formed. At 504 nm, 300 cm^{-1} gelatin samples were made by adding 0.3 g of Direct Red 81 from Sigma in 100 mL of liquid gelatin (3.5% 175 bloom).

Solutions of water or mineral oil containing a light absorbing dye (Direct Red 81 or D&R #17) were used as light absorbing liquids. The absorption was controlled by varying the amount of dye in the solutions. The details of making these solutions were described in Chapter 3.

4.2.2 Laser Radiation

Laser irradiation at 504 or 577 nm was provided by flashlamp excited dye lasers (Palomar Medical Technologies). The pulse duration was $\sim$1.3 μs (full width at half maximum). The laser pulses were delivered into absorbing liquids or through clear liquids onto thrombus phantoms via a fused-silica fiber with diameters 300 and 1000 μm. The energy per pulse was measured with an joulemeter (Molectron). Pulse-to-pulse energy variation was less than 5%.

4.2.3 Photographic Systems

Two photographic systems were used to visualize the bubble formation. A time-resolved flash photographic setup provided a series of single stroboscopic pictures, while a high-speed framing camera captured 12 images for one single event. The bubble sizes were measured directly from the images by using the

optical fiber in each image as a scale factor. The images were analyzed using NIH Image or IP Lab software.

Flash Photography

The microsecond time-resolved flash photography setup is shown in Figure 4.1. The processes taking place at the fiber end or on the gelatin surface were photographed using a triggerable CCD camera (CV-251, Protec). A stereomicroscope (SZ60, Olympus) was used for magnification. Each picture was a single event and was repeated three times for each parameter set. The bubble size was reproducible to 5% before the bubble collapse. The appearance of cavitation bubbles varied widely after the bubble collapse. A strobe (MVS–2601, EG&G) with a 5 μs pulse duration (full width at half-maximum) was used for illumination. The delay times were controlled by a digital delay generator (DG535, Stanford Research Systems). The generator was triggered by the laser pulse by using a photodiode (UDT Instruments) that was attached to the laser delivery fiber, so flash photographs were taken at variable delay times of 5–500 μs after the laser pulse. A laser filter was positioned in front of the microscope to avoid blinding the CCD camera.

High-speed Shadowgraphy

Figure 4.2 shows a schematic of the high-speed photographic system. A continuous-wave argon ion laser at 514 nm was used for illumination. The laser beam was expanded to 10 mm diameter using a 3× beam expanding telescope for illuminating the sample area. A shadowgraph of the sample surface and optical

fiber was imaged on the input of an electronic framing camera (FS501, Ultranac). By properly timing the pulsed-dye laser and argon ion laser with the triggering of the electronic framing camera, multiple exposures of the interaction of the laser pulse with the thrombus could be realized. The ablation process could be examined from start as early as several hundred nanoseconds to several hundred microseconds after the laser pulse. The electronic framing camera captured 12 pictures with an adjustable interframe time. The photographs were taken with one microsecond exposure time and 25 microsecond interframe time. The 12 frames were captured on a 1152×770 pixel CCD chip with the image read directly into a PC for data analysis. The illumination light was adjusted using a neutral density wheel (50G00AV.2, Newport).

4.2.4 Experiments

Effects of Laser Energy, Absorption, and Radiant Exposure

In a previous chapter I established the thresholds for bubble formation in absorbing liquids. The results demonstrated that the thresholds increased with decreasing absorption coefficients and were relatively independent of the fiber size. The goal of this experiment was to investigate the role of excess laser energy on bubble formation in the solutions with varied absorptions at supra-threshold energies when fibers of different sizes were used for laser delivery. The bubble dynamics in absorbing liquids were visualized with the flash photographic setup, and the laser-induced acoustic pressure waves were measured with a piezoelectric polyvinlyidenefluoride (PVDF) transducer (Hydrosonics) that was placed under

the transparent container filled with the light absorbing liquids.

Laser pulses of 30–100 mJ (4–13 times above the threshold energies) were delivered into a 300 cm^{-1} oil solution through a fiber with a diameter of 1000 μm for the energy effect experiment, while single laser pulses of 100 mJ were delivered into the medicated oil solutions with absorption coefficients (50–300 cm^{-1}) for the absorption effect experiment. The effect of radiant exposure was investigated by using fibers (300–1000 μm) to deliver laser pulses with the same radiant exposure into a 300 cm^{-1} oil solution, such that the energies varied from about 8–13 times above the threshold energies (i.e., 9 mJ via a 300 μm fiber, 36 mJ via a 600 μm fiber, and 100 mJ via a 1000 μm fiber). The bubble sizes (widths) were measured as functions of delay time for different laser energies, absorption coefficient, and fiber sizes respectively. A theoretical analysis of the bubble volumes was correlated with measured bubble volumes. The bubble volumes were calculated using equation (3.19) with the data in Table 3.1.

Acoustic measurements were conducted to correlate the acoustic pressure waves with the bubble sizes, such that no quantitative analyses of the pressures were made. The acoustic signals were recorded on a digital storage oscilloscope (DSA 602A, Tektronix). A typical acoustic transducer signal is shown in Figure 4.3. The oil solutions were selected because they were used as drug models for *in vitro* experiments of photomechanical drug delivery (see Chapter 6).

Effects of Materials

Three experiments were performed to investigate the effects of materials:

1. Does viscosity and density of absorbing liquids affect the bubble size formed in absorbing liquids?

2. What are the differences when the bubble forms on a soft target covered with the liquids?

3. Does the mechanical strength of the ablation targets affect the bubble dynamics?

In the first experiment, single pulses of 100 mJ were delivered into an oil solution or water solution through a 1000 μm fiber. The absorption coefficient for both solutions was 300 cm^{-1}. The solutions filled a 3 mm diameter silicone tube and the fiber was centered inside the tube. The laser emitted light with a wavelength 504 nm.

In the second experiment, two sets of experiments were performed. The first set used single pulses of 50 mJ were delivered onto 100 cm^{-1} gelatin through clear water or clear oil via a 300 μm fiber placed 1 mm above the gelatin surface. The bubble formation was visualized using high-speed shadowgraphy. The laser emitted 577 nm light. The second set used 100 mJ laser pulses to irradiate the gelatin sample (300 cm^{-1}) through clear water, clear mineral oil (Paddock Lab), and clear contrast medium (MD-76, Mallinckrod Medical, Inc.) using a 1000 μm fiber that was 1 mm away from the gelatin surface. The bubble width was measured 300 μs after the laser pulse with flash photography. The laser operated at 504 nm. The density and viscosity for water, mineral oil, and contrast medium are summarized in Table 4.1.

The third experiment visualized the bubble formation on $100\,\mathrm{cm}^{-1}$ gelatin with different mechanical strengths. Single pulses of 50 mJ pulse were delivered via a $300\,\mu$m fiber onto a gelatin sample ($100\,\mathrm{cm}^{-1}$) with varied hardness (3.5% 60 bloom and 5% 300 bloom) under water. The fiber tip was 1 mm above the gelatin surface and centered inside 1 cm cuvette. The laser operated at 577 nm. I also investigated the effect of mechanical strength on bubble formation when the fiber tip was slightly in contact with the gelatin surface. Single pulses of 100 mJ operating at 504 nm was delivered via a $1000\,\mu$m fiber onto a clear gelatin sample (3.5% 60 bloom and 3.5% 300 bloom) covered with a $300\,\mathrm{cm}^{-1}$ oil solution.

Boundary Effects

In a previous chapter I proposed that the use of a smaller fiber for laser delivery may benefit the clinical applications because of the lower energy needed. However, it is unclear whether the bubble generated by a smaller fiber can produce the same hydrodynamic pressure as that created by a larger fiber with higher energy when the bubble diameters are similar. Thus, an experiment was performed to investigate the effect of fiber configuration on bubble formation and acoustic pressures. The laser pulses were delivered into the oil solution ($300\,\mathrm{cm}^{-1}$) through 300, 600, and $1000\,\mu$m fibers, and the pulse energy was varied, such that bubbles of same size could be produced. Consequently, the experiment was performed in a silicone tube with a 3 mm inner diameter as a blood vessel model using the energies that could create bubbles of the same width for a $300\,\mu$m fiber and a $1000\,\mu$m fiber.

The effects of boundaries were also investigated through comparing the bubble dimensions generated by different size fibers (300, 600, and 1000 μm) with different boundary conditions (i.e., a 52×52×50 mm-bottle, 1 cm-cuvette, and 3 mm-silicone-tube). A series of experiments were performed with the same parameters as those described in section 3.4.1 in a 1 cm cuvette instead of the plastic bottle.

4.3 Results

4.3.1 Effects of Laser energy, Absorption, and Radiant Exposure

Figures 4.4 and 4.5 show the plots of the bubble dimension (width) as a function of delay time for different laser energies and absorption coefficients of the solutions. As expected, the bubble sizes increased as both the laser energy and absorption coefficient increased. The first collapse was observed at pulse energies above 60 mJ in the 300 cm^{-1} oil solution. Note that the time of maximum bubble size was half of the first collapse time for a larger bubble (e.g., at 100 mJ), while the time of the maximum bubble size was shortened for the smaller bubbles. Figure 4.6 shows that the bubble sizes were proportional to the fiber sizes at a constant radiant exposure. The constant radiant exposure was achieved by increasing the area of the delivery fiber with increasing the total energy, i.e., more energy was delivered for larger fibers.

Acoustic pressure measurements showed that the acoustic pressure increased with increasing bubble size and pulse energy (Figures 4.7 and 4.8). The acoustic

signal also increased with increasing absorption coefficient. Increases in the acoustic signals were faster from 75–210 mJ/mm^2 than those from 210–850 mJ/mm^2 (Figure 4.8). The amplitudes of the maximum signals increased by a factor of 3.5 when the radiant exposure increased from 75–210 mJ/mm^2. However, it only increased by a factor of 1.4 as the radiant exposure increased from 210–850 mJ/mm^2. It can also be seen that the acoustic pressures were greater for the smaller fibers than for larger fibers at equal laser energy (Figure 4.8).

The bubble volumes were estimated using equation (3.19). The ratio of bubble volume and surface area of the fiber tips as a function of the ratio of radiant exposure over measured threshold radiant exposure is plotted in Figure 4.9. The solid lines were least square curve fits according to equation 3.19 and the correlation coefficient R = 0.99. Note that the volume expansion coefficient, Ω, varied as much as a factor of 4. A volume expansion coefficient Ω of 10000 seems to be better for smaller bubbles, while a volume expansion coefficient Ω of 38000 may be a better parameter for the larger bubbles.

4.3.2 Effect of Materials

Figure 4.10 shows the bubble dimensions (width and height) generated on the absorbing gelatin surface under clear water and oil. There were no significant differences in bubble sizes formed on the gelatin under water or oil. The bubble heights did not differ significantly from the widths. Note that the bubble in water grew faster initially ($\sim$25 μs) and at 50 μs they matched. Flash photographs revealed that the bubble dimensions formed under water, oil, and contrast medium

were quite similar each other. The measurements are summarized in Table 4.1. I observed that a stream of color released from the absorbing gelatin surface when the contrast medium interacted with the gelatin samples. This was not observed for water and oil.

Figures 4.11 and 4.12 show in side view the behavior of a bubble generated on absorbing gel surface with different mechanical strength using the flash photography setup, while two series of high-speed shadowgraphs are shown in Figures 4.13 and 4.14. In the case of soft 3.5% 60 bloom gelatin, the bubble shape was spherical during expansion and contraction. The bubble reached its maximal dimension about 100 μs after the laser pulse, and then started to contract slowly (Figure 4.11). The collapse occurred about 300 μs after the laser pulse. The bubble shape became elliptical between 150 and 200 μs after the laser pulse when the harder 3.5% 300 bloom gelatin was used (Figure 4.12). The first collapse was observed at about 250 μs and then slightly rebounded. The second collapse occurred between 400–450 μs. The second collapse occurred between 400–450 μs. The gelatin ejected from the surface afterwards. Similar bubble behavior was observed from the high-speed shadowgraphs (Figures 4.13 and 4.14). The bubble widths from Figures 4.13 and 4.14 are plotted as a function of delay time in Figure 4.15. These shadowgraphs confirmed that the series of isolated stroboscopic pictures could be used to characterize the bubble formation even though the process may vary from shot to shot and from sample to sample.

Figures 4.16 and 4.17 show the effect of material mechanical strength on the bubble formation when the fiber tip slightly contacted the gelatin surface.

Evidently, the bubble more easily penetrated into the soft gel than the hard one (Figure 4.16). The resistance from the harder gelatin pushes the collapsing bubble back to the surface (Figure 4.17).

4.3.3 Boundary Effects

Figure 4.18 shows laser-induced bubbles formed in a $300\,\mathrm{cm}^{-1}$ oil solution with the same width. The pulse energy needed to create bubbles of the same size increased with increasing the fiber size. The bubble shape changed from almost spherical to a more widened elliptic shape as the fiber size increased. Two compiled sequences of bubble growth and collapse with different fibers are shown in Figures 4.19 and 4.20. The first collapse for the $300\,\mu$m fiber was of $\sim 300\,\mu$s and then rebounded to a second maximum size at $400\,\mu$s. The second collapse occurred $525\,\mu$s after the laser pulse. Eventually, the bubble left the fiber and migrated forwards. The bubble dynamics for a bubble generated by a $1000\,\mu$m fiber differed from that created by the $300\,\mu$m fiber (Figure 4.20). The bubble size at first collapse ($\sim 260\,\mu$s) was larger than that of the $300\,\mu$m fiber and left the fiber tip faster than that of the $300\,\mu$m fiber. The acoustic measurements revealed that bubbles of similar size could generate the similar maximal acoustic pressure (Figure 4.8).

Figures 4.21 and 4.22 show the bubble formation in a $300\,\mathrm{cm}^{-1}$ oil solution confined in a 3 mm silicone tube. There were no differences in the maximal tube wall diameter due to the bubble expansion and minimal diameter caused by the collapse between the two cases. In both cases, the bubble reached its

maximum size 50 μs after the laser pulse and dilated the tube wall by 10%. The subsequent bubble collapse caused a 4% invagination of the tube wall. Figure 4.23 shows the bubble expansion and collapse (top panel) in an unbounded 300 cm^{-1} water solution. The maximal dilation of 29% was 60 μs and the tube diameter was reduced by 13% at 900 μs due to the collapse (bottom panel). Note that the maximum bubble width formed in the water solution was larger than that formed in the oil solution by a factor of 1.8 (i.e., 3.9 mm in water and 2.2 mm in oil) using the same laser energy (in this case, 100 mJ) and resulted in significant differences in the dilation and invagination of the tube wall (Figures 4.22 and 4.23).

The effect of container boundary on the bubble dimension for different energies and absorptions is shown in Figures 4.24 and 4.25. There was no difference in bubble size for laser energies below 60 mJ in a 300 cm^{-1} oil solution (Figure 4.24A), although the times of the maximum bubble size were different (Figure 4.24B). The bubble dimensions and the corresponding times were also different when the bubbles were formed in oil solutions with varied absorption coefficients (50–300 cm^{-1}), shown in Figure 4.25. The maximal bubble diameter (2.7$\pm$0.2 mm) formed in the tube was similar to that in cuvette (2.4$\pm$0.2 mm), but it was only 84% of that in the semi-infinite medium (i.e., in a 52$\times$52$\times$50 mm-bottle).

4.4 Discussion

The objective of this study was to characterize the laser-induced cavitation phenomena that take place in absorbing liquids and on soft targets. The dynamic

behavior of the vapor bubble was visualized using time-resolved flash photography and high-speed shadowgraphy, and the acoustic pressures were measured using a PVDF transducer to correlate the acoustic pressures with the bubble dimensions.

4.4.1 Effects of Laser Energy, Absorption, and Radiant Exposure

The results of this present study demonstrated that the bubble dimensions depended on the laser energy and absorption coefficient. The bubble sizes increased with increasing laser energy and absorption. The excess laser energy resulted in larger short lived bubbles ($\sim 300\,\mu$s). This demonstrated the applicability of two methods for decreasing bubble dimensions: decreasing pulse energy and diluting surrounding liquids, i.e., decreasing the absorption coefficient. The effects of radiant exposure seem to more complicated than those of laser energy and absorption. Figure 4.6 shows that the bubble sizes are larger for larger fibers and smaller for the small fibers at a constant threshold radiant exposure. The energy varied by a factor of 4–11, and larger fibers needed more energy than that needed by the smaller fibers. It seems that the pulse energy dominates the bubble dimension. However, bubbles of the same size could be created by a small fiber (i.e., $300\,\mu$m fiber) using lower energy (33 mJ) or a larger fiber (e.g., $1000\,\mu$m fiber) using higher energy (100 mJ). This result suggests that the bubble dimension was, somehow, governed by the radiant exposure. I hypothesize that there is a threshold effect, i.e., the bubble formation will be governed by laser energy

below this threshold, while the radiant exposure dominates the bubble dimensions above this threshold. However, it is unclear whether the laser energy will dominant the bubble dynamics above a certain value, i.e., the bubble dimension would be independent of the fiber configuration as long as the same pulse energy is delivered.

In a previous chapter, I proposed a theoretical model to analyze bubble volume (see Appendix in Chapter 3). To verify the applicability of this model, the calculated bubble volumes were compared with those measured. The range of parameters was relatively large. The delivered laser energy per pulse ranged from 9–60 mJ (about 4–8 times above the threshold energy). The absorption coefficient of the oil solution was varied from 50–300 cm^{-1} (a factor 3) and the surface area of the fiber tip varied from 0.071–0.785 mm^2 (a factor 11). The ratio of input radiant exposure and the measured threshold (F_o/F_{th}) was about 10. The results revealed that the estimation of bubble volumes would be off by a factor of 4 due to the variation of the volume expansion coefficients (10000–38000). This may indicate that the volume expansion factor Ω is dependent of the initial volume of the vaporized oil that may depend on the latent heat. Furthermore, the latent heat of oil is a function of temperature [108]. The results of the preceeding chapter showed that the threshold temperature varied from 90–350°C, such that the latent heat would change by a factor of 2.

A study by van Leeuwen *et al.* demonstrated that the volume expansion factor varied by a factor of 1.6 for the excimer laser-induced vapor bubble formed in

hemoglobin solution [90]. In their study, single pulses of 1.25–51 mJ were delivered into hemoglobin solutions (40–320 cm^{-1}) through fibers (300, 550, or 950 μm diameter) and the thresholds were calculated using the partial vaporization theory. The ratio of incident radiant exposure F_o and theoretical threshold F_{th} was restricted to 10. The volume expansion factor ranged from 3400–5400. A similar study by Jansen *et al.* also showed that the volume expansion coefficient was not a constant for bubble formation using mid-infrared lasers and the best fitting volume expansion factors were about 820 for Ho:YAG laser (2.12 μm) and 729 for Tm:YAG laser (2.01 μm) respectively [84].

The variation of volume expansion coefficient Ω reduced to a factor of 2 after the variation of latent heat was taken into account for the calculation. This discrepancy between the experimental and the theoretical values (by a factor of 2) may be caused by the physical properties of the mineral oil since it was a mixture of several different components and carbonization always occurs when part of the oil was super heated by the laser pulse. Furthermore, it is unclear what the temperature really was at supra-threshold energy, which may also cause misestimation of the latent heat. In comparison with previous studies [84, 90], this model is useful for predicting the bubble dimension.

4.4.2 Effects of Materials

Photoacoustic drug delivery uses the hydrodynamic pressure following the laser-induced bubble expansion and collapse to deliver the drug into thrombus during laser thrombolysis procedure. The bubble is formed on the thrombus

covered with clear fluids (e.g., saline and contrast). One concern is whether the density and viscosity affect the bubble dynamics. This study demonstrated that the effects of density and viscosity of the liquids above the target on the bubble formation are negligible when the bubble formed on an ablation target (Figure 4.10 and Table 4.1). The mechanical strength of the target material does affect the bubble dynamics (Figure 4.15). The bubble dynamics strongly depended on the physical properties of the absorbing liquid when the bubble was formed in an absorbing liquid (Table 4.1). These findings suggest that the properties of the liquids dominate the bubble formation as the laser energy is absorbed by the absorbing liquids, while the bubble formation is governed by the properties of the targets if the laser energy is absorbed by the target. In brief, the dynamics of bubble formation depends on where the bubble is formed due to the absorption of laser energy by absorbing liquids or soft targets.

The flash photographs revealed that the larger bubble formed in water could cause greater dilation of the tube wall (Figures 4.22 and 4.23). A study by de la Torre and Gregory suggested that laser-induced cavitation bubble could cause dissections in vascular tissue during pulsed-dye laser angioplasty [109]. Reducing bubble dimensions has been proposed to minimize the photomechanical effect [89–91]. This study suggests that the bubble size may be reduced by using a liquid in which small bubbles are formed like oil rather than water.

The density and viscosity of clear liquids do not affect bubble dynamics significantly when the bubble is formed on gelatin. This implies that the bubble formation depends on the material properties of the ablation target. This finding

suggests that photomechanical drug delivery may be achieved by using any drugs that are suitable to dissolve the thrombus during laser thrombolysis regardless of the density and viscosity of the drug.

Previous studies have demonstrated that the mechanical properties of tissue significantly affect the ablation rate and the bubble formation [85, 91]. However, there is no evidence available to show that the mechanical strength of the thrombus affects the bubble dynamics. This study provided evidence that the mechanical strength of the ablation targets affects the bubble dynamics and suggests that the mechanical strength of the thrombus should be considered when modelling the bubble dynamics during laser thrombolysis and photomechanical drug delivery.

The bubble behavior became closer to that formed on solid targets and the bubble oscillation was observed for the bubble formed on a harder gelatin (e.g., 3.5% 300 bloom gel) shown in Figure 4.12, while the ejection of materials always followed the bubble collapse for those formed on a soft gelatin (e.g., 3.5% 60 bloom gel) shown in Figure 4.11. The bubble shape was also affected by the mechanical strength. For example, the bubble formed on soft gelatin kept an almost spherical shape until its collapse (Figure 4.13), and that formed on harder gelatin was pushed back to the surface due to the resistance from the gelatin (Figure 4.14). The maximal bubble volume was similar for both cases although the bubble dynamics were significantly different. A possible explanation for this phenomena was that the bubble had enough energy to overcome the resistance from the harder gelatin during the expansion phase, and then the pressure inside

the bubble decreased fast and eventually became smaller than the resistance and pressure of the surrounding liquid. Consequently, the bubble was pushed back to the surface, since the resistance from the water above the gelatin surface was much smaller than that from the gel. In brief, the bubble would migrate to a place where there is less resistance. One experimental result provided an evidence to support this explanation. When the bubble formed on plastic plate under clear water, only a hemispherical bubble was observed, shown in Figure 4.26.

Evidently, when the bubble formed inside the gelatin the effect of mechanical strength would be more effective (Figures 4.16 and 4.17). A study by Jansen *et al.* demonstrated that bubble dimensions formed in an 84% gelatin (in their case, 84 percent of water in the gel) were always smaller than those formed in water regardless of the pulse duration with a Ho:YAG laser [91].

4.4.3 Boundary Effects

The results of this study showed that bubbles of the same size could be created using fibers of different size (Figure 4.18), but the bubble shape changed from almost spherical to a more widened elliptic shape with increasing fiber size. Furthermore, the dynamic behaviors of these two bubbles looked different (Figures 4.19 and 4.20). The bubbles generated by a smaller fiber (300 μm) could contract to a smaller size than those for a larger fiber (1000 μm). This may be caused by the physical size of the fiber tip.

The bubbles of the same size created using different fibers with different energies could generate the same mechanical effects on dilation and invagination of a

3 mm silicone tube wall. The acoustic transient measurements also showed that similar acoustic pressure waves could be generated in this manner. This finding suggests that photomechanical drug delivery can be achieved by use of smaller fiber with lower energy.

The results of the present study demonstrated that the bubble formation was also affected by the surrounding space. The bubbles formed in a plastic bottle were larger than those formed in a 1 cm cuvette (Figures 4.24 and 4.25). I found that the bubble formed in the 3 mm tube was similar to that formed in the cuvette although the space surrounding the bubble was significant different. This may be due to the fact that the rigid wall of the cuvette forced the moving liquid back to the bubble while the flexible tube wall allowed the bubble to expand, resulting in dilation of the tube wall. About 34% of the bubble energy was dissipated in the dilation of the tube wall or displacement of liquid in the cuvette. This estimation was made using Rayleigh's bubble formula [97, 98, 110]: $E_{bubble} = 4/3\pi\ R_{max}^2\ \Delta p$, where E_{bubble} is the energy of the bubble and Δp is the difference between inner and outer pressure, by assuming $\Delta p = 1000$ kPa (the hydrostatic pressure) in both cases, in the plastic bottle and tube or cuvette.

4.4.4 Implications

This study suggests that photomechanical drug delivery can be achieved selectively by use of different strategies to generate the laser-induced hydrodynamic pressures in fluid-filled vessels. One is to generate bubbles on the thrombus due to the absorption of laser energy by the thrombus in coincidence with injection

of drug. In this case, the effect of drugs with different physical properties on the bubble formation will be negligible. The other method is to create bubbles in surrounding liquids (saline or blood) and the bubble dimension can be controlled by either the properties of the fluids or using different laser parameters.

It has been shown that the rapidly expanding and collapsing bubble induced by pulsed-dye laser radiation can cause perforation, dissection and other unwanted tissue effects [41, 87]. However, the hydrodynamic pressures arising for the bubble expansion and collapse would be harnessed under controlled circumstances for photomechanical drug delivery. Currently, two strategies to reduce the bubble dimensions are clinically used. One of the strategies is called multiplexing [111]. This method uses a multifiber catheter to generate a number (8–12) of smaller laser pulses (with the same radiant exposure) by consecutively delivering laser pulses at different sectors of the catheter. Equation (3.19) shows that the bubble volume is proportional to the surface area of the fiber tip at a constant radiant exposure. However, the reduction of the surface area of the fiber tip by a factor of 8 only results in decreasing the bubble diameter by a factor of 2. The other method is to dilute the blood by applying a saline flush during laser procedure [112].

This study provided evidence that bubbles of the same size could result in similar hydrodynamic pressure. This finding demonstrated that a small fiber could be used to create the same displacement of intravascular fluids with lower energy as that created by a larger fiber with higher energy proposed in Chapter 3.

4.5 Conclusion

In this chapter, experimental evidence that similar hydrodynamic pressures could be generated using a small fiber with lower energy rather than using a larger fiber with higher energy has been shown. The theoretical model proposed in a previous chapter was applicable to estimate the bubble volume. The volume of laser-induced bubbles increased as the laser energy and absorption coefficient increased. The bubble formation was relatively independent of the liquid properties when the bubbles were formed on the ablation targets under clear liquids. The bubble formation in absorbing liquids strongly depended on the material properties. The mechanical strength of the ablation targets affected the bubble geometry, and the bubble became more elliptical after it reached its maximal dimension for the harder targets. The high-speed shadowgraphs showed that the series of individual stroboscopic pictures could be used for the characterization of the cavitation events, although it took at least 12 times longer to photograph the process using the flash photographic setup than using a high-speed electronic framing camera.

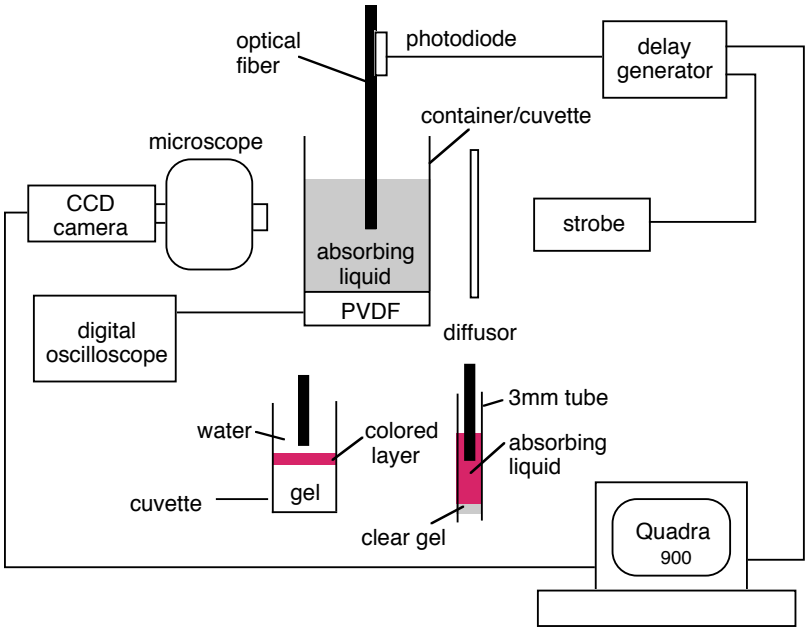

Figure 4.1: Schematic of experimental setup for flash photography and acoustic measurement.

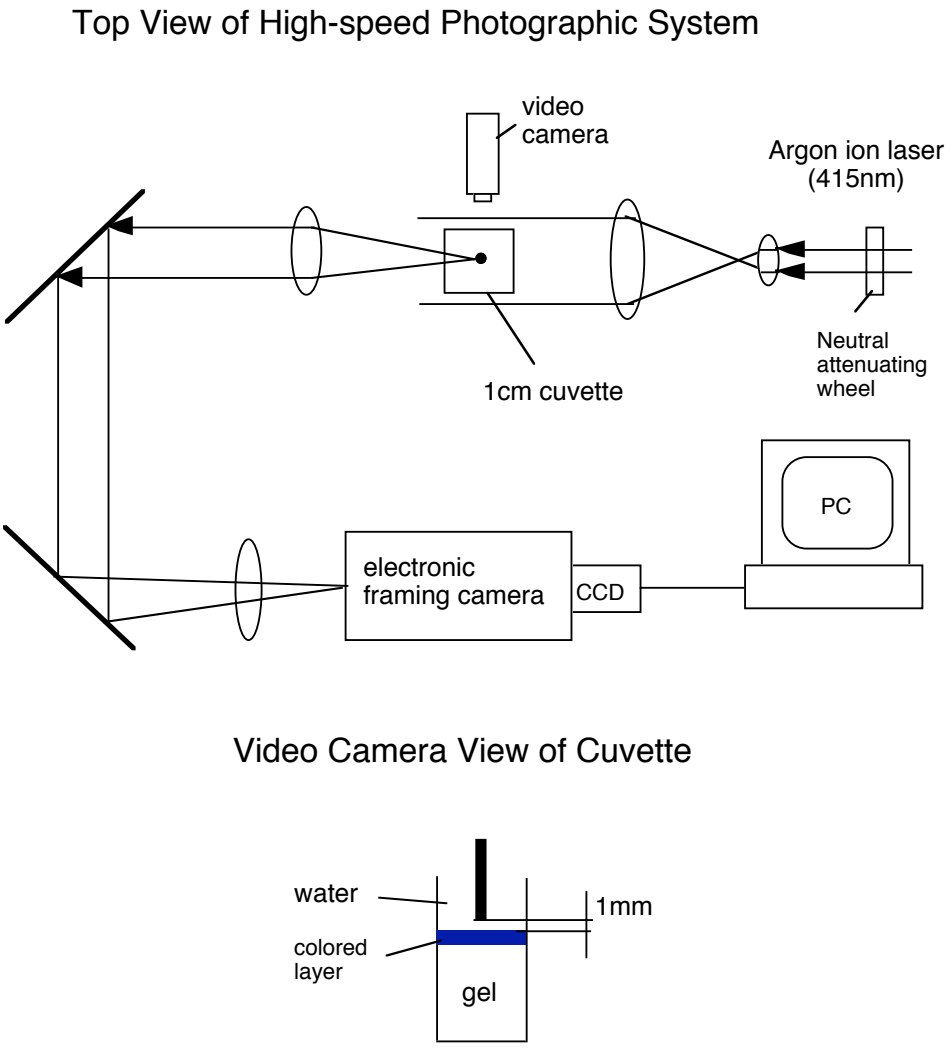

Figure 4.2: Schematic of high-speed photographic system.

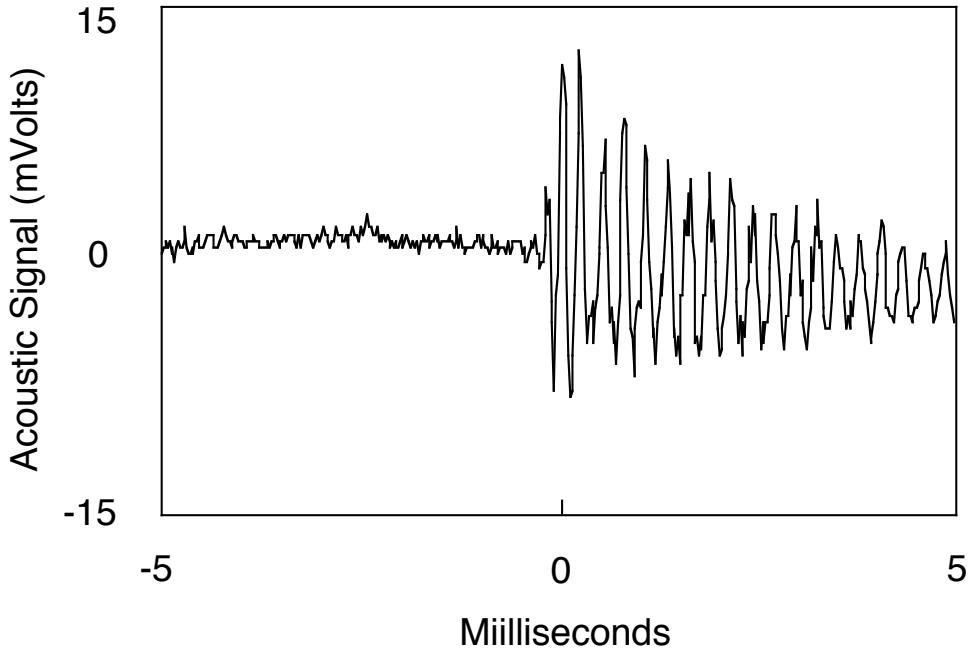

Figure 4.3: Acoustic signal due to bubble formation in an absorbing liquid by a one microsecond laser pulse. The acoustic signal was detected by placing a PVDF transducer under a plastic bottle filled with the absorbing liquid. The transducer signal was amplified and then was displayed on an oscilloscope.

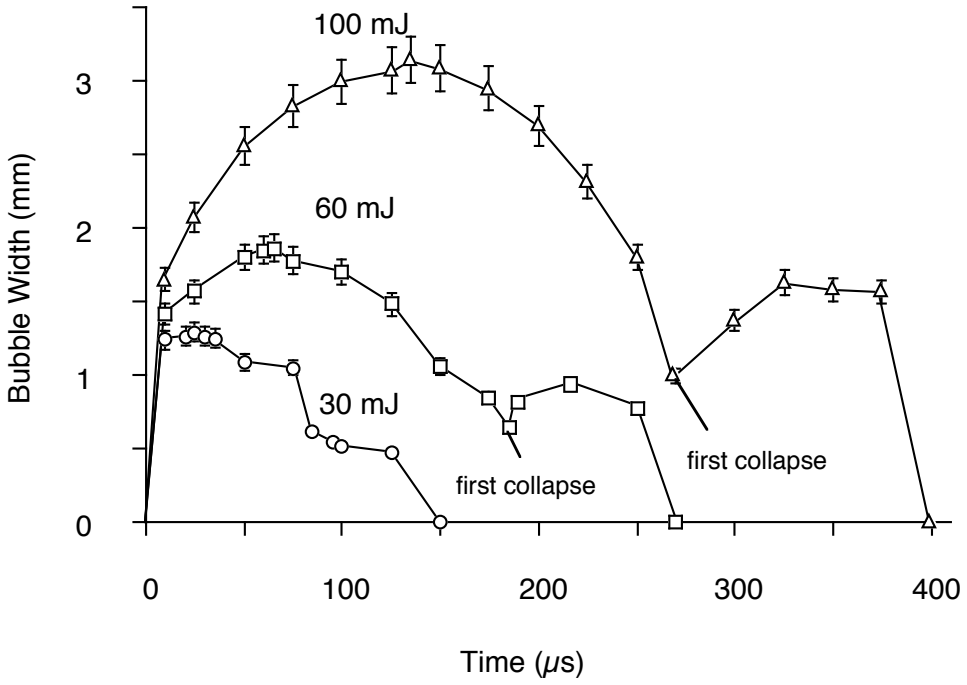

Figure 4.4: Measured bubble width as a function of delay time after the laser pulse using different pulse energies. Plotted data are the average of three measurements. Error bars represent the standard deviation. Laser pulses were delivered into a $300\,\mathrm{cm}^{-1}$ oil solution via a $1000\,\mu$m fiber.

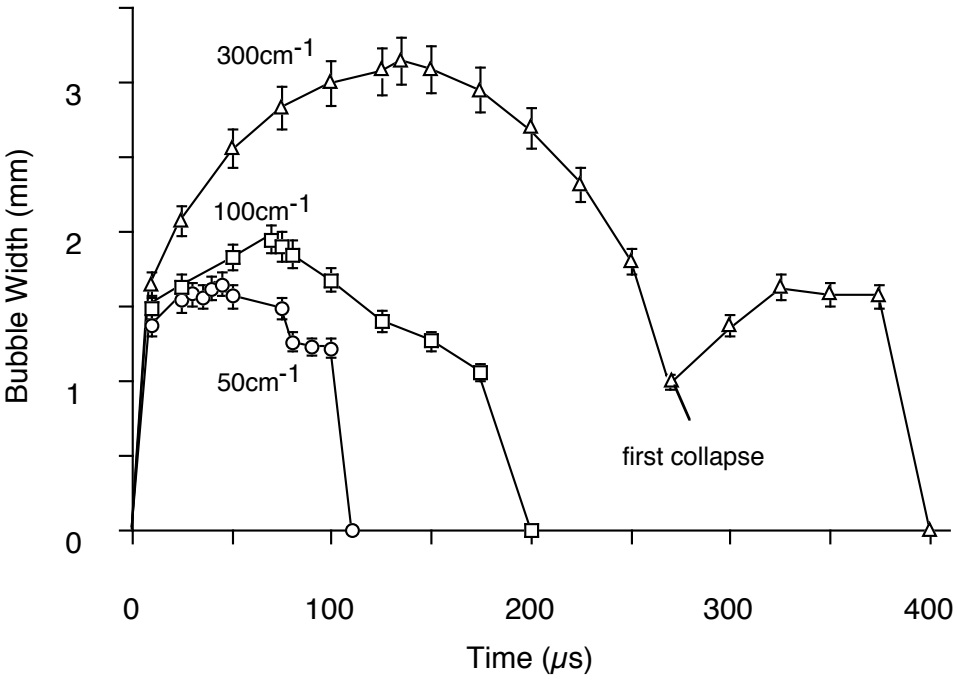

Figure 4.5: Bubble growth and collapse after the laser pulse. Plotted data are the average of three measurements. Error bars represent the standard deviation. 100 mJ pulses were delivered into the oil solutions through a 1000 μm fiber.

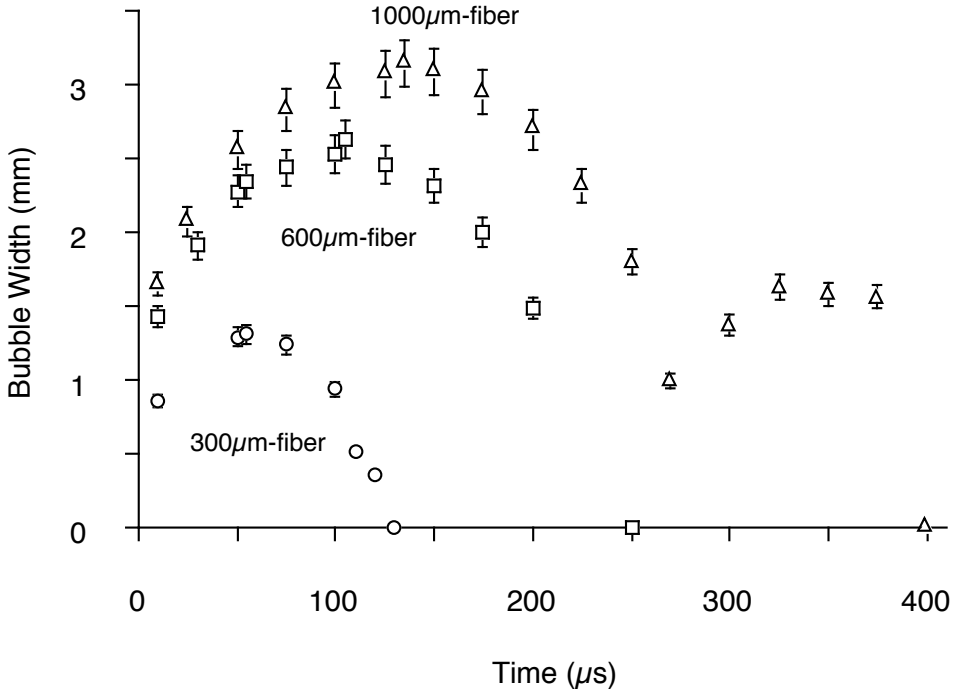

Figure 4.6: Bubble width as a function of delay time after the laser pulse for different fibers at constant radiant exposure ($127\,\mathrm{mJ/mm^2}$). Plotted data are the average of three measurements. Error bars represent the standard deviation. Laser pulses of 9–100 mJ were delivered into a $300\,\mathrm{cm^{-1}}$ oil solution through fibers of 300–1000 μm respectively. Some error bars are smaller than the symbols.

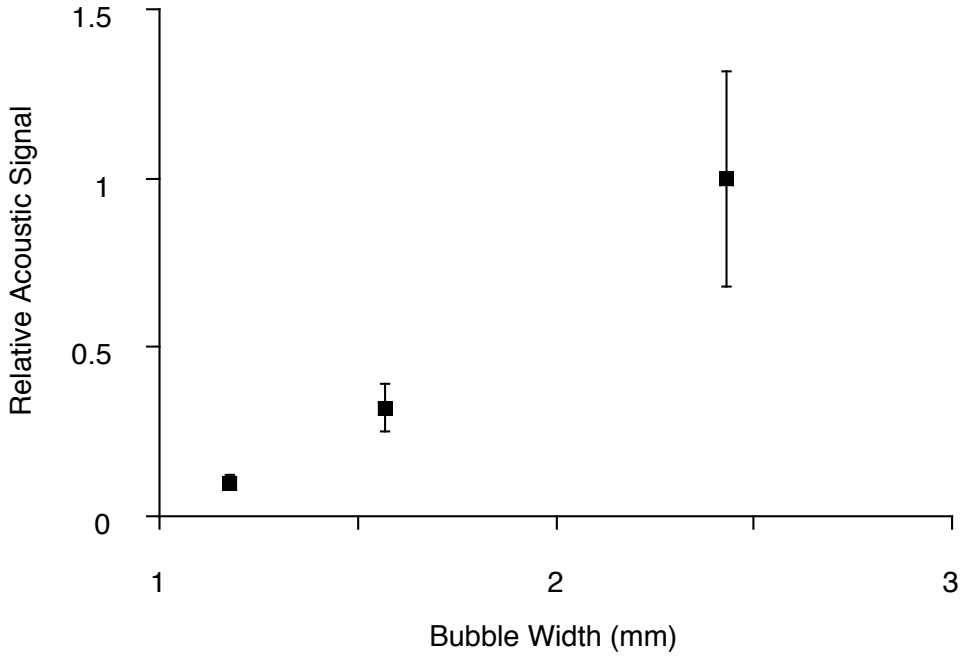

Figure 4.7: The cavitation bubble width versus relative acoustic signal (normalized to the value measure at 100 mJ laser energy via a 1000 μm fiber). The absorption coefficient was 300 cm^{-1}. Single pulses of 30–100 mJ laser energy were delivered through a 1000 μm fiber. The acoustic signal errors are the standard deviation of 5 measurements. The standard deviation for the bubble width was smaller than the squares.

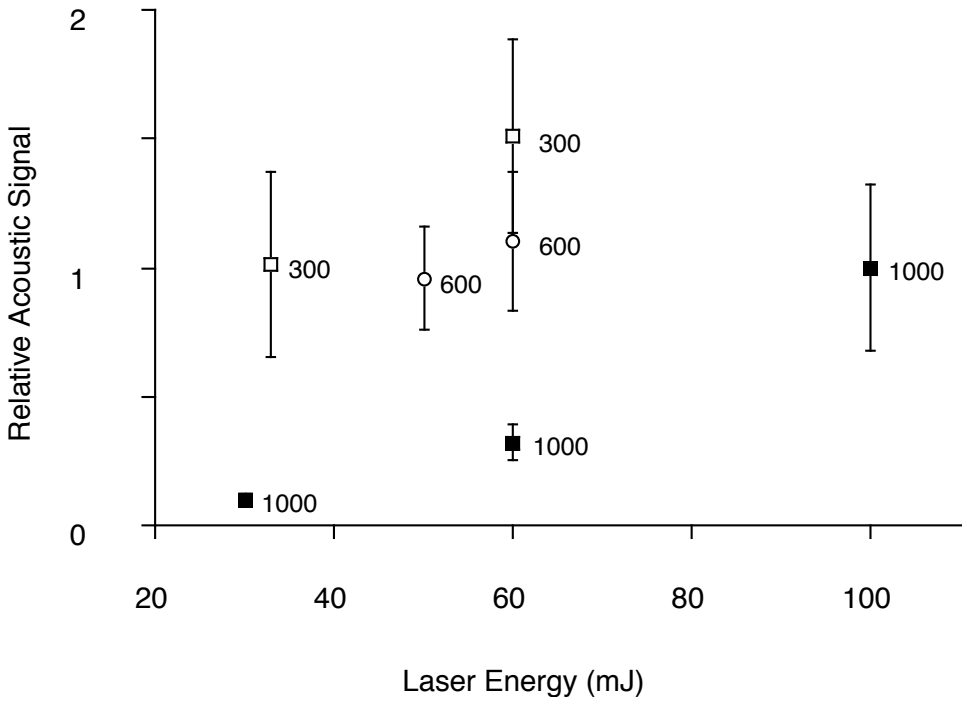

Figure 4.8: The effect of laser energy on the acoustic transients normalized to the value at 100 mJ via a 1000 μm core diameter fiber. The relative signal plotted versus laser energy. The absorption coefficient was 300 cm^{-1}. Single pulses of 60–100 mJ laser energy were delivered through optical fibers with 300, 600, and 1000 μm diameter respectively. The numbers present fiber core diameter. All data are mean$\pm$standard deviation of 5 measurements.

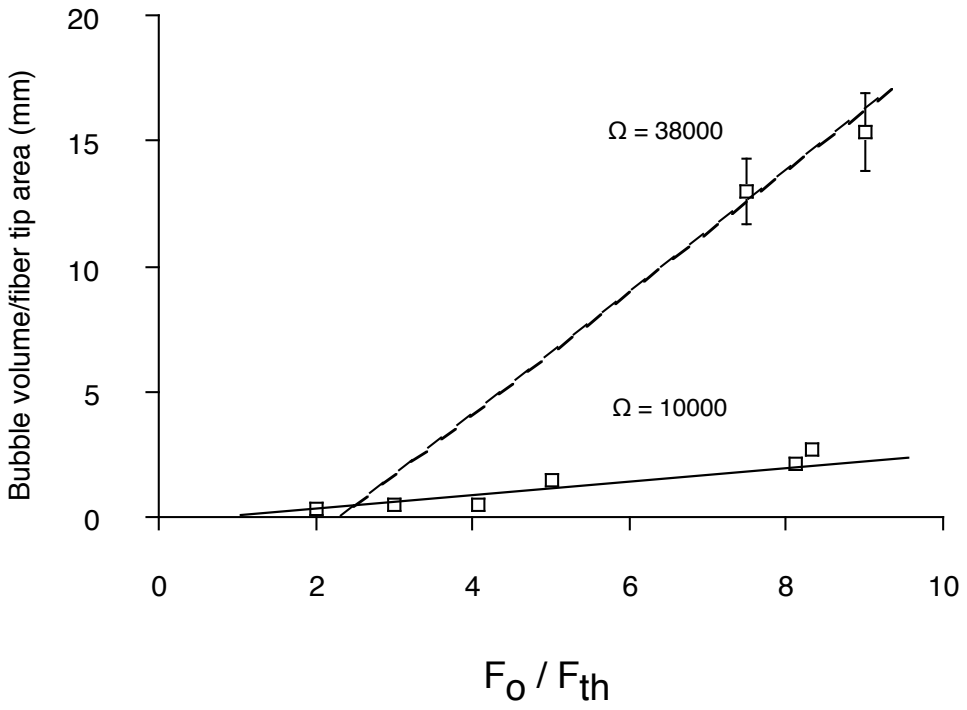

Figure 4.9: Ratio of maximal bubble volume to fiber surface area as a function of the ratio of incident radiant exposure and measured threshold for bubble formation in medicated oil solutions. Single pulses of 9–60 mJ were delivered into oil solutions (50–300 cm^{-1}) via fibers (300–1000 μm). The ratio of input radiant exposure and the measured threshold (F_o/F_{th}) was about 10.

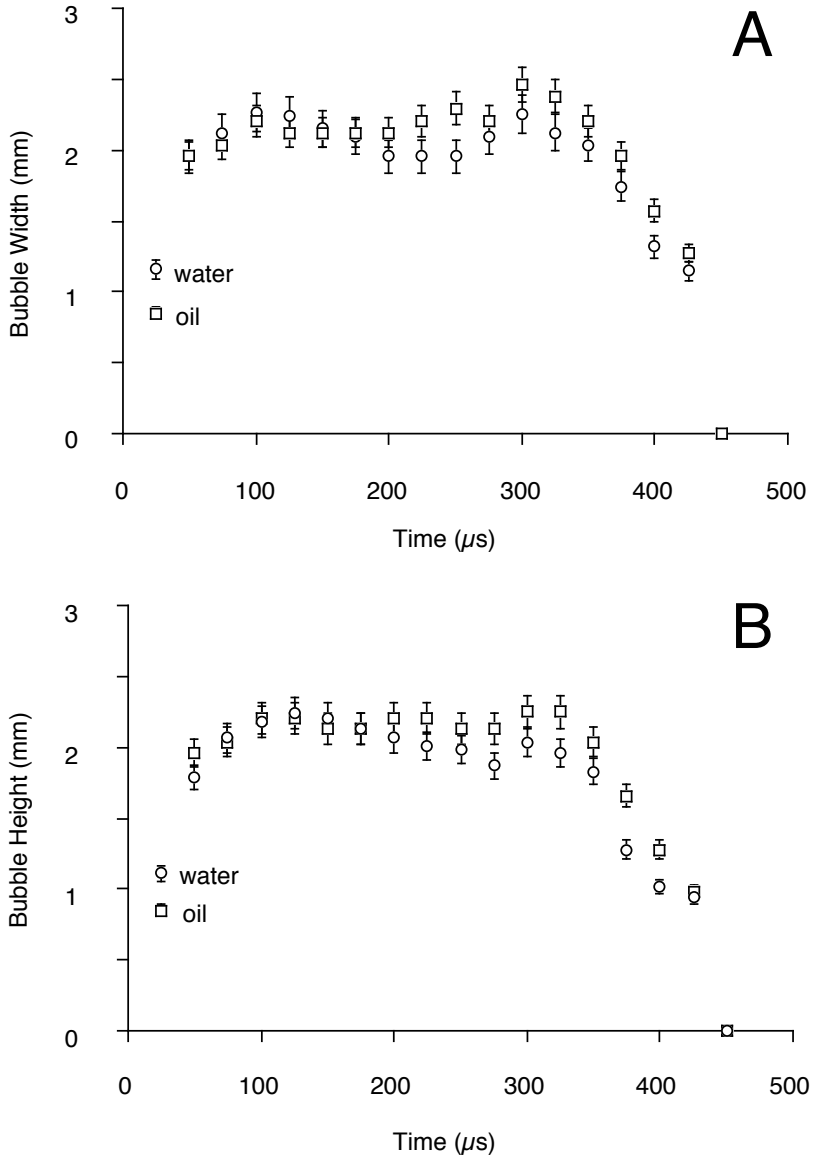

Figure 4.10: Measured bubble width and height as function of time. Single pulses of 50 mJ were delivered onto the absorbing gelatin surface ($100\,\mathrm{cm}^{-1}$) through clear water and oil via a 300 μm fiber. Error bars represent the standard deviation of three measurements.

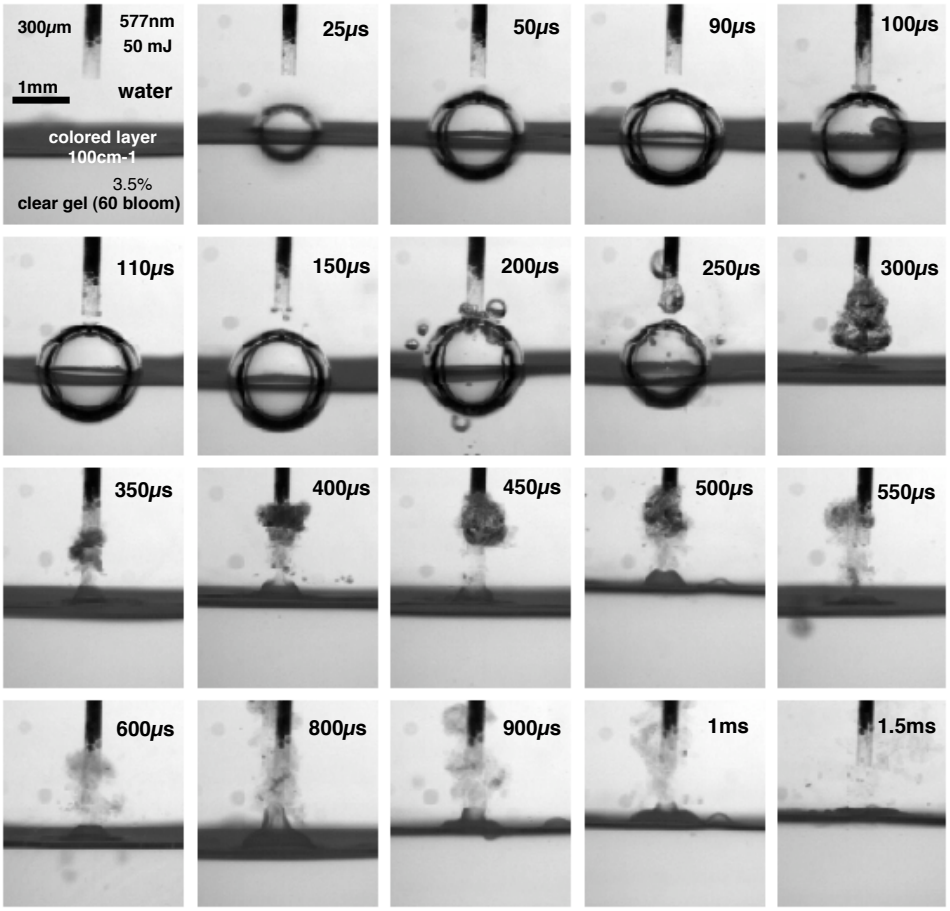

Figure 4.11: Flash photographs in side view of bubble growth and collapse on absorbing gelatin surface after the laser pulse. Single pulses of 50 mJ were delivered onto absorbing gelatin surface (3.5% 60 bloom, 100 cm^{-1}) through clear water via a 300 μm fiber. The fiber tip was placed 1 mm above the gelatin surface.

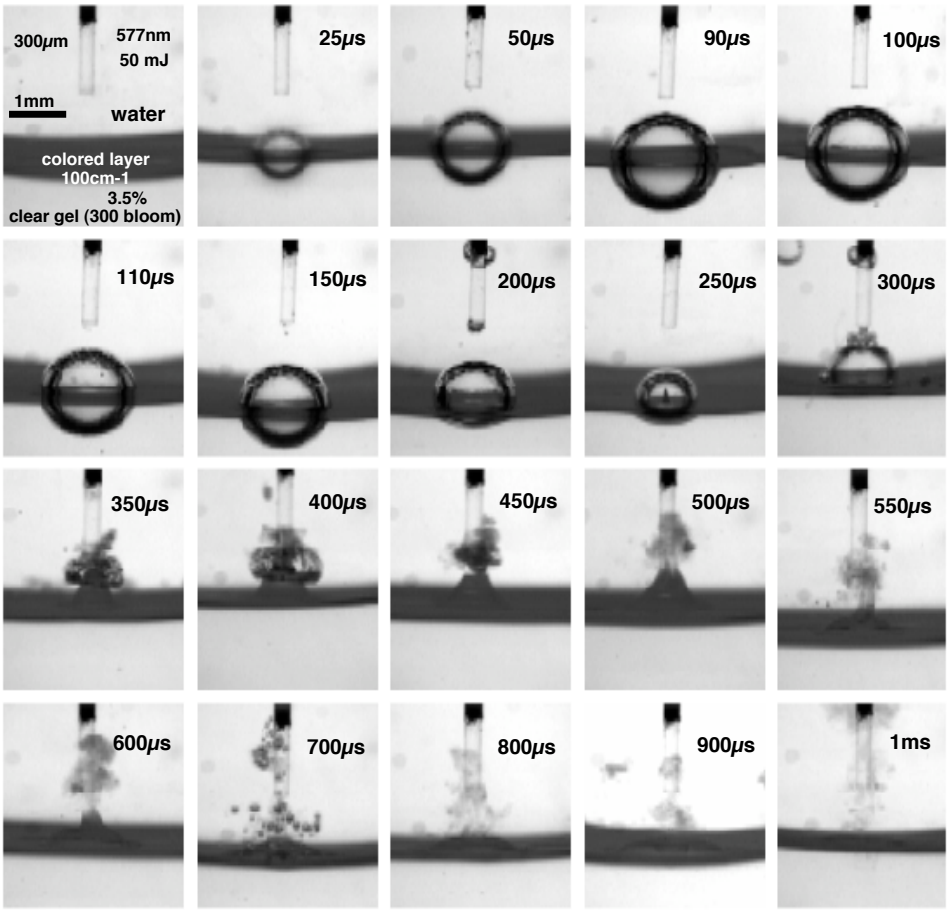

Figure 4.12: Flash photographs in side view of bubble growth and collapse on absorbing gelatin surface after the laser pulse. Single pulses of 50 mJ were delivered onto absorbing gelatin surface (3.5% 300 bloom, 100 cm^{-1}) through clear water via a 300 μm fiber. The fiber tip was placed 1 mm above the gelatin surface.

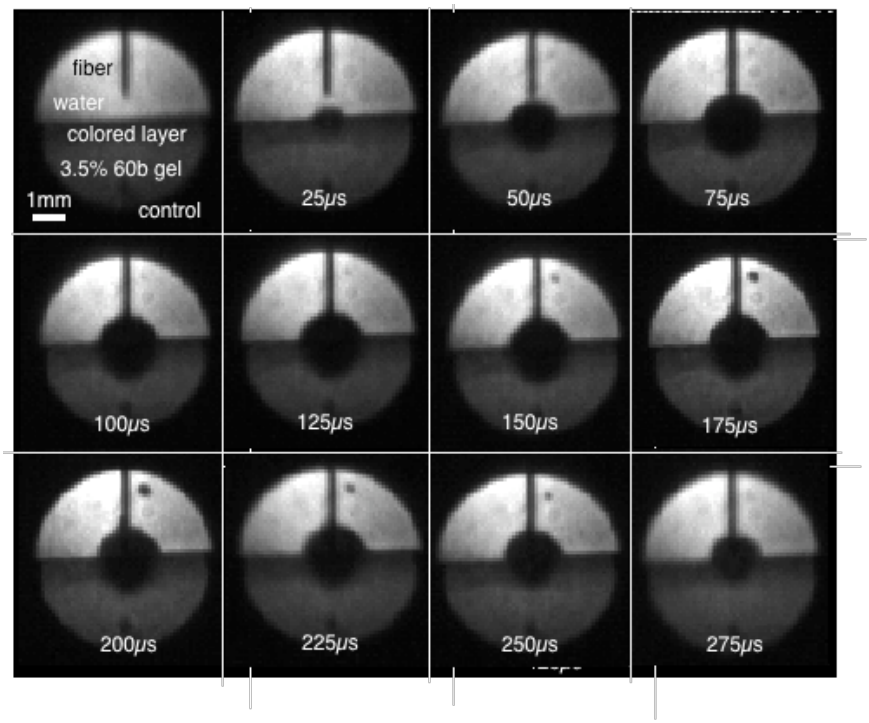

Figure 4.13: Side view of high-speed shadowgraphs of bubble formation on the absorbing gelatin surface (3.5% 60 bloom, $100\,\mathrm{cm}^{-1}$). The laser parameters were the same as those used in Figure 4.11.

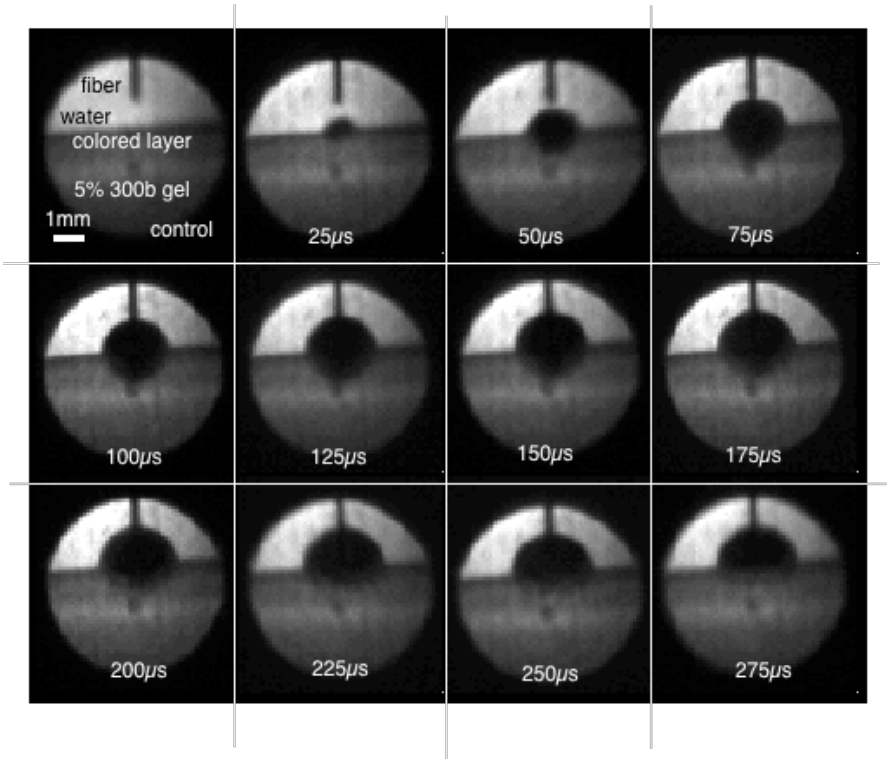

Figure 4.14: Side view of high-speed shadowgraphs of bubble formation on the absorbing gelatin surface (5% 300 bloom, $100\,\mathrm{cm}^{-1}$). The laser parameters were the same as those used in Figure 4.12.

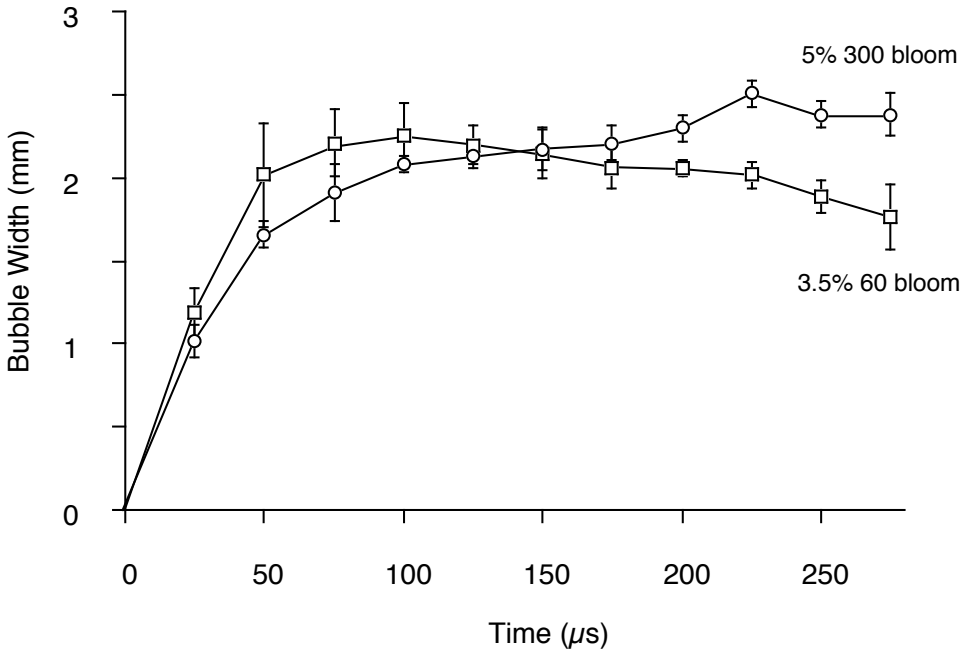

Figure 4.15: The bubble width as function of time after the laser pulse for 3.5% 60 bloom gelatin and 5% 300 bloom gelatin. Error bars represent the standard deviation of three measurements.

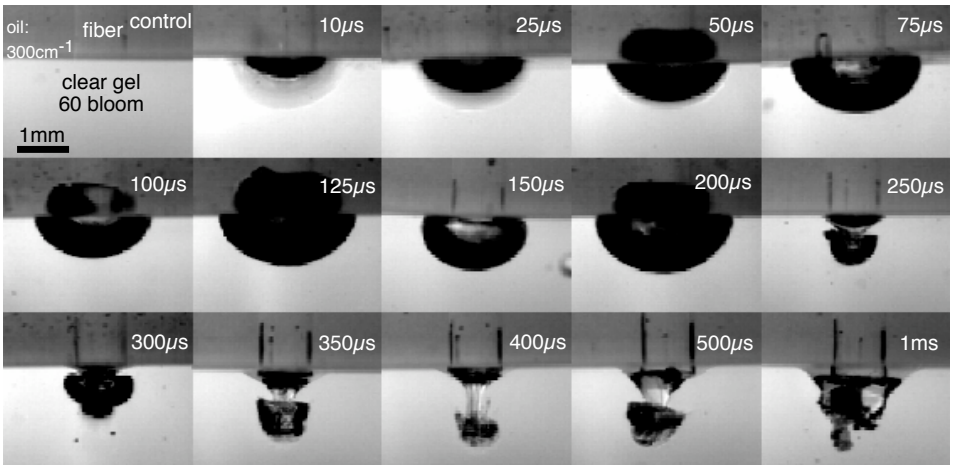

Figure 4.16: Flash photographs in side view of bubble growth and collapse on absorbing gelatin surface after the laser pulse. Single pulses of 50 mJ were delivered onto the surface of clear gelatin (3.5% 60 bloom) covered with a 300 cm^{-1} oil solution via a 1000 μm fiber. The fiber tip was slightly in contact with the gelatin surface.

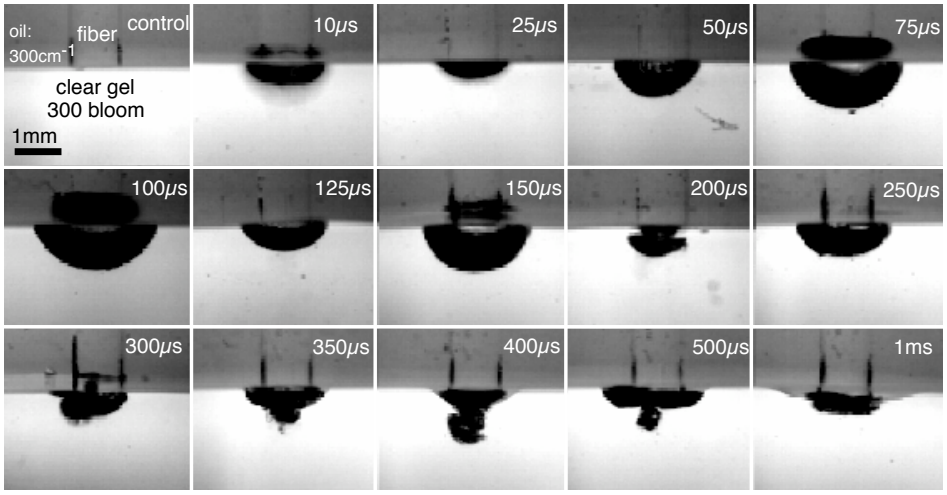

Figure 4.17: Flash photographs in side view of bubble growth and collapse on absorbing gelatin surface after the laser pulse. Single pulses of 50 mJ were delivered onto the surface of clear gelatin (3.5% 300 bloom) covered with a 300 cm^{-1} oil solution via a 1000 μm fiber. The fiber tip was slightly in contact with the gelatin surface.

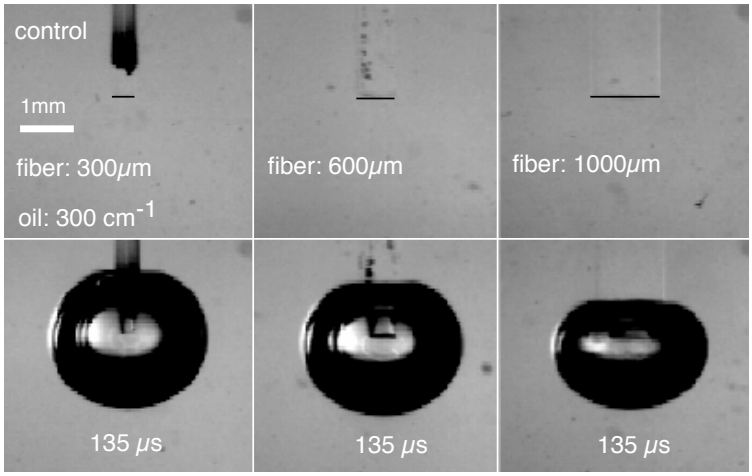

Figure 4.18: Side view of bubbles of the same width generated by 300, 600, and 1000 μm fibers respectively. Single pulses of 33 mJ, 50 mJ, and 100 mJ were delivered into a 300 cm^{-1} oil solution. The bubbles were formed right at the fiber tips.

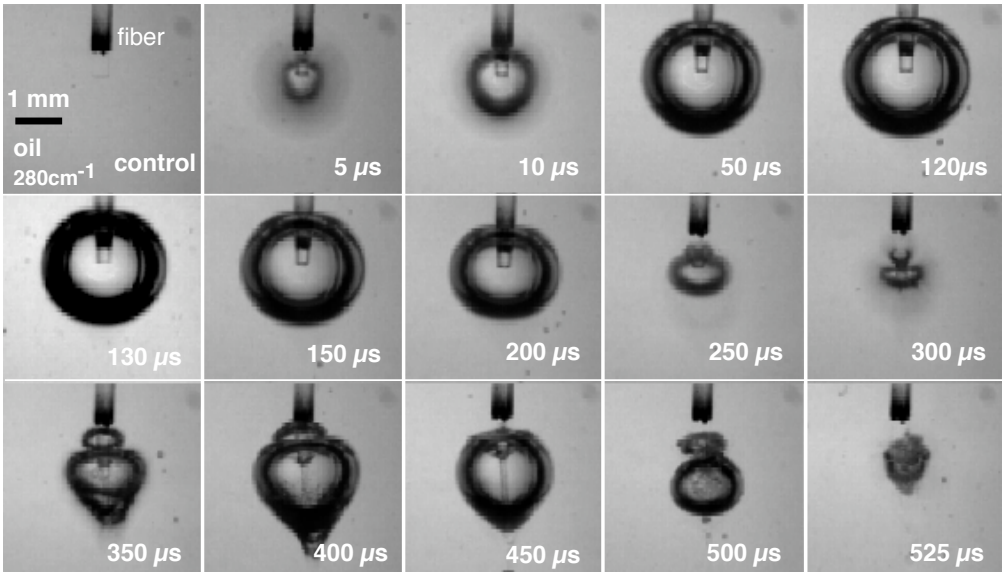

Figure 4.19: Flash photographs in side view of bubble formation in the absorbing oil solution. Single pulses of 33 mJ were delivered into a 280 cm^{-1} oil solution via a 300 μm-fiber.

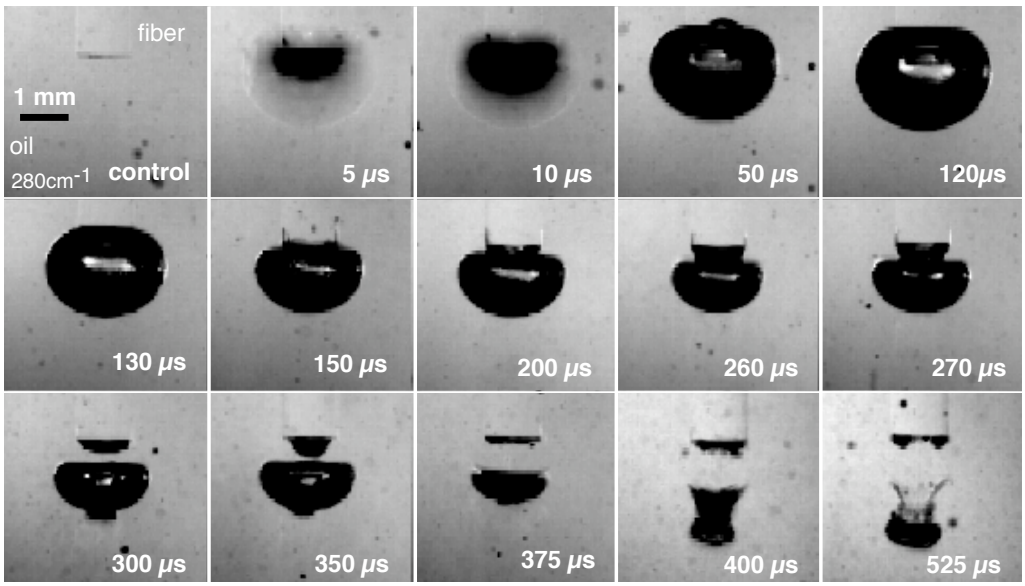

Figure 4.20: Flash photographs in side view of bubble formation in the absorbing oil solution. Single pulses of 100 mJ were delivered into a 280 cm^{-1} oil solution via a 1000 μm-fiber.

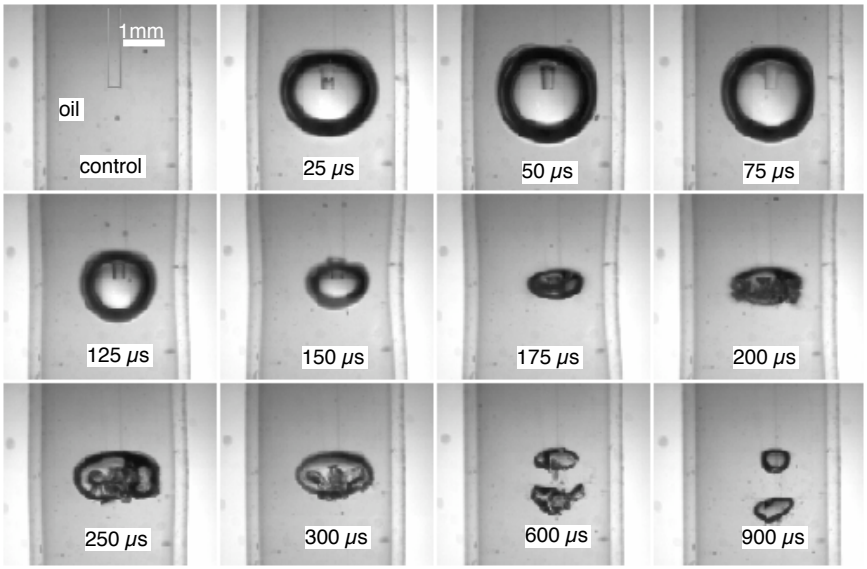

Figure 4.21: Side view of bubble formation in a 300 cm^{-1} oil solution confined in a 3 mm silicone tube. The laser parameters were the same as those used in Figure 4.19.

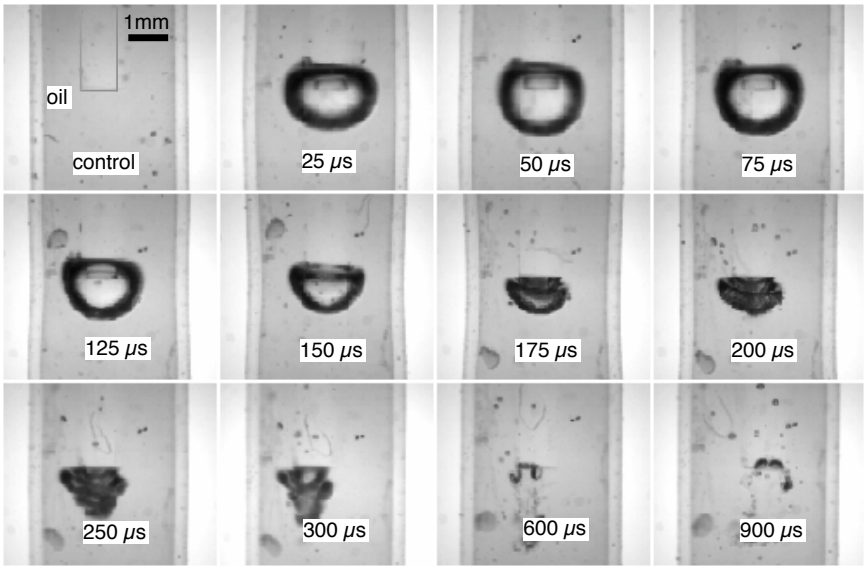

Figure 4.22: Side view of bubble formation in a 300 cm^{-1} oil solution confined in a 3 mm silicone tube. The laser parameters were the same as those used in Figure 4.20.

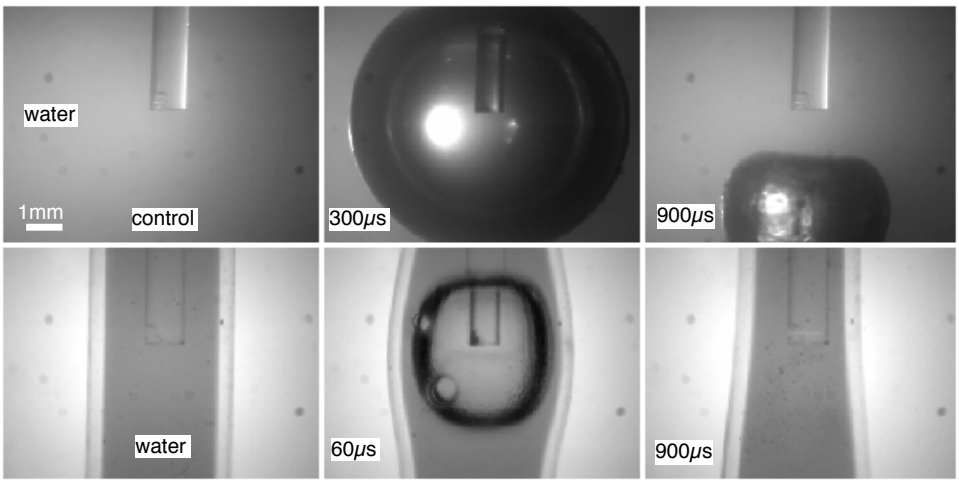

Figure 4.23: Side view of bubble formation in a semi-infinite space (top panel) and in a 3 mm tube (bottom panel). Single pulses of 100 mJ was delivered into a 300 cm^{-1} water solution via a 1000 μm fiber. The maximal bubble diameter and dilation of the tube wall were observed at 300 μs and 60 μs respectively after the laser pulse. The invagination of the tube was 84% of the initial value about 900 μs after the laser pulse.

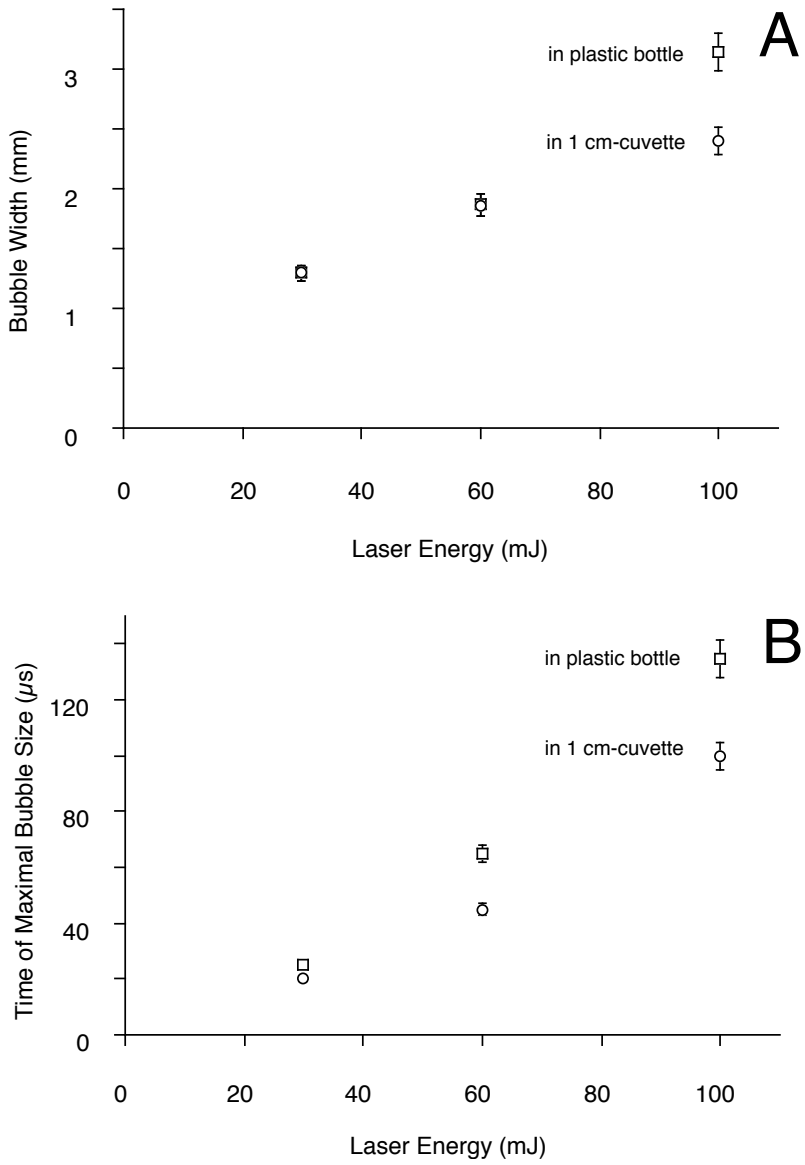

Figure 4.24: Maximal bubble width (A) and the corresponding time (B) as a function of laser energy. The error bars represent the standard deviation of three measurements. Some error bars are smaller than the symbols.

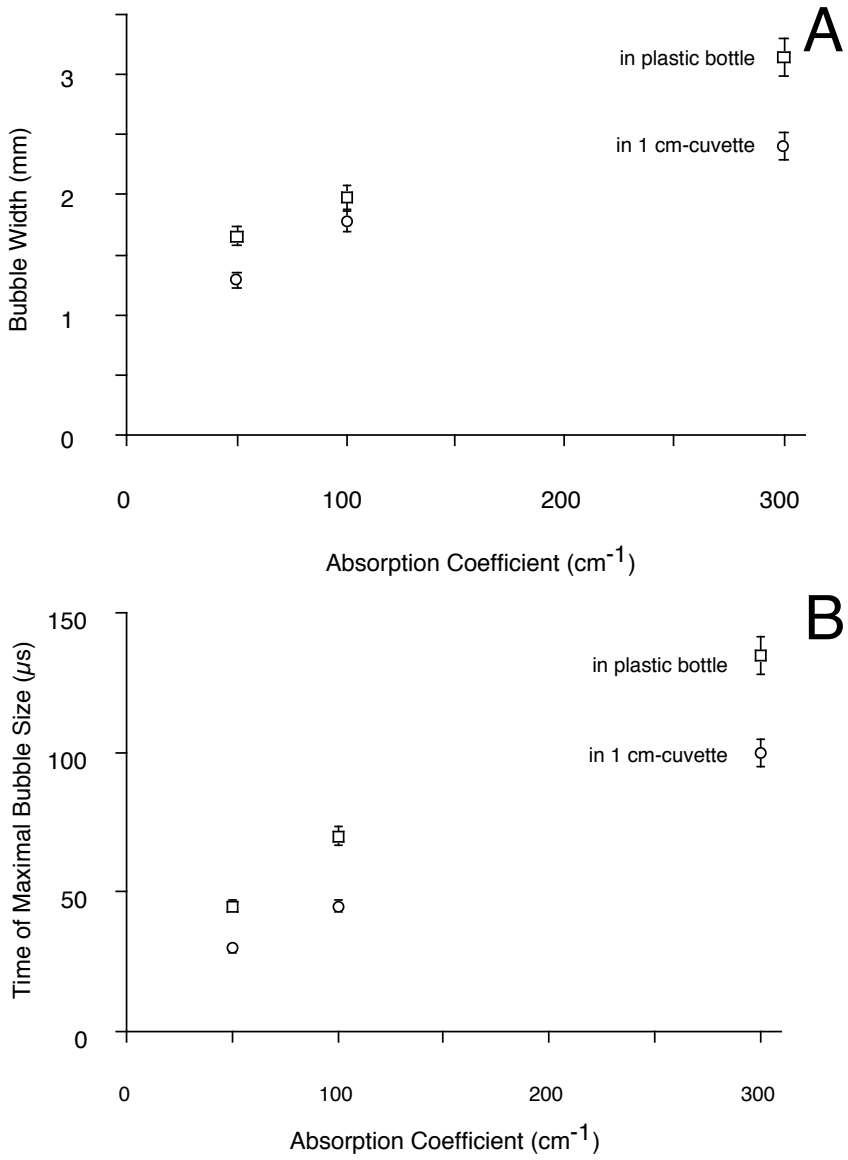

Figure 4.25: Maximal bubble width (A) and the corresponding time (B) as a function of absorption coefficient. The error bars represent the standard deviation of three measurements. Some error bars are smaller than the symbols.

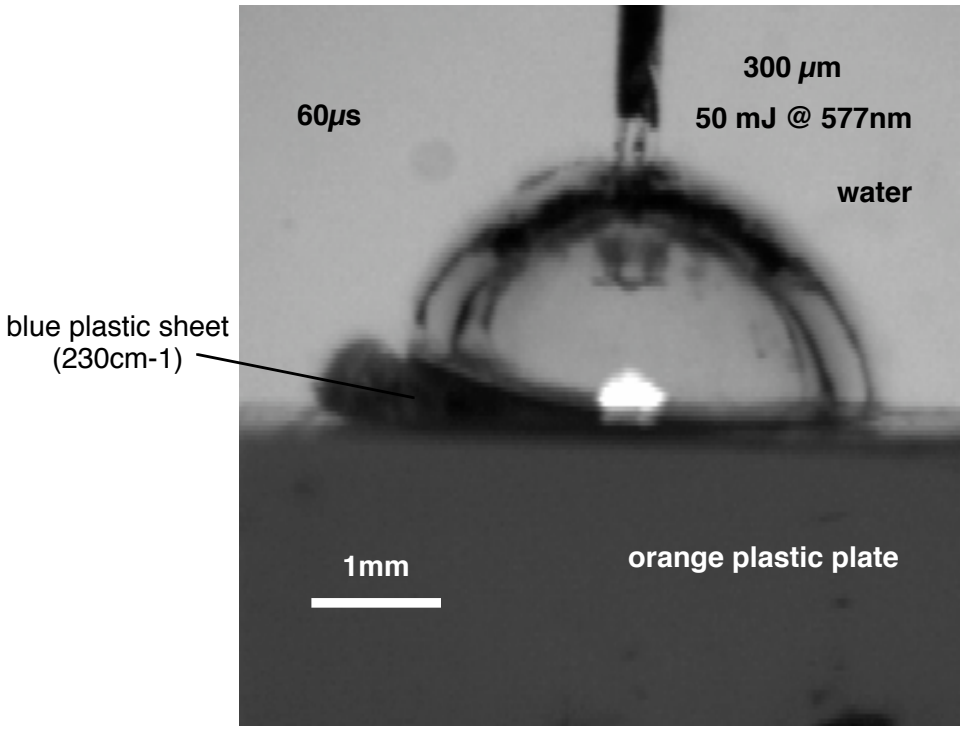

Figure 4.26: Side view of a bubble formed on a plastic plate.

Liquid	Density mg/mm^3	Viscosity cP	Bubble Width in Liquid mm	Bubble Width on Gelatin mm
Water	0.992	0.653	3.9	5.5±0.2
Mineral oil	0.86	29.67	2.2	5.4±0.2
Contrast Medium	1.411	13.34	—	5.2±0.3

Table 4.1: Variation in maximum bubble size when formed *in* 300 cm^{-1} liquids or under clear liquids *on* 300 cm^{-1} gelatin. The bubbles formed in liquids were confined by a 3 mm tube, and consequently are smaller than bubbles formed in 1 cm cuvettes because of the presence of tube boundaries. The errors are the standard deviation of three measurements.

Chapter 5

Particle Image Velocimetry

5.1 Introduction

In this chapter, experiments are described to investigate the flow pattern around laser-induced cavitation bubbles near a soft boundary. The bubbles were formed either at a fiber tip or on a target depending on where the laser energy was absorbed. The interest in the flow pattern and the speed of the flow motion during the expansion and collapse of the bubbles arises from their importance in photomechanical drug delivery.

A number of optical techniques have been used to extract quantitative information about the velocity components in a flow field [113]. For example, interferometry, schlieren and shadowgraph have contributed tremendously to the understanding of fluid motion. The serious limitation with these techniques is that of involving path integration and hence they cannot be used to characterize complex or unsteady flow fields except in limited circumstances. Conventional flash photography and high speed photography have been widely used for the

dynamics of laser-induced cavitation or cavitation bubbles [3, 76, 89, 98, 114–116]. Unfortunately, a major limitation associated with these techniques is that it is impossible to track the temporal evolution of a fluid flow surrounding the bubble. To overcome this limitation, Vogel *et al.* demonstrated that the combination of particle image velocimetry (PIV) and high speed photography could be used to investigate the cavitation bubble dynamics near a solid boundary [117].

The particle image velocimetry has emerged over the past decade. It involves extracting velocity information by measuring the displacement of these particle images over a known period of time, which depends on the interaction between radiation and particles to record the location of each particle. There are two mechanisms involved in PIV: scattering and diffraction. Assuming the particle does not absorb light, all of the light that falls within the cross-sections of the particle is scattered. An additional amount of light is scattered by diffraction around the edge of the particle. The basic assumption for PIV is that the motion of the particles accurately represents the fluid motion.

In this study, the images of the particle trajectories were recorded using a CCD camera. The use of a CCD camera makes nearly real-time displays of stored information possible, which is helpful for monitoring the quality of images as experimental conditions change. The aims of this study were to measure the velocities near laser-induced cavitation bubbles and to investigate the hydrodynamic flow pattern during the bubble formation for the improvement of localized drug delivery.

5.2 Materials and Methods

5.2.1 Laser Radiation

The experimental arrangement is outlined in Figure 5.1. A flashlamp-pumped dye laser (Palomar Medical Technologies) operating at 577 nm was used to create cavitation bubbles. The pulse duration was 1.3 μs (full width at half maximum). The laser pulses were delivered via a 1000 μm fiber. The laser energy was 60 mJ for the laser absorption on a target and 30 mJ for the laser absorption at the fiber tip (Figure 5.2). The light source for PIV was an argon-ion laser (Model 171, Spectra-Physics). Laser output was in the 2–8 W range before passing through an acousto-optic modulator (AOM-403c, Intra Action).

5.2.2 Cavitation Bubble Generation

The cavitation bubbles were formed either on gelatin (Figure 5.2(a)) or at the fiber tip (Figure 5.2(b)). Laser absorption on gelatin was achieved by adding a light absorbing dye. Absorption at the fiber tip was achieved by painting a thin light absorbing layer (<200 μm) on the end face of the fiber tip. This made it possible to simulate the bubble formation typically found in light absorbing liquids and simultaneously allow visualization through the water. The fiber was located 1 mm above the gelatin target. The gelatin samples were covered with distilled water seeded with scatterers.

5.2.3 Thrombus Model

The thrombus was modeled using 10% gelatin (300 bloom). The percentage was determined by the weight ratio of gelatin to water. Samples were clear or blue color made by adding a dye (direct blue 15, Sigma). The gelatin-water mixture was heated to 60℃ with stirring until it became clear, and then sufficient dye was added to achieve the desired absorption coefficient. For example, samples with $300\,\mathrm{cm}^{-1}$ could be made by adding 40 mL of distilled water, 4 g of the gelatin, and 0.231 g of the dye. Liquid gelatin samples were poured into 1 cm cuvettes and molded to form 2–3 cm thick thrombus models with planar geometry.

5.2.4 Scattering Particles

The fluid was seeded with polymer microspheres (Duke Scientific) with an average diameter of 25 μm. These particles had nearly the same density as water ($1.05\,\mathrm{g/cm}^{3}$). Therefore, the particles would follow the flow arising from the expansion and collapse of cavitation bubbles. These particles were clear and did not absorb the laser energy, but could be visualized by the light that they scattered. The concentration of scatterers was about 3×10^{4} scatterers/mL. It was difficult to ensure good spatial resolution in the analysis of the fluid velocity field if the concentration was greater than this value.

5.2.5 Particle Image Velocimetry

The laser beam from the argon laser was chopped by the acousto-optic modulator to generate a first-order diffracted beam. The modulator was driven by

a combination of a pulse generator (Model 8011A, Hewlett-Packard) and a delay generator (Model DG535, Stanford Research Systems). Thus, pulse trains of variable length, pulse separation, and pulse number could be obtained. By selecting the separation time, I refer to this as the time coding, I produced an image of the particle trajectory as series of dots and dashes. From this coded image, the velocities of particles near the cavitation bubbles could be determined. The modulated laser beam was focused horizontally by a bi-convex lens with a focal length of 38.1 mm and expanded vertically by a cylindrical lens with 40 mm focal length. A light sheet of 10 mm height and 200 μm thickness was produced that passed through the center of the cavitation bubble. The particle track images were captured with a CCD camera (XC-57, Sony) through a microscope (SZ6045, Olympus). The camera was oriented perpendicular to the light sheet. The direction of particle trains was determined by setting different intervals between the last pulse and previous sequential pulses (see Figure 5.3).

5.2.6 Flash Photography

Conventional single event flash photography was used to orient each PIV image. Each picture was a single event and reproducible. A strobe (MVS–2601, EG&G) was used for illumination at an adjustable delay time controlled by the digital delay generator. The generator was triggered by the laser pulse using a photodiode (UDT Instruments) that was attached to the laser delivery fiber. The delay time was defined as the period between the end of the laser pulse and the peak of the flash of light from the strobe. The fluid was not seeded for flash

photography.

5.3 Results

I investigated the cavitation bubble dynamics during the bubble expansion, collapse, and several milliseconds after the collapse using PIV. Two sets of experiments were performed based on where the bubbles formed due to the laser absorption on the gelatin target and at the fiber tip.

Figures 5.4–5.6 show the PIV/flash photography for the laser absorption on gelatin. Figure 5.4 shows a typical multiple exposure photograph of the flow around a cavitation bubble and the corresponding flash photographs. The flow around the bubble was moving away from the gelatin surface along with the bubble expansion. The measurements indicated that the velocity of particles near the bubble slowed down significantly when the bubble reached its maximum. The dynamic range was about 5–12 m/s. Figure 5.5 shows the evolution of the flow near a cavitation bubble during the bubble collapse phase. The maximum velocity during this phase was comparable to that during the bubble expansion. The flow moved away from the gelatin target. Figure 5.6 shows the flow patterns after a comparatively longer time (several milliseconds) after a laser pulse. The particles moved slowly at an average speed of 0.1 m/s. The presence of several vortices around the fiber tip were observed.

Figures 5.7–5.9 show the PIV/flash photography for the laser absorption at the fiber tip. Figure 5.7 shows a typical multiple exposure photograph of the flow around a cavitation bubble and the corresponding flash photographs. Unlike the

previous case (laser absorption on target), the flow around the bubble was moving towards the gelatin surface along with the bubble expansion. The measurements indicated that the velocity of particles near the bubble slowed down when the bubble reached its maximum. The dynamic range was about 9–12 m/s. The flow also slowed down to 7 m/s near the boundary (dashed line). Figure 5.8 shows the evolution of the flow near a cavitation bubble during the bubble collapse phase. The measurements indicated that the velocity of particles near the bubble slowed down to 5 m/s near the boundary (dashed line). The maximum velocity during this phase was comparable to that during the bubble expansion. The flow moved towards the gelatin target. Figure 5.9 shows the flow patterns after a comparatively longer time (several milliseconds) after a laser pulse. The particles moved slowly at an average speed of 0.2 m/s. The particles moved away from the gelatin surface rather than towards the gelatin surface. The presence of several vortices around the fiber tip was observed.

5.4 Discussion

This study demonstrated that PIV photography is a useful method for the investigation of the photomechanical drug delivery process. One can obtain more information about the flow behavior near the cavitation bubble and the target by PIV photography than by conventional flash photography, especially when the bubble reaches its maximum size and interacts with the target. For example, it is impossible to measure the velocity of flow as it interacts with the target from a conventional flash photograph (c.f., Figure 5.8). However, it is easy to determine

the velocity with PIV photography.

The measurements showed that the particle velocities slowed down as the cavitation bubble reached its maximum size. The velocities of particles also slowed when the flow interacted with a target because of the resistance from the target. The momentum of particles decreased to about 16% of their initial value. The difference in the velocities may provide the crucial information related to photomechanical drug delivery. The question of how fast the particles must move towards the target to penetrate into the gel remains and requires further investigation.

Velocities of particles were within a range of 5–12 m/s during expansion and collapse. A study by Vogel *et al.* demonstrated that velocities of particles around laser-induced cavitation bubbles ranged between 2–30 m/s during their collapse near a solid boundary [117]. The cavitation bubbles were generated by focusing pulses of 100–400 mJ from a passively Q-switched ruby laser into a cuvette with distilled water. However, in the present study the first PIV image was taken about 10 μs after the laser pulse. The particle velocity might be greater than 100 m/s at that time assuming the particles were initially located on the fiber surface or the gel surface since the flash photographs showed that the bubble wall was about 0.4–0.6 mm away from the fiber surface or the gel surface about 10 μs after the laser pulse. This observation may imply that the loss of flow momentum was caused by the pressure from the surrounding liquid, and the transient displacement of the vapor cavity initiated the flow motion. Unfortunately, the particle velocity at this early stage could not be determined in the present study due to limitations

of the photographic setup.

The problem of directional ambiguity was resolved by using multiple exposures with variable pulse separation. This technique permits the unambiguous, instantaneous, two-dimensional measurement of velocity near the laser-induced cavitation bubbles in a single frame.

PIV photography showed clearly that the major direction of hydrodynamic flow changed during the bubble expansion and collapse (i.e., towards the target), and at a certain time after the collapse (i.e., away from the target) as the bubble was formed at the fiber tip. However, it was not clear whether the majority of flow moved towards the target when the bubble was formed on the target although the flow surrounding the bubble moved along with the bubble during its contraction.

The flow patterns suggested that the drug could be delivered into clot or vessel wall radially no matter where the cavitation bubbles were formed since both laser absorption on the target and at the fiber tip could cause the flow to move radially. The drug could be delivered axially as the cavitation bubble formed at the fiber tip (i.e., in a light absorbing liquid). However, whether the drug could be delivered axially when the bubbles were formed on the target needs further investigation. This study showed that the laser energy used was significantly different for both laser absorption on the target and at the fiber tip although the maximum velocity was comparable each other. A possible explanation is due to the boundary effect of the fiber tip. The initial thermoelastic wave could only be released away from the fiber surface because of the rigid fiber. This finding suggests that less energy

is needed to generate similar velocity if the bubble is formed at the fiber tip, which may benefit some medical applications where less energy is required.

In conclusion, I demonstrated that PIV photography allows the visualization of the photomechanical drug delivery process. The flow pattern depends on where the cavitation bubbles are formed. The particle velocity near the cavitation bubbles range from 0.1–12 m/s. The maximum velocity of particles is comparable to the bubble expansion and collapse speed.

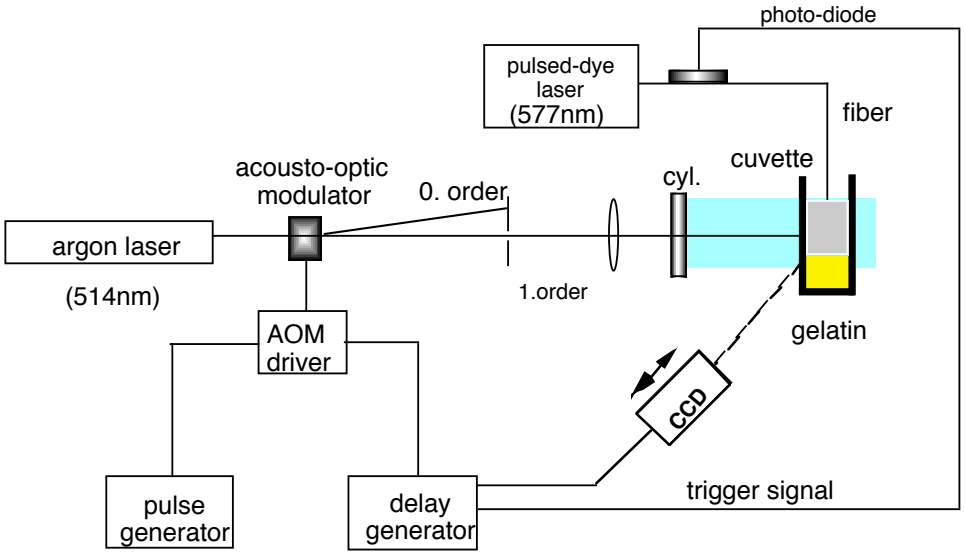

Figure 5.1: Experimental setup for time-resolved PIV of the flow around a laser-induced cavitation bubble.

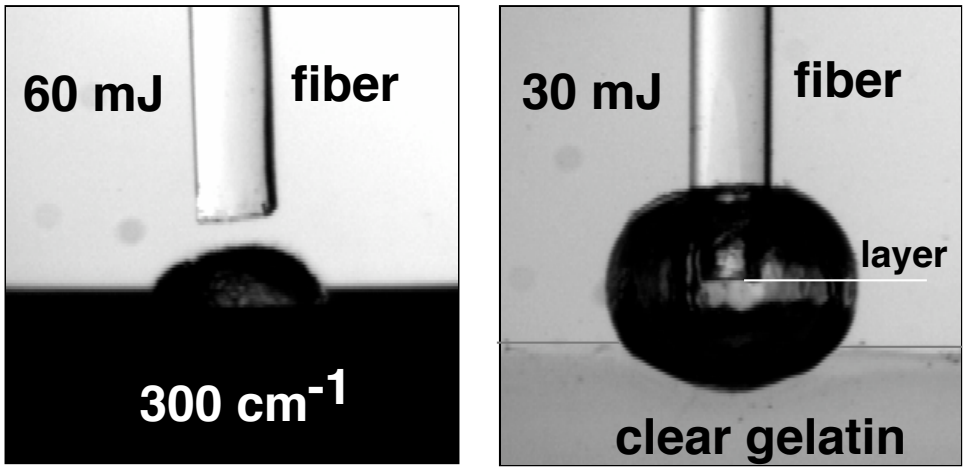

Figure 5.2: Schematic illustration of two configurations for cavitation bubble generation. (a) Laser absorption on gelatin. (b) Laser absorption at the fiber tip.

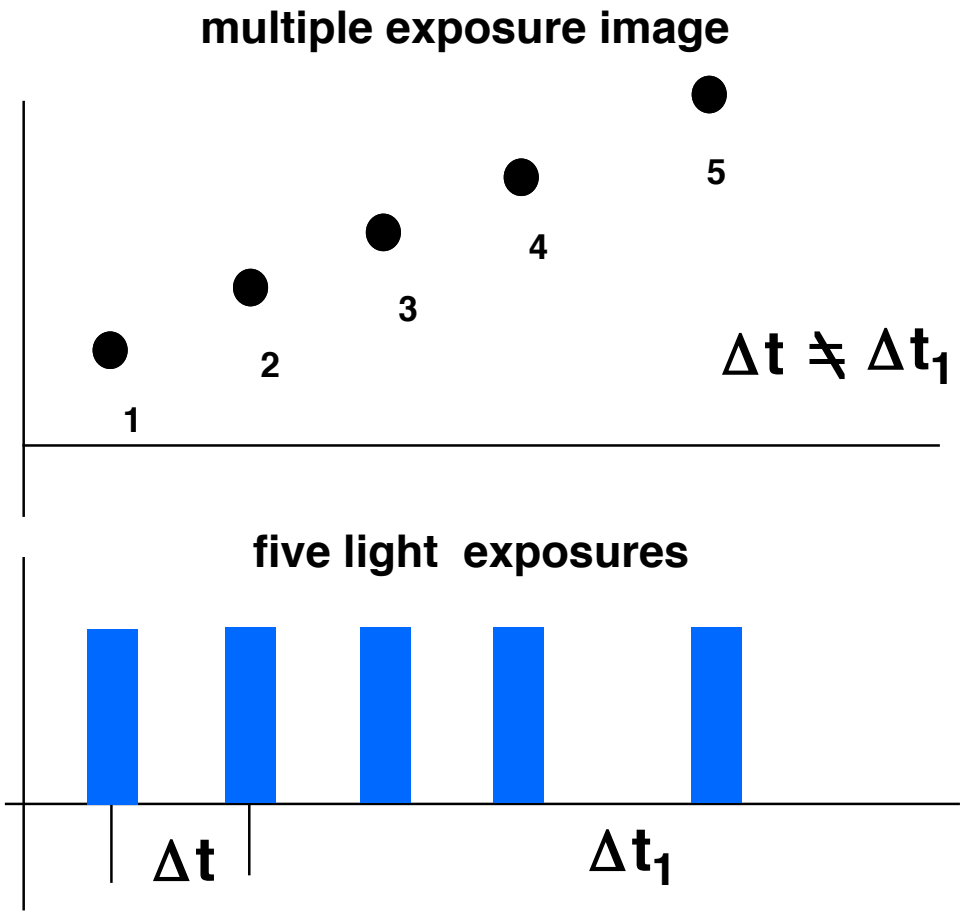

Figure 5.3: Technique for determining the direction of displacement between exposures on a single frame.

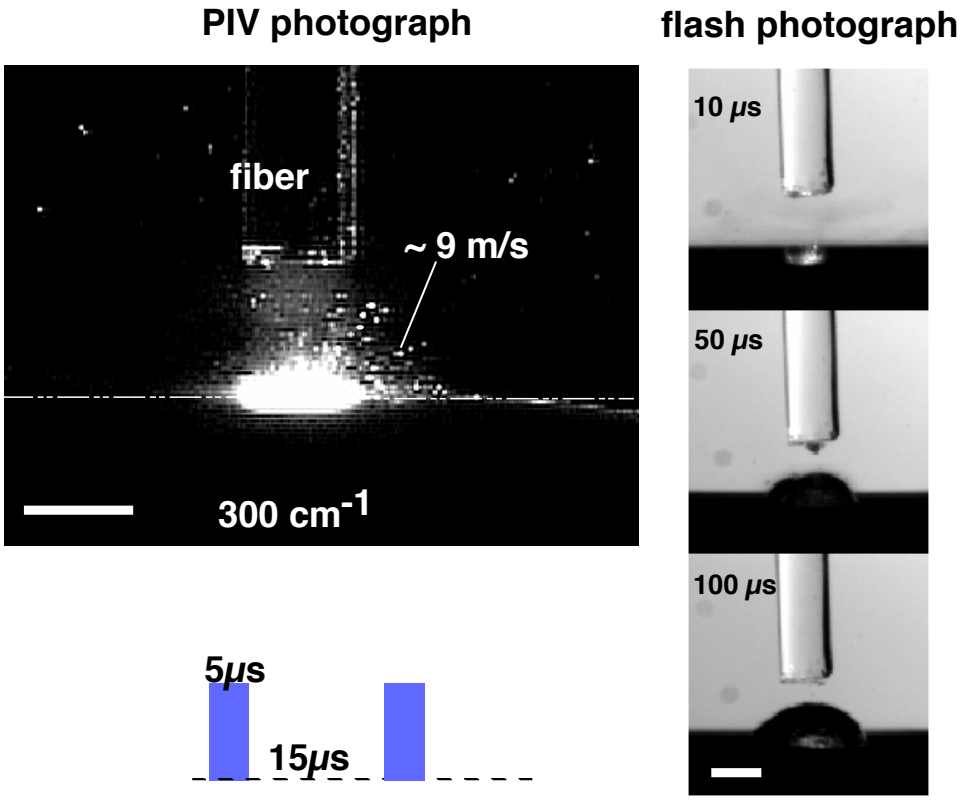

Figure 5.4: PIV/flash photograph of a cavitation bubble near a gelatin target 10–100 μs after a laser pulse. A 60 mJ laser pulse was delivered via an optical fiber with a 1000 μm core diameter. The maximum bubble diameter was 2.5 mm at 100 μs. The marked velocity was the average for this specific particle train during the bubble expansion. The white bar presents 1 mm in length. The white dashed line indicates the surface of the gelatin target. Five exposures were used with the presented pulse profile.

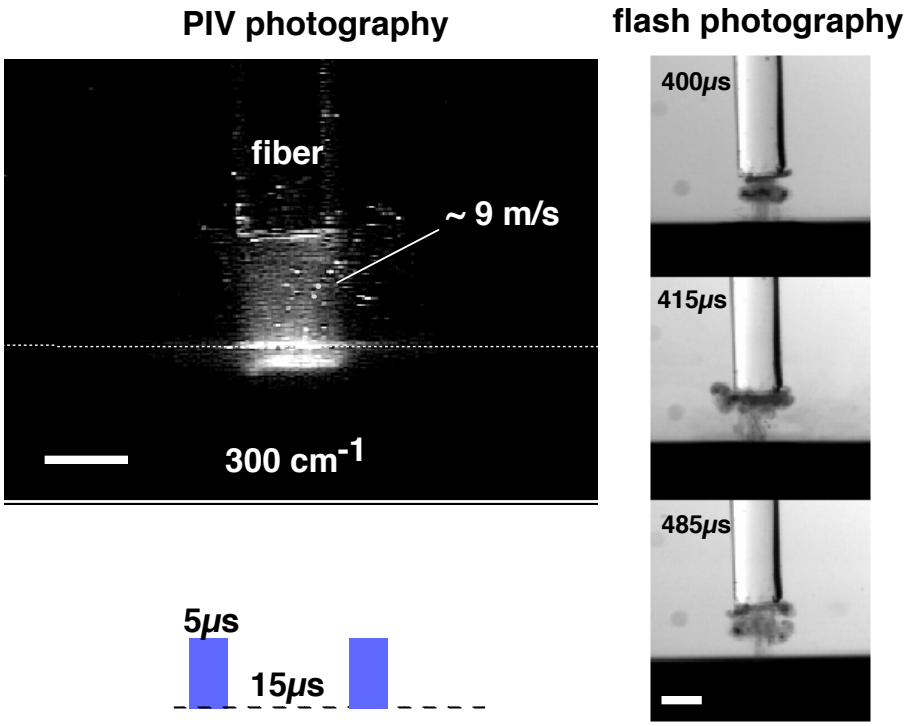

Figure 5.5: PIV/flash photograph of a cavitation bubble near a gelatin target 400–485 μs after a laser pulse. A 60 mJ laser pulse was delivered via an optical fiber with a 1000 μm core diameter. The marked velocity was the average for this specific particle train during the bubble collapse. The white bar presents 1 mm in length. The white dashed line indicates the surface of the gelatin target. Five exposures were used with the presented pulse profile.

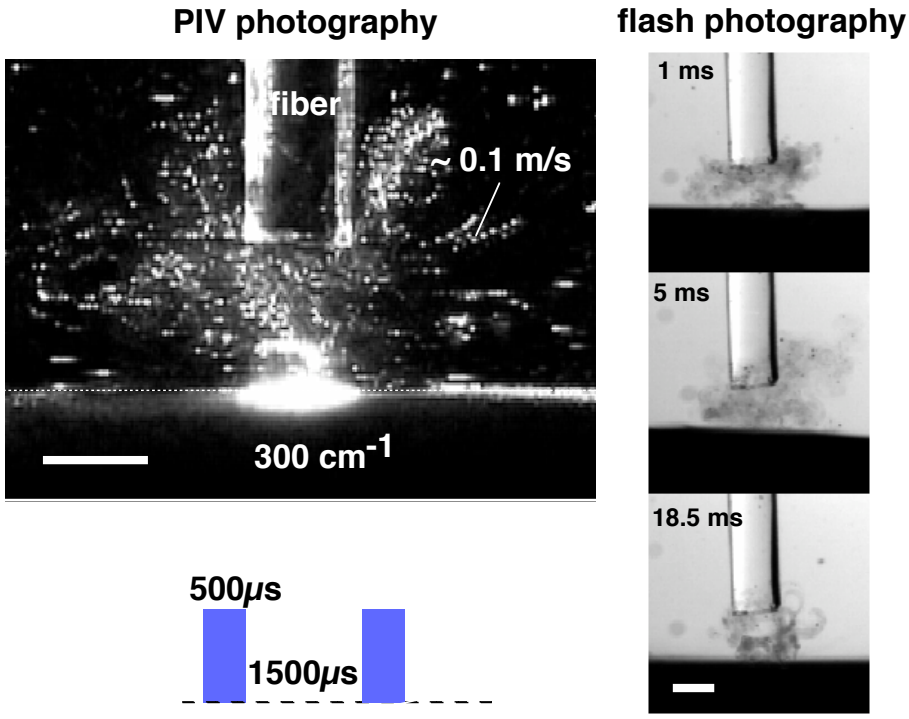

Figure 5.6: PIV/flash photograph of a cavitation bubble near a gelatin target 1–18.5 ms after a laser pulse. A 60 mJ laser pulse was delivered via an optical fiber with a 1000 μm core diameter. The marked velocity was the average for this specific particle train during post bubble collapse. The white bar presents 1 mm in length. The white dashed line indicates the surface of the gelatin target. Ten exposures were used with the presented pulse profile.

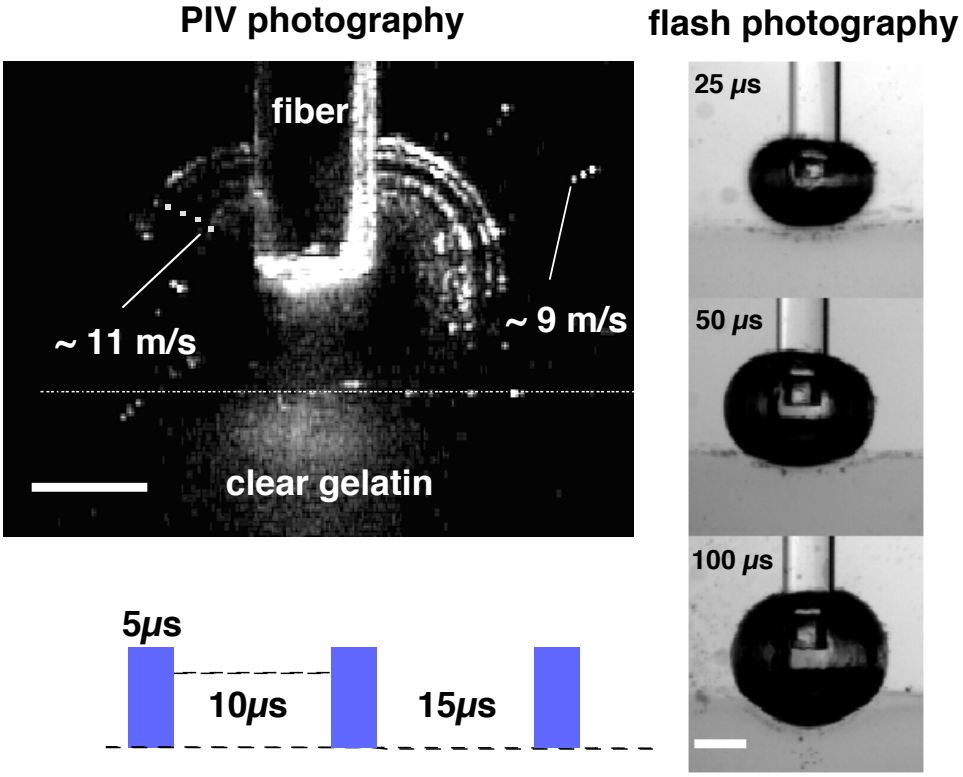

Figure 5.7: PIV/flash photograph of a cavitation bubble near a gelatin target 25–100 μs after a laser pulse. A 30 mJ laser pulse was delivered via an optical fiber with a 1000 μm core diameter. The maximum bubble diameter was 3.2 mm at 100 μs. The marked velocity was the average for this specific particle train during the bubble expansion. The white bar presents 1 mm in length. The white dashed line indicates the surface of the gelatin target. Five exposures were used with the presented pulse profile.

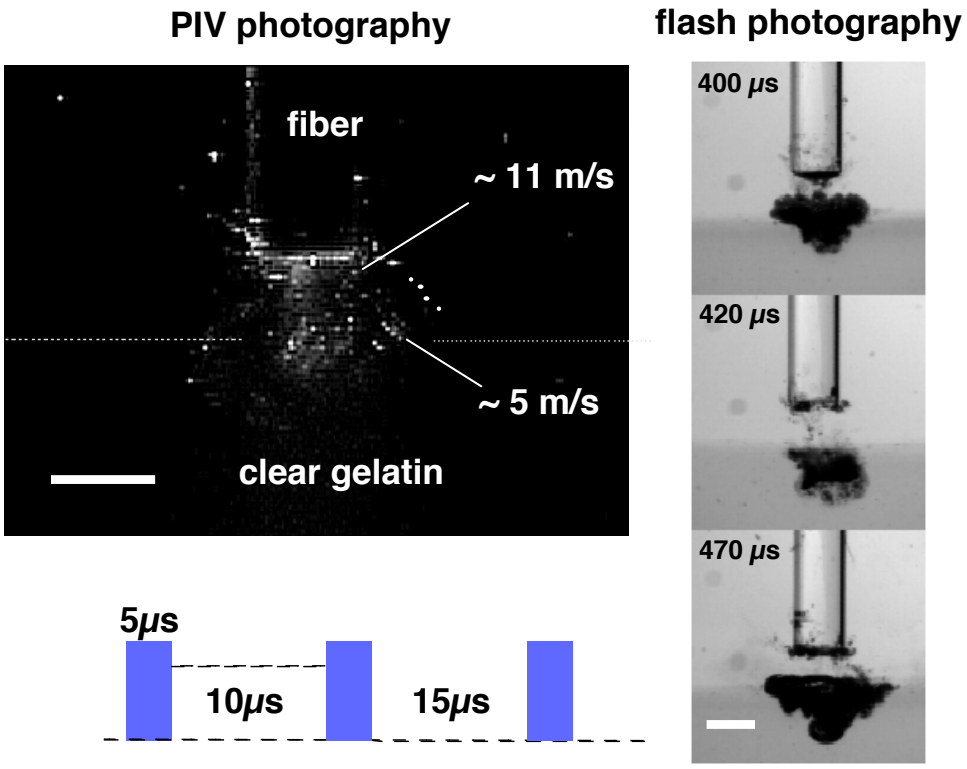

Figure 5.8: PIV/flash photograph of a cavitation bubble near a gelatin target 400–470 μs after a laser pulse. A 30 mJ laser pulse was delivered via an optical fiber with a 1000 μm core diameter. The marked velocity was the average for this specific particle trains during the bubble collapse. The white bar presents 1 mm in length. The white dashed line indicates the surface of the gelatin target. Five exposures were used with the presented pulse profile.

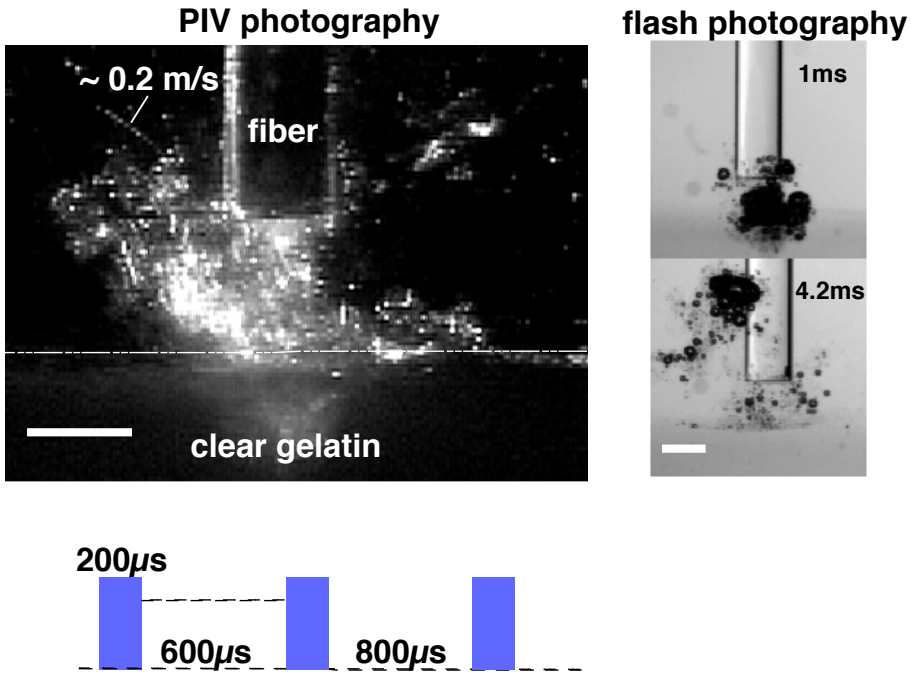

Figure 5.9: PIV/flash photograph of a cavitation bubble near a gelatin target 1–4.2 ms after a laser pulse. A 30 mJ laser pulse was delivered via an optical fiber with 1000 μm core diameter. The marked velocity was the average for this specific particle train during post bubble collapse. The white bar presents 1 mm in length. The white dashed line indicates the surface of the gelatin target. Five exposures were used with the presented pulse profile.

Chapter 6

Drug Delivery with Microsecond Laser Pulses into Gelatin and Porcine Aorta

6.1 Introduction

Pharmacological therapy for the treatment of restenosis, thrombosis, and ischemic heart diseases may eventually become clinically practical through the localized delivery of therapeutic agents [118–120]. A primary advantage of localized drug delivery over traditional drug delivery is that, with the former, side-effects such as bleeding or stroke can be avoided, because high concentrations of pharmacologic agents are delivered directly to the treatment site with minimal systemic exposure to the medication. Localized drug delivery for vascular applications is typically achieved using balloon-based catheter systems [63, 64, 67, 119, 121]. For example, a double-balloon catheter is used for delivering drug into vessel wall tissue by inflation of two balloons in an artery with a pressurized drug-filled

volume between them [119]. The primary problems associated with current investigational systems are their cumbersome size and long inflation times as well as the risk of medial injury occurring during the balloon inflation process, thus potentially limiting the benefits of localized drug delivery.

Photomechanical drug delivery is a technique for delivering drugs to localized areas [2, 3]. Unlike the techniques for enhancing local delivery of molecules that use laser-induced shock waves [77,122], photomechanical drug delivery uses a laser pulse to generate a cavitation bubble in a blood vessel owing to the absorption of laser energy by targets (e.g., blood clots) or surrounding liquids (e.g., blood). The cavitation bubble expands and collapses hundreds of microseconds after the laser pulse. The hydrodynamic pressure arising from the expansion and collapse of the cavitation bubble can force the drug into the clot or the vessel wall. One can perform photomechanical drug delivery by timing the laser pulses to be coincident with an injected bolus of drug. The delivery system for photomechanical drug delivery could consist of only two elements: an optical fiber or light guide for delivering laser pulses and catheter tubing for injecting drugs. A fluid-core laser catheter has been used to remove thrombus (blood clot) with a pulsed dye laser without damaging the vessel wall tissue [55]. Photomechanical drug delivery with such a fluid-core laser catheter may be an alternative method to current techniques for localized drug delivery.

Previous studies have established that cavitation bubbles can be formed in a liquid or on a solid target, depending on where the laser energy is absorbed. Cavitation bubbles play an important role in pulsed laser ablation of tissue and

in laser lithotripsy [76, 89, 98, 116]. van Leeuwen *et al.* demonstrated that cavitation bubbles make it possible to ablate tissue in a noncontact mode through a layer of blood or saline, and the forceful expansion of a cavitation bubble induces mechanical damage in adjacent tissue in the form of dissections [76]. A study by Vogel *et al.* suggested that cavitation-induced dilatation of vessel walls occurring in pulsed laser angioplasty can be prevented by division of the laser pulse energy into a prepulse with low energy and an ablation pulse with high energy [89]. Rink *et al.* reported that cavitation bubble collapse is the governing factor for fragmentation and disruption during laser lithotripsy with microsecond laser pulses [98]. The stone is progressively fragmented by stresses exceeding its tensile strength and by fatigue. In clinical trials of laser thrombolysis, Gregory suggested that the removal of thrombus might be attributed to the acoustic phenomena from vaporization and ejection of materials [1]. Francis *et al.* recently demonstrated that ultrasound could be used to accelerate the transport of fibrinolytic agents into clots as a result of the ultrasound effects mediated by cavitation and microstreaming [75]. However, whether the laser-induced hydrodynamic pressure can be used to drive drugs into thrombus or tissue for localized drug delivery remained to be investigated.

This study was motivated by the possibility of using laser-induced hydrodynamic pressure to drive clot-dissolving enzymes into clots or vessel wall tissue for the enhancement of laser thrombolysis. Specifically, the aim of this study has been to identify the mechanisms of photomechanical drug delivery through investigating how the target material, laser energy, absorption coefficient, fiber

size, repetition rate, and number of pulses affect the spatial distribution of photomechanically delivered drug. The process of photomechanical drug delivery was visualized by use of flash photography, and the acoustic pressure transients were measured with a piezoelectric polyvinlyidenefluoride (PVDF) transducer.

Photomechanical drug delivery was studied with gelatin-based thrombus models that eliminated the biological variation of thrombus and provided transparent samples for spatial distribution measurement. Solutions of a hydrophobic red dye in mineral oil were irradiated with a microsecond laser pulse to initiate drug delivery. We found that photomechanical drug delivery was associated with cavitation bubble formation and sound emission and that the deepest penetration followed the collapse of the cavitation bubble.

6.2 Materials and Methods

6.2.1 Laser Delivery

A flash-lamp-pumped dye laser (Palomar Medical Technologies) operating at 504 nm was used to create cavitation bubbles (Figure 6.1). This wavelength corresponded to the peak absorption of the light-absorbing dye used. The pulse duration was 1.3 μs (full width at half maximum). The laser energies varied from 30 to 100 mJ. Pulse-to-pulse energy variation was less than 5%. The repetition rate ranged from 1 to 10 Hz. The laser pulses were delivered by means of step-index fused-silica optical fibers with 300–1000 μm core diameters. The light was

always absorbed by the liquid surrounding the fiber tip. Three irradiation configurations were used. First, a flat optical fiber tip was perpendicular to a planar target (Figure 6.2a). Second, a flat optical fiber tip was coaxial with a cylindrical channel (Figure 6.2b). Third, a side-firing fiber (MicroQuartz Sciences) was coaxial in a cylindrical channel, but with irradiation perpendicular to the axis of the channel (Figure 6.2c)

6.2.2 Preparation of Thrombus Models

The thrombus was modeled with 3.5% gelatin (60–300 bloom). The percentage was determined by the weight ratio of gelatin to water. The bloom number is the standard method for indicating the toughness of gels and is a measure of surface tension. Higher bloom numbers indicate stronger gels. No attempt was made to correlate the bloom number with any specific clots in this study, although the range studied was similar to that of typical clot toughness. The gelatin-water mixture was heated to 60°C with stirring until it became clear. Liquid gelatin samples were poured into 1 cm cuvettes and molded to form 2–3 cm thick thrombus models with planar or cylindrical geometries. To simulate cardiovascular applications, the channels were constructed ∼2 mm in diameter under the assumption that some narrowing of the normal 2–4 mm adult human coronary artery is likely in a thrombotic lesion. The samples were transparent, and it was easy to use light microscopy to discriminate any colored substances from clear gelatin.

6.2.3 Preparation of Drug Models

I used solutions of a hydrophobic dye (D&C Red #17, Warner-Jenkinson) in mineral oil (Paddock Laboratories) as a model for the drug. The hydrophobic dye was used because the gels were water based and staining of the surface by the dye was undesirable. I added the dye to the mineral oil to achieve the desired absorption coefficient. I observed that no dye passively diffused into gelatin in control samples. The absorption coefficient of a solution was linearly proportional to the concentration of the dye in the oil: 0.0367 g of dye in 30 mL oil gave an absorption coefficient of 300 cm^{-1} at 504 nm. The absorption coefficients in our experiments varied from 50 to 300 cm^{-1}. The dye-oil mixture was heated to 100°C with stirring until the appearance became uniform and was then cooled to room temperature. A solution of 300 cm^{-1} was saturated at room temperature after 4 hours when the dye began to precipitate, and the absorption coefficient dropped to 250 cm^{-1}. The use of a sonicator (Medelco) for 10 min after the dye-oil solution was heated delayed the precipitation time for at least another hour.

6.2.4 Spatial Distribution Measurement

Planar Geometry

All planar targets were covered with 1.5 cm of colored oil. The target was clear gelatin ∼2 cm thick. Ten laser pulses were delivered through an optical fiber into the colored oil for each experiment (except in the study involving pulse number, in which 10–100 pulses were delivered). The fiber tip was positioned 1–5 mm above the target surface, as shown in Figure 6.1. The laser energy output was measured

with a joulemeter (J50LP, Molectron Detector) before and after each irradiation. Following photomechanical drug delivery, the samples were measured under a stereo-optical microscope (SZ6045, Olympus). The stained areas in the clear gels indicated the presence of photomechanically delivered colored oil. Figure 6.2(a) shows how the spatial distributions of colored oil in the gelatin were measured. The stained areas consisted of two parts: a hemisphere with width w and height h_{mix}, and some colored cracks extending a depth h_{crack}. The distances w, h_{mix}, and h_{crack} were measured on all four sides of each sample. The spatial distribution of the colored oil in the gels was measured as functions of laser energy (30–100 mJ), absorption coefficient of the oil (50–300 cm^{-1}), fiber size (300–1000 μm), gelatin strength (60–300 bloom), repetition rate (1–10 Hz), pulse number (1–100), and fiber position (1–5 mm above the ablated target).

Cylindrical Geometry

A clear gelatin sample with a 2 mm cylindrical channel was filled with colored oil. Fifty laser pulses were delivered coaxially through a cleaved fiber tip or perpendicularly through a side-firing fiber tip. The fiber tip was located in the middle of the channel. Following laser irradiation, the gel samples were carefully removed from the cuvette and then fixed in 10% formalin. They were then sectioned into 2 mm thick slices through both the irradiated and the nonirradiated sites after the colored oil in the channel was washed away with the formalin. To assess whether the process of photomechanical drug delivery could enhance intravascular recanalization, we measured the lumenal areas and then compared

them with control data measured from non-irradiated sections. The uniform penetration of colored oil in the gels was defined as $h_{\text{mix}}^{\text{coax}}$, whereas the colored cracks underneath $h_{\text{mix}}^{\text{coax}}$ were defined as $h_{\text{crack}}^{\text{coax}}$. The measuring method is shown in Figure 6.2b.

6.2.5 Visualization of Photomechanical Drug Delivery

Photomechanical drug delivery was visualized with flash photography (Figure 6.1). A triggerable CCD camera (CV-251, Protec) was used to photograph the processes. Each picture was a single event and was repeated three times for each parameter set. The bubble size was reproducible to 5% before the bubble collapse. The appearance of cavitation bubbles varied widely after the bubble collapse. A strobe (MVS–2601, EG&G) with a 5 μs pulse duration (full width at half-maximum) was used for illumination at an adjustable delay time (10–5000 μs) controlled by a digital delay generator (DG535, Stanford Research Systems). The generator was triggered by the laser pulse by use of a photodiode (UDT Instruments) that was attached to the laser delivery fiber. The delay time was defined as the period between the end of the laser pulse and the peak of the flash of light from the strobe.

6.2.6 Acoustic Pressure Measurement

The acoustic pressure measurements were intended for relative measurements of the acoustic pressure transients created by different laser parameters. A PVDF transducer (Hydrosonics) with a rise time of $\sim$1 μs was placed under the cuvette

(Figure 6.1). The acoustic signals were recorded on a digital storage oscilloscope (DSA 602A, Tektronix) through an amplifier (Hydrosonics). Only the maximum signals were recorded for the comparative study of the acoustic pressure transients.

6.2.7 Photomechanical Drug Delivery to Porcine Aorta

Photomechanical drug delivery to arterial tissue was evaluated by delivering blood and a $300\,\mathrm{cm}^{-1}$ oil solution onto porcine aorta. The porcine aorta specimens were divided into 2 cm $\times$4 cm and pinned to paraffin slabs. The inner surface was facing up for laser irradiation. Marker pins were placed 1 cm intervals before submerging the specimens under $\sim$2 cm of heparinized blood or the oil solution, leaving the marker pin exposed. The marker pins were used to direct the fiber to the ablation site. 50–100 laser pulses of 50–100 mJ via a 1000 μm fiber that was 1 mm above the specimens. Following laser irradiation, the specimen was removed and carefully washed with normal saline and then fixed in formalin. The specimens were studied under scanning electron microscopy and fluorescence microscopy.

6.2.8 Statistical Evaluation

All values are expressed as mean $\pm$ standard deviation. The statistical significance of differences in the penetration of photomechanically delivered dye in gels was determined by a two-tailed Student's t-test. An unpaired t-test was used to analyze the data as each parameter varied. Differences were considered

significant at p$\leq$ 0.05.

6.3 Results

6.3.1 Spatial Distribution Measurement

For simplicity, most of experiments were conducted on the samples with planar geometry. A cylindrical geometry was used to simulate the boundaries of vessel walls and to show the clinical possibilities of photomechanical drug delivery. The effects of laser parameters on photomechanical drug delivery were qualitatively the same for planar and cylindrical geometries, but the penetration was less in the cylindrical case. I defined w and w^{coax} as stained width (Figure 6.2). The parameters h_{mix}, h_{crack}, $h_{\text{mix}}^{\text{coax}}$, and $h_{\text{crack}}^{\text{coax}}$ were defined as penetration.

Planar Geometry

The spatial distribution measurements are summarized in Table 6.1. As the parameters increased, some increased the penetration (laser energy, absorption coefficient, and pulse number), some decreased the penetration (gelatin strength, fiber size, and the distance between the fiber and target surface), and one parameter had no significant effect on penetration (repetition rate).

Both penetration depths h_{mix} and h_{crack} increased significantly with increases in laser energy, absorption, and number of pulses. The penetration h_{mix} increased linearly, and h_{crack} increased with a steadily increasing slope. The stained width w was relatively independent of the laser energy and absorption coefficient, but it increased significantly as the number of pulses increased.

Increasing the gelatin strength, spot sizes, and the distance between a fiber tip and target surface caused both the penetration and the stained width to decrease significantly. Linear decreases in h_{mix} were observed, whereas h_{crack} decreased with steadily decreasing slope for each parameter. I found that the colored oil was easily driven into the low strength gel samples following irradiation. For example, the colored oil was driven into the weaker gel (60 bloom) after one or two pulses, but at least five pulses were needed to push the colored oil into the stronger gel samples (300 bloom). I observed that during irradiation with a 300 μm fiber the solution was explosively ejected and the solution in front of the fiber tip became dark, i.e., it was burnt. Irradiation with a 600 μm fiber was more violent than that with a 1000 μm fiber, but no explosive ejection was observed. The repetition rate did not affect the penetration ($p = 0.15 \sim 0.95$) or the stained width ($p < 0.4$) significantly.

Cylindrical Geometry

A cleaved fiber tip (300 μm in core diameter) was used to deliver 50 laser pulses of 30 mJ at 3 Hz into the light absorbing liquid (300 cm^{-1}) coaxially. The target was 3.5% gelatin (175 bloom). After laser irradiation, the lumen area increased up to 125%, and the colored oil was driven into the gels up to 1.5 mm ($h^{\mathrm{coax}}_{\mathrm{crack}}$ in Figure 6.2b). The maximum depth $h^{\mathrm{coax}}_{\mathrm{mix}}$ of uniformly stained layer was less than 250 μm. The stained width w^{coax} of the wall was $\sim$4 mm. One of these sectioned samples is illustrated in Figure 6.3.

A side-firing fiber was also evaluated. The output spot size of this tip was

$\sim$700 μm in diameter. Fifty laser pulses of 40 mJ at 3 Hz were delivered. The corresponding radiant exposure is 104 mJ/mm^2. The penetration was comparable with that of planar geometry for the same laser parameters. The measurements revealed that the deeper penetration was more easily achieved by side delivery than by coaxial delivery. The light photomicrography in Figure 6.4 illustrates that the colored oil is deeply driven into the gel ($\sim$1 mm) on the light delivery side and only superficially ($<$100 μm) elsewhere.

6.3.2 Visualization of Photomechanical Drug Delivery

In Figure 6.5, a series of pictures shows the process of photomechanical drug delivery on a gelatin sample (175 bloom) with planar geometry. The bubbles were formed in colored oil (300 cm^{-1}) with 30 mJ pulses delivered through a 300 μm core-diameter fiber. This corresponds to a laser radiant exposure of 424 mJ/mm^2. The fiber tip was positioned 1 mm above the target. The camera flash occurred from 25–1500 μs after the laser pulse. The cavitation bubble initially grew and interacted with the nearby gel. The maximum horizontal diameter of the bubble measured 2.4 mm and was reached at 110 μs. At $\sim$250 μs after the laser pulse, the bubble shrank to a minimum size and then rebounded slightly. A second maximum was observed at $\sim$300 μs and the bubble then shrank until $\sim$415 μs. At $\sim$500 μs a larger and less distinct shadow was seen, which may correspond to a final rebound of the bubble. This bubble size oscillation was reproducible. The bubble started its final collapse to the gel at $\sim$650 μs, and the maximum penetration into the gel was reached at about 1 ms. The shape of the bubbles was

not reproducible after the second rebound of the cavitation bubble. Evidently, the colored oil was driven into the gel as the result of the expansion and collapse of the bubble, and the deeper penetration of colored oil in gels was achieved following the collapse. I observed that the colored oil was pushed back to the surface because of the resistance of gels when the gels with higher mechanical strength (e.g., $\geq$175 bloom) were used during single pulse irradiation. This is seen at 1.5 ms.

Photomechanical drug delivery on a gelatin sample (175 bloom) with cylindrical geometry is shown in Figure 6.6. In this experiment, a 30 mJ laser pulse was delivered through a 300 μm core-diameter fiber into colored oil with absorption coefficient 300 cm^{-1}. The channel wall was dilated during the cavitation bubble expansion. The maximum dilation was reached after $\sim$100 μs, and amounted to 120% of the initial channel diameter. During the bubble collapse the channel wall invaginated, and the solution in the channel was pushed away from the fiber tip in both lateral and forward directions, which caused dilation and invagination along the channel wall until the end of the event. It took approximately 5 ms for the channel to return its original shape after a laser pulse. The minimum diameter was about 90% of the original value. I took the images on one sample rather than on a fresh sample each time to avoid misinterpretation of initial intrasample defects before irradiation.

Figure 6.7 shows a cavitation bubble developing between the side-firing fiber tip and the surface of the cylindrical channel after the delivery of a 40 mJ energy laser pulse. The corresponding radiant exposure is $\sim$104 mJ/mm^2. The other

parameters were the same as those in Figure 6.6. The images were recorded between 25 μs and 1 ms after laser radiation. The cavitation bubble was formed directly on the side surface of the fiber tip where the laser energy was absorbed. The maximal development of the laser-induced elliptical cavitation bubble is seen at 100 μs after the laser pulse. The corresponding bubble diameter and height were 1.7 and 1.2 mm, respectively. The bubble reached its minimum size at 250 μs, and penetrated $\sim$1.5 mm into the gelatin at $\sim$1 ms. No bubble oscillation was observed. The bubble did not penetrate the channel wall when the laser pulse was less than a 5 mJ. The bubble penetrated deeper into the gel at higher laser energies (i.e., $>$40 mJ). No displacement of the tip was observed during the irradiation. In this experiment the distance between the bubble site and the target was $\sim$400 μm and the gelatin was as thick as 4 mm. The initial channel wall surface was not so smooth as a planar surface and was often associated with some defects. These differences may contribute to the differences in the bubble formation in Figures 6.5 and 6.7, although the spatial distribution measurements were comparable. The images were taken on one sample, as explained above.

Flash photography also led to the following observations: (1) Increasing energy (Figures 6.8 and 6.9), absorption coefficient (Figures 6.10 and 6.11), and radiant exposure (Figures 6.5 and 6.8) increase the bubble size and the penetration of colored oil in the gel and delay the time of the maximum bubble size. For example, the bubble diameter was 2.7 mm at 110 μs when a 100 mJ laser pulse was delivered into the solution (300 cm^{-1}) through a 1000 μm fiber positioned 1 mm above the target, whereas it was 1.6 mm at 45 μs as 30 mJ of energy was delivered

instead. (2) Increasing the target strength does not affect the bubble size unless the expanding bubble interacts with the target (Figures 6.12 and 6.13). If this occurs both the bubble size and the penetration of colored oil are reduced. (3) Increasing the distance between the fiber tip and the target decreases the penetration of colored oil in the gel, creates larger cavitation bubbles, and delays the time of the maximum bubble size (Figures 6.14 and 6.11). (4) Cavitation bubbles formed in cylindrical channels were smaller than those formed in unbounded solutions because of the boundary effect. (5) Multiple pulses affect the bubble formation — sometimes making the bubbles smaller, sometimes larger compared with the bubbles generated by single pulses (Figure 6.15). The penetration of colored oil into the gel increases with more pulses.

6.3.3 Acoustic Pressure Measurement

Flash photography and a PVDF transducer were used to correlate the bubble size with the pressure transients. The acoustic measurements were qualitative and the measured pressure might be underestimated because of the slow response of the transducer and the multiple boundaries between the initial acoustic event and the transducer. I observed that the acoustic pressure transients were proportional to the bubble size and that bubbles of similar size created by different-size fibers generated similar maximum acoustic pressure transients. The acoustic measurements provided a quick qualitative check of the maximum bubble size observed visually.

6.3.4 Photomechanical Drug Delivery to Porcine Aorta

Figure 6.16 shows a typical photo of the inner surface of porcine aorta exposed to one hundred pulses of 90 mJ from a 1000 μm fiber placed 1 mm away from the surface. The fluorescence microscopy of irradiated aorta samples (exposed to the oil solution) revealed that a uniform moderate level of fluorescence was even throughout most samples irradiated with 30–150 pulses of 150 mJ via a 1000 μm fiber, while the top 25–50 μm fluoresced more strongly. Considerable tissue disruption (up to 800 μm deep) was observed when more than 30 pulses were delivered under scanning electron microscopy. Evidently, the fluorescence on the surface of aorta specimens was enhanced after the photomechanical drug delivery procedure. However, it was difficult to discriminate the autofluorescence of the aorta sample from the fluorescence of the dye since a low level of fluorescence occured throughout the non-laser control samples.

6.4 Discussion

The major objective of this study was to investigate the feasibility of a photomechanical technique to deliver clot-dissolving enzymes into clots to enhance laser removal of the clots. I investigated the effects of laser parameters on the spatial distribution of photomechanically-delivered colored oil (a drug model) in gelatin-based thrombus models. I used clear gel samples covered with colored oil to determine the spatial distribution of delivered drug. A stained area in the clear gel indicated the presence of colored oil delivered photomechanically.

No dye passively diffused into the clear water-based gels. The colored oil was driven into the gels following irradiation, cavitation bubble formation, and secondary acoustic emission. When no cavitation bubble was formed, no gelatin was stained. Normally, deeper penetration was accompanied by louder popping sounds. Acoustic pressure transients were detected during the expansion and collapse of the cavitation bubble. The spatial measurements also revealed that higher pressures resulted in deeper penetration. These findings suggest that cavitation bubble formation is crucial in photomechanical drug delivery and that acoustic events can be used as a means of monitoring the efficacy of photomechanical drug delivery *in vivo*.

This study demonstrated that the drug was most likely driven into the clot by hydrodynamic flow that was due to the cavitation bubble formation, inasmuch as the acoustic transients arising from the bubble formation since the acoustic transients passed through the sample and reached the transducer before the colored oil was forced into the gelatin. In this sense, the term photomechanical drug delivery may be more appropriate for the type of drug delivery described in this study. However, it remains unclear whether the acoustic transients contribute to the delivery through other mechanisms that might weaken the gelatin before the onset of hydrodynamic flows.

At least four limitations are associated with the models used in this study. First, the gelatin-based thrombus models did not work perfectly with multiple pulse studies because they were easily melted or fractured; real clots tend to be more durable. Second, it may be harder to deliver oil-based dye than aqueous

dyes because of viscosity effects. Third, the colored oil at high absorption coefficients (e.g., 300 cm^{-1}) was easily burnt when laser pulses with high energy (e.g., 100 mJ through a 1000 μm core fiber) or high radiant exposure ($\geq$212 mJ/mm^2, or, say, 60 mJ through a 600 μm core fiber) were used. The burnt solution surrounding the fiber tip sometimes caused the photomechanical delivery process to become nonreproducible. It was observed that the color of the solutions sometimes became darker after multiple pulse irradiation. Fourth, all cavitation events in this model were initiated at the fiber tip. Photomechanical drug delivery may be significantly different when the cavitation bubble is formed directly on a target because of the absorption of the laser pulse by the target.

6.4.1 Effect of Cavitation Bubble Formation

Photoacoustically delivered colored oil in a planar geometry was uniformly distributed as an inverted hemisphere layer and in a cylindrical geometry as a ball-shaped profile. The uniformly stained layer looked like a dye-gelatin mixture (i.e., the gel itself rather than small colored oil droplets became stained) under light microscopy and could not be washed away by clear oil or wicked off by a piece of tissue paper. Colored cracks were formed below the uniformly stained layer.

The shape of colored cracks was not reproducible, and the cracks were not always associated with the uniformly stained layers. For example, no colored cracks (i.e., h_{crack} =0) were formed by ten 60 mJ laser pulses through a 1000 μm core fiber in a colored oil (50 cm^{-1}), but colored cracks 400 μm in depth were

formed by the same laser parameters when a different colored oil ($300\,\mathrm{cm}^{-1}$) was used (see Table 6.1). Light microscopy showed that the cracks were formed as the result of defects in gel structure. No defects were observed in the position where the cracks were formed before the irradiation. This suggests that the formation of the uniformly stained layers and that of the cracks are mediated by separate processes. These separate processes may be used to advantage in clinical applications. For example, drugs can be uniformly delivered into thrombus or deposited in an arterial wall or deeply delivered into plaque underneath the thrombus by fracture.

Colored oil in a planar geometry was driven into the gels even when the expanding bubbles had no contact with the gels (although the collapsing bubble always did). The penetration h_{mix} increased but the stained width w remained relatively constant when h_{crack} was zero (cf. Figure 6.2(a)). These observations imply that h_{mix} depends on the hydrodynamic forces arising from both the expansion and the collapse. A uniform colored layer is formed when the forces are below the yield strength of the gelatin structure, whereas cracks are formed when the forces exceed those needed to fracture the gelatin.

Gross physical displacement of the cuvette containing the irradiation targets occurred after the laser pulse. The magnitude of the displacement increased as the bubble size increased. For example, the cuvette rebounded more than 2 mm when the bubble diameter was $\sim$4 mm, but no displacement was observed for a 1.3 mm bubble. The direction was opposite that of laser delivery. The bubble energy obtained with Rayleigh's bubble formula [97, 98, 110] accounts for only a

small fraction of the laser energy (<1%). This raises the question: How was the majority of the energy dissipated during the process? I hypothesize that the delivered laser energy is dissipated mainly through heating, phase changes, acoustic transients, and hydrodynamic flow of liquid. Hydrodynamic flows ultimately lead to movement of the cuvette.

6.4.2 Geometric Effect

Photomechanical drug delivery was qualitatively the same for both planar and cylindrical geometries, but the penetration was less in the cylindrical case. Flash photography showed that the fiber tip affected the cavitation bubble growth: bubbles grew faster in the radial and forward directions. The bubble did not move radially and migrated away from the fiber tip on collapse. Strong hydrodynamic flows were associated with the bubble collapse and may be the reason that deeper penetration was achieved by perpendicular delivery rather than by coaxial delivery. Collapsing bubbles migrated toward the target in both perpendicular and side-firing delivery (see Figures 6.5 and 6.7). This finding suggests that the side-firing light-delivery devices may be promising for photomechanical drug delivery in vascular applications.

No mass removal was observed for the samples with planar geometry. However, in a cylindrical geometry light microscopy revealed that the lumen size increased by as much as 1.5 mm after multiple pulses. I hypothesize that gelatin removal in the cylindrical channel is due to hydrodynamic flow and to a thermal effect. Hydrodynamic flow was exerted directly on the planar surface, and

the flow passed over the channel surface in a cylindrical geometry. Melted gelatin may resolidify at the planar surface, whereas in a cylindrical geometry the melted gelatin may be carried away.

When the laser pulses were delivered perpendicularly, the deepest penetration was observed in front of the fiber tip. In a channel with coaxial delivery the deepest penetration was inside the channel wall ∼1 mm from the distal face of the fiber (see Figure 6.6). This most likely is the result of bubbles' propagating away from the fiber face. Also, bubble movement may be a reason that w^{coax} was ∼4 mm long.

The presence of boundaries reduced the maximum size of the cavitation bubble. For example, a 30 mJ laser pulse delivered through a 300 μm fiber created a 1.9 mm diameter bubble in a 2 mm diameter channel filled with a 300 cm^{-1} colored oil (Figure 6.6), but a 2.9 mm bubble was created in an unbounded colored oil at the same energy (picture not shown). To estimate the energy lost to the dilatation of the channel wall after a 30 mJ laser pulse, we compared the maximum bubble radius in both cases using Rayleigh's bubble formula. The result indicated that ∼30% of the bubble energy was dissipated in the dilatation process.

6.4.3 Multiple-pulse Effects

A surprising observation was that the stained width on the surface was relatively independent of the laser energy and absorption coefficient when laser pulses were delivered perpendicularly. The interface ($w_{\text{interface}}$ in Figure 6.5) was smaller

than the stained width w (Figure 6.2(a)) for single-pulse events. Flash photography revealed that the cavitation bubble sizes varied during the multiple-pulse irradiation (see Figure 6.14). This phenomenon was supported by the acoustic pressure measurements. Sometimes the amplitude of acoustic signals during multiple pulses was ten times that of a single pulse, and at other times no signal was detected. The variation in bubble size and acoustic transient amplitude is possibly not caused by the changes in the laser pulse energy when multiple pulses were delivered because the variation was less than 5%. The independence of the stained width from laser energy and absorption coefficient seems to be a side effect of multiple pulses.

The effect of multiple pulses on both the penetration and the stained width was significant (see Table 6.1). I found that the deeper penetrations, especially h_{crack} and $h_{\text{crack}}^{\text{coax}}$, were more easily achieved by multiple pulses than by the combinations of other laser parameters. Sequential bubble collapses likely weakened the gelatin structure, and the colored oil was easily driven into fractured lines.

I observed that, when the gelatin strength was greater than 60 bloom, colored oil could not be deposited on the gel surface with a single pulse. This finding suggests that the oil entrainment may be caused by mechanical rather than thermal means despite a high initial temperature of the cavitation bubble (above 300°C calculated by a partial vaporization theory [83, 84]). Presumably significant cooling has occurred by the time the bubble reaches the gelatin surface. Mechanical vibration owing to the hydrodynamic forces has been shown to liquefy gelatin [123]. However, the thermal effect may contribute to melting during

multiple pulse irradiation because of successive amounts of heat deposited on the gelatin surface with each bubble expansion.

Multiple-pulse variation of bubble dimensions has been reported by van Leeuwen *et al.* [124]. A new observation made in our study is that small gas bubbles (<50 μm) around the fiber tip played an important role in the bubble dynamics. After a laser pulse, long-lasting (several seconds) small gas bubbles were often formed around the fiber tip. Cavitation bubble size was reproducible when no gas bubbles were present; otherwise the cavitation bubble size could change significantly. This finding suggests that the use of degassed solution may reduce the effect of multiple pulses on the bubble dynamics, although, of course, this is impossible in an *in vivo* environment.

6.4.4 Similar Effects

The same radiant exposure using different-size fibers produces different-size bubbles. Furthermore, the same pulse energy using different-size fiber also produces different-size bubbles. However, similar maximum cavitation bubble sizes can be produced by different sets of laser parameters. For example, a cavitation bubble 3.2 mm in diameter can be produced in unbounded colored oil (300 cm^{-1}) by a 300 μm fiber at 33 mJ, by a 600 μm fiber at 50 mJ, or by a 1000 μm fiber at 100 mJ, with an error estimate of less than 5%. The maximum acoustic signals were similar for similar bubble sizes. Similar spatial distributions of colored oil in gels were achieved with the three sets of parameters mentioned above when the fibers were located 1 mm above the gelatin (175 bloom) samples.

Alternatively, 60 mJ laser energy delivered by a 1000 μm fiber and ten additional pulses (data not shown) also can be used instead of 100 mJ laser energy to yield equal penetration. These findings suggest that similar drug delivery can be achieved by various combinations of laser parameters. Furthermore, photomechanical drug delivery may be safer in a smaller laser delivery catheter because one can use a lower energy to achieve equivalent penetration by using more pulses.

Cavitation bubble formation in this study is similar to that of a Q-switched holmium laser in water. The absorption coefficient of water at 2.1 μm is 30 cm^{-1}. The Q-switched pulse length is $\sim$1 μs and is therefore comparable with those used in this study. In this study and in those of Jansen *et al.* the cavitation bubbles are formed at the fiber tip after the laser pulse owing to the laser energy absorption by the liquid [84]. The Q-switched holmium laser can be used for photomechanical drug delivery, although Table 6.1 indicates that the penetration will be half that of a 577 nm pulsed dye laser in blood (absorption coefficient of 300 cm^{-1}). The pulse duration for the free-running holmium laser is much longer ($\sim$250 μs) and the bubble dynamics are completely different because the cavitation bubble is formed during the laser pulse.

This study showed that drug could be delivered into arterial tissue using photomechanical drug delivery. However, the dye-oil solution is not suitable for photomechanical drug delivery to arterial tissue, since it was difficult to discriminate the autofluorescence of the aorta sample from the fluorescence of the dye.

In conclusion, I have demonstrated the feasibility of photomechanical drug delivery to drive drugs (colored oil) into thrombus (a gelatin-based model). The

results of this study indicate that cavitation bubble formation is the governing mechanism for photomechanical drug delivery with microsecond laser pulses in light absorbing liquids. When no cavitation bubble was formed, no gelatin was stained. There are two processes in photomechanical drug delivery: the formation of uniformly stained layers and the formation of colored cracks. The two separate processes may benefit clinical applications. The deepest penetration of colored oil in gels follows the cavitation bubble collapse. The penetration was less than 500 μm when the gelatin structure was not fractured, and the colored oil could be driven a few millimeters into the gels in both axial and radial directions. The results of this study demonstrated that similar penetration could be achieved by use of various combinations of laser parameters. Photomechanical drug delivery may be used for drug delivery to arterial tissue.

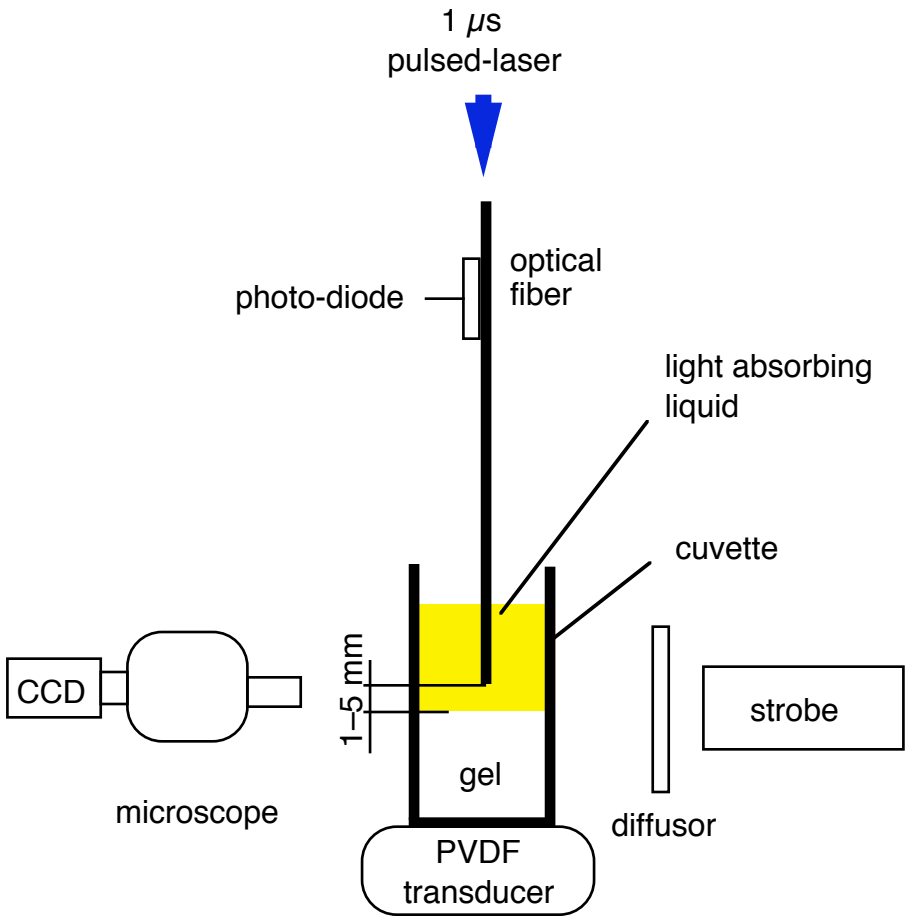

Figure 6.1: Experimental setup for the spatial distribution measurement, flash photography, and acoustic pressure measurement.

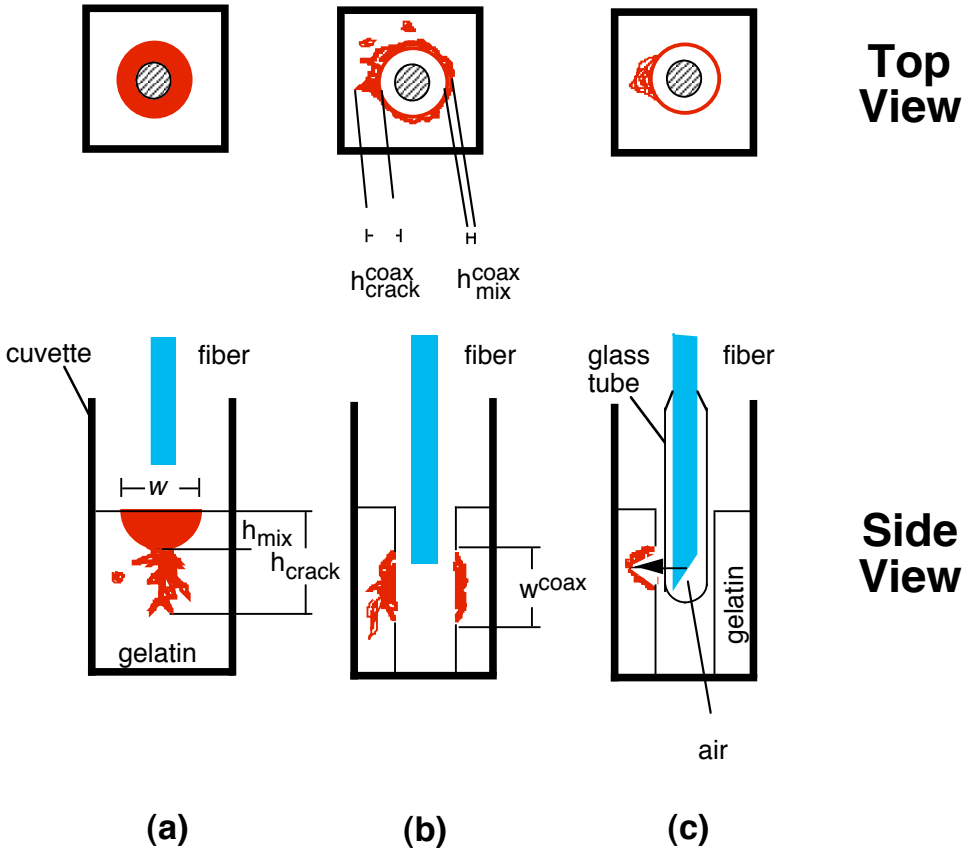

Figure 6.2: Schematic illustration of three irradiation configurations and the methods used for measuring the spatial distribution of photomechanically delivered dye in clear gels. The top and side views of samples irradiated by perpendicular, coaxial, and side irradiation are shown in (a), (b), and (c) respectively.

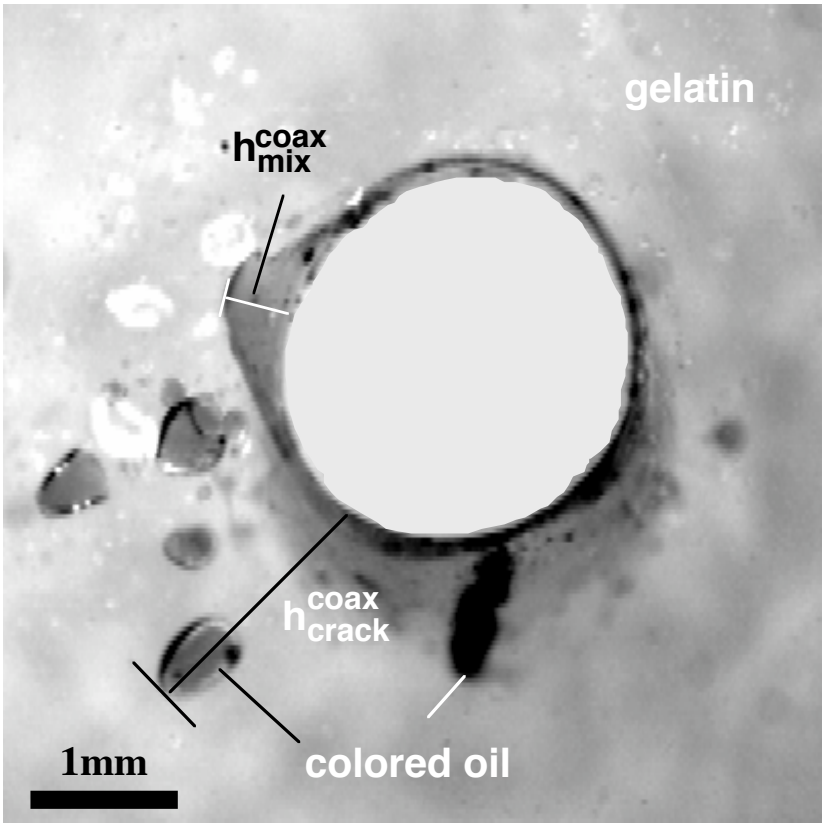

Figure 6.3: Top view of colored oil distribution in a 2 mm channel through gelatin (175 bloom) with cylindrical geometry after 50 pulses of 30 mJ laser energy through a 300 μm core diameter fiber in 300 cm^{-1} colored oil. The laser energy was delivered coaxially. Extensive shadows are present because this section was 2 mm thick.

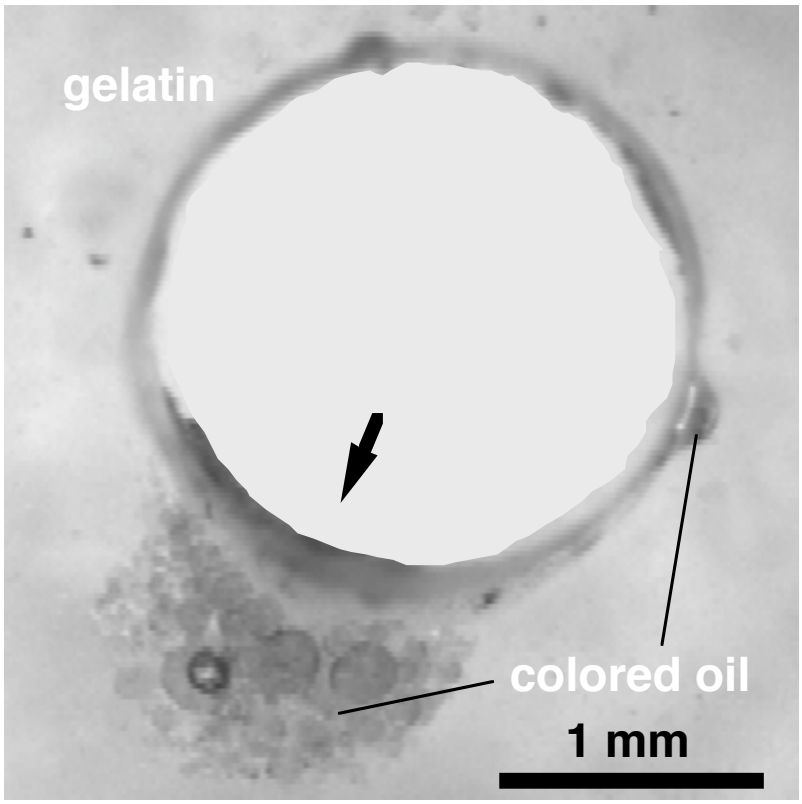

Figure 6.4: Top view of colored-oil distribution in a 2 mm channel through gelatin (175 bloom) with cylindrical geometry after 50 pulses of 40 mJ laser energy through a side-firing fiber in 300 cm^{-1} colored oil. The laser energy was delivered perpendicular to the channel wall as indicated by the arrow.

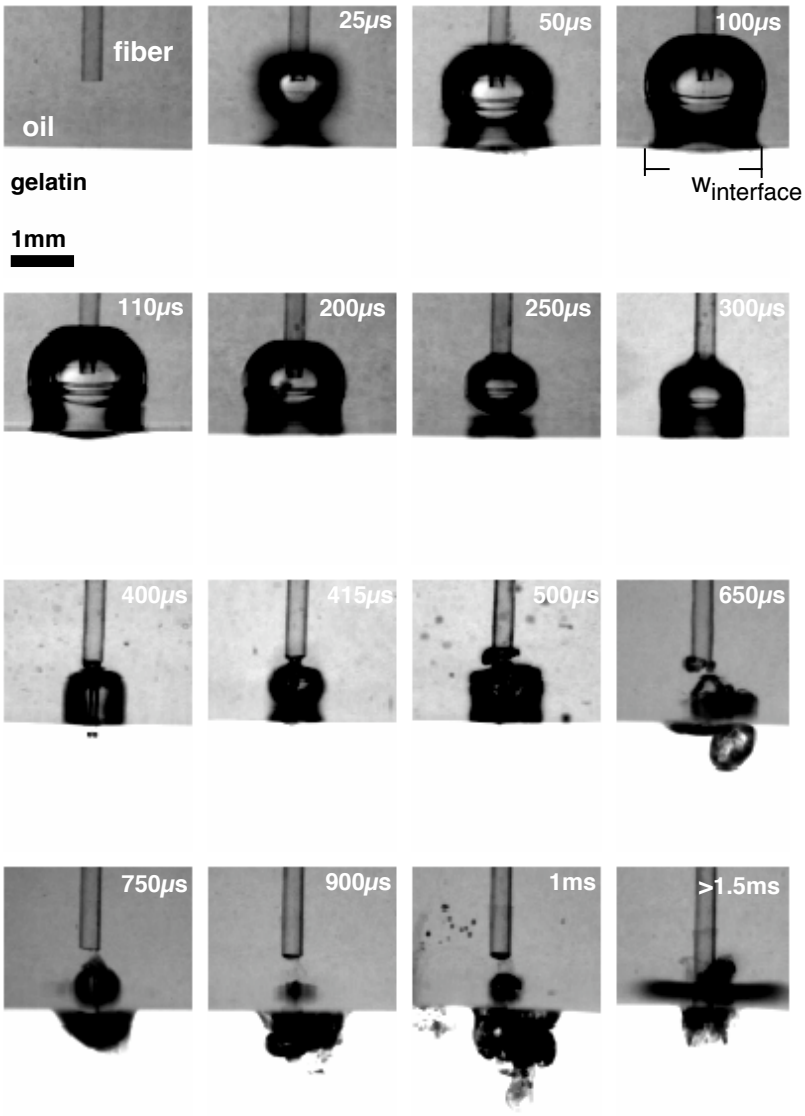

Figure 6.5: Side views of photomechanical drug delivery on gelatin (175 bloom) with a planar geometry. A single pulse of 30 mJ laser energy was delivered through a 300 μm diameter fiber. The absorption coefficient was 300 cm^{-1}. The fiber was located 1 mm above the gel surface. The backgrounds of four photographs (300–500 μs) are lighter than the rest because of the different illumination. The bubble size was reproducible to 5% before the second rebound of the cavitation bubble (500 μs). The appearance of cavitation bubbles varied widely after 500 μs.

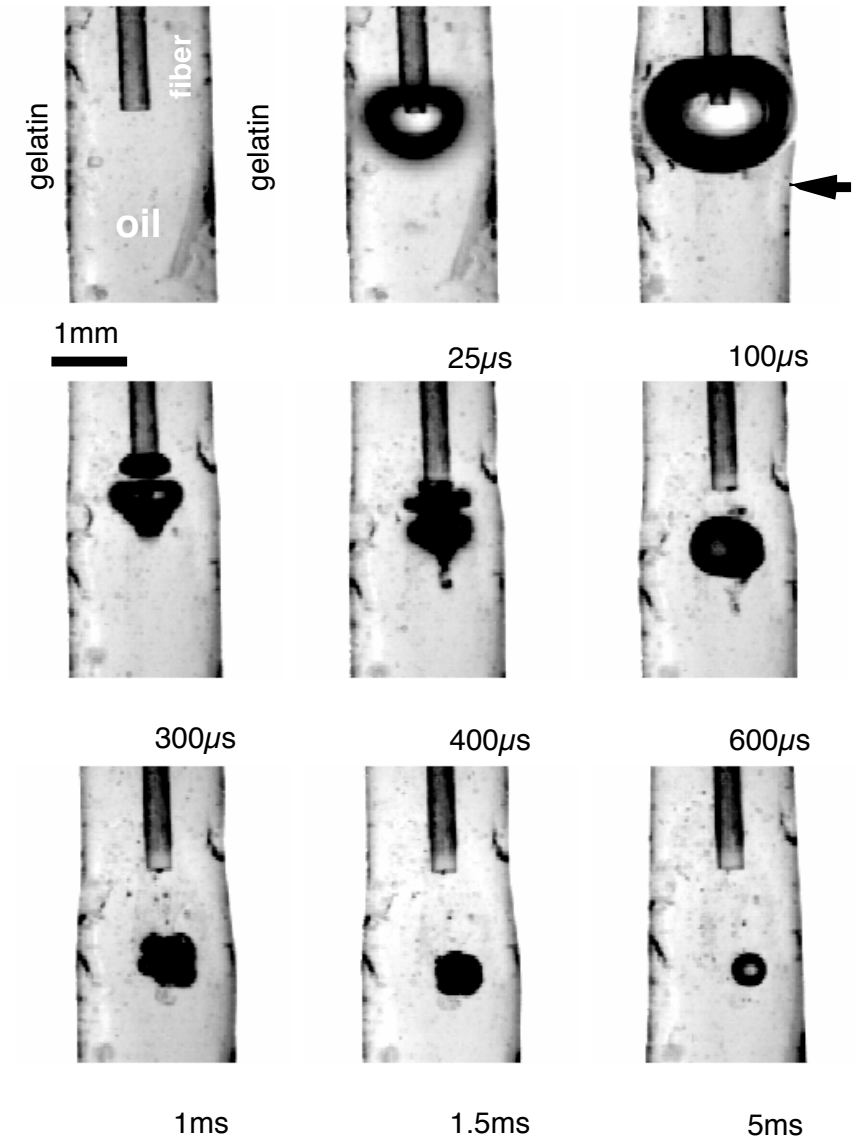

Figure 6.6: Side views of photomechanical drug delivery on gelatin (175 bloom) in a cylindrical geometry. A single pulse of 30 mJ laser energy was delivered through a 300 μm diameter fiber into 300 cm^{-1} colored oil. The absorption coefficient was 300 cm^{-1}. The laser energy was delivered coaxially. The arrow indicates the place where the deepest penetration was observed.

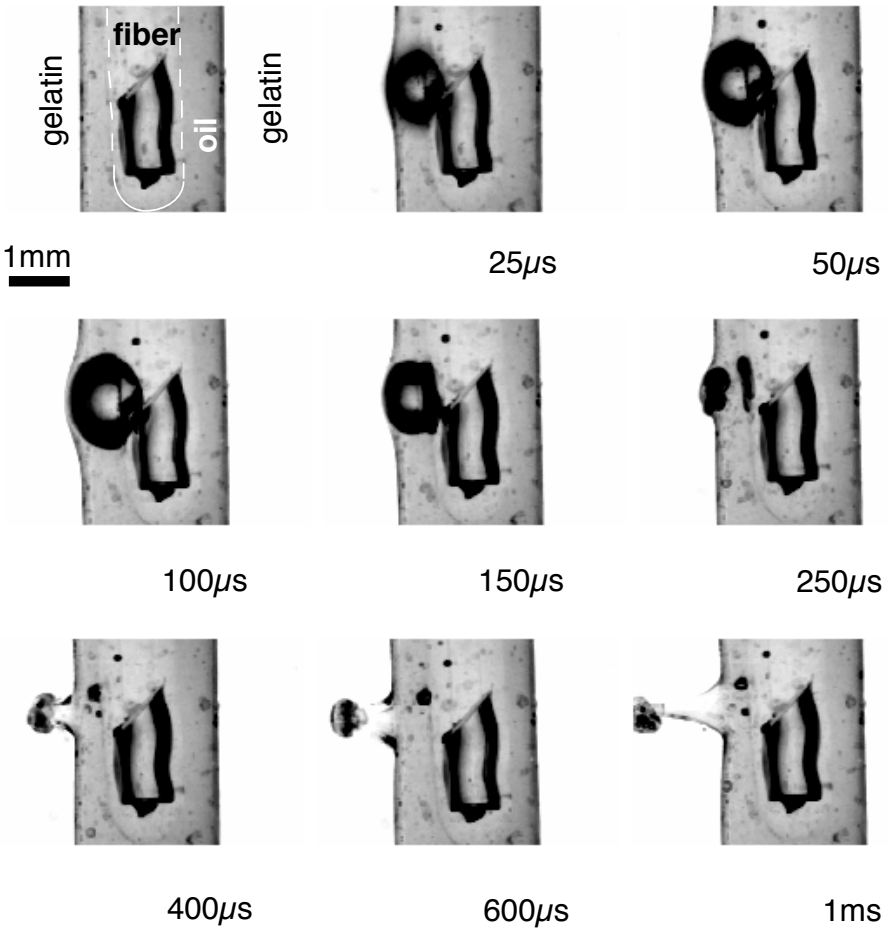

Figure 6.7: Side views of photomechanical drug delivery on gelatin (175 bloom) with cylindrical geometry. A single pulse of 40 mJ laser energy was delivered perpendicularly to the channel through a side-firing fiber into 300 cm^{-1} colored oil. The white dashed curve shows the edge of the side-firing fiber tip. The dark areas inside the fiber tip are due to the index mismatch at the air-oil interface.

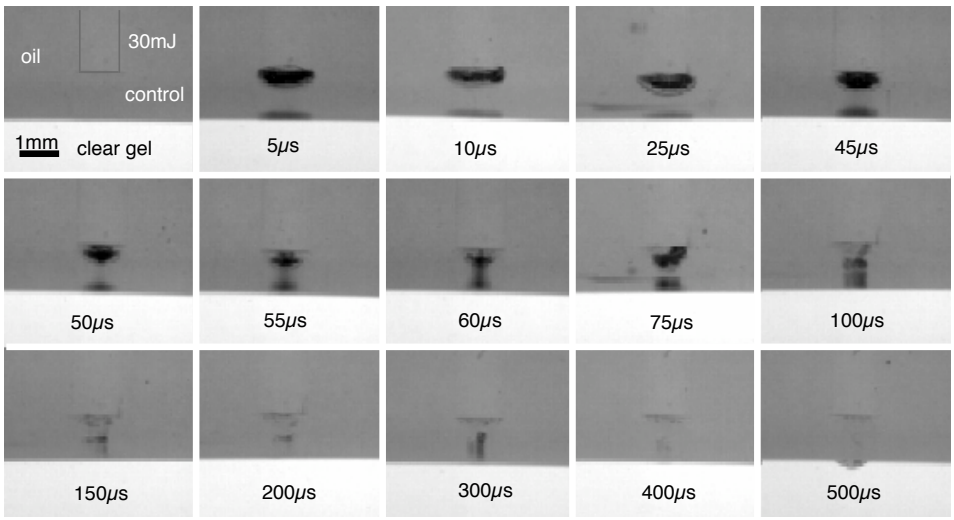

Figure 6.8: Side views of photomechanical drug delivery on gelatin (175 bloom) with a planar geometry. A single pulse of 30 mJ laser energy was delivered through a 1000 μm diameter fiber. The absorption coefficient was 300 cm^{-1}. The fiber was located 1 mm above the gel surface.

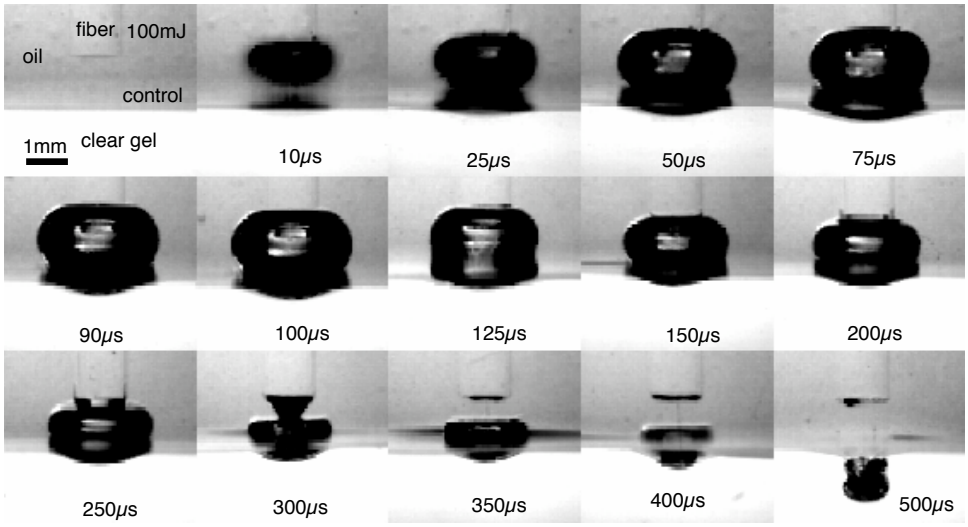

Figure 6.9: Side views of photomechanical drug delivery on gelatin (175 bloom) with a planar geometry. A single pulse of 100 mJ laser energy was delivered through a 1000 μm diameter fiber. The absorption coefficient was 300 cm^{-1}. The fiber was located 1 mm above the gel surface.

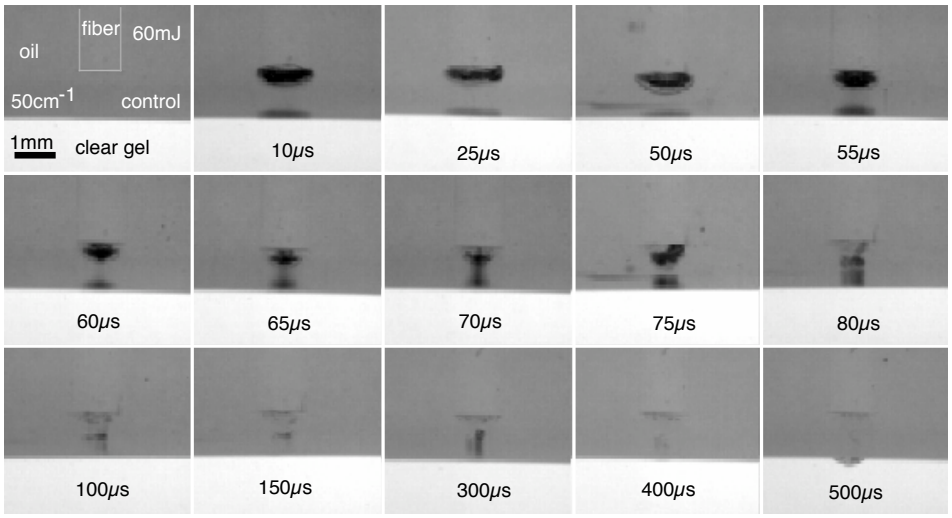

Figure 6.10: Side views of photomechanical drug delivery on gelatin (175 bloom) with a planar geometry. A single pulse of 60 mJ laser energy was delivered through a 1000 μm diameter fiber. The absorption coefficient was 50 cm^{-1}. The fiber was located 1 mm above the gel surface.

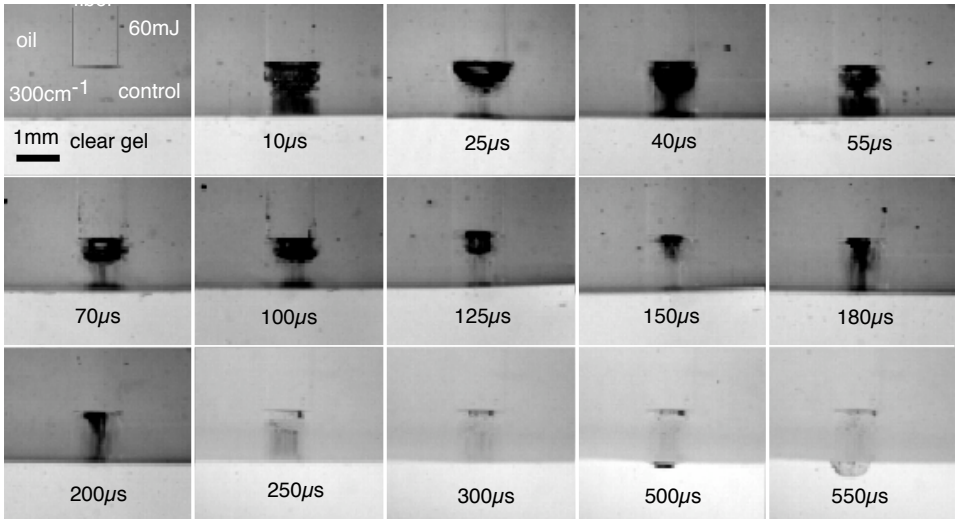

Figure 6.11: Side views of photomechanical drug delivery on gelatin (175 bloom) with a planar geometry. A single pulse of 60 mJ laser energy was delivered through a 1000 μm diameter fiber. The absorption coefficient was 300 cm^{-1}. The fiber was located 1 mm above the gel surface.

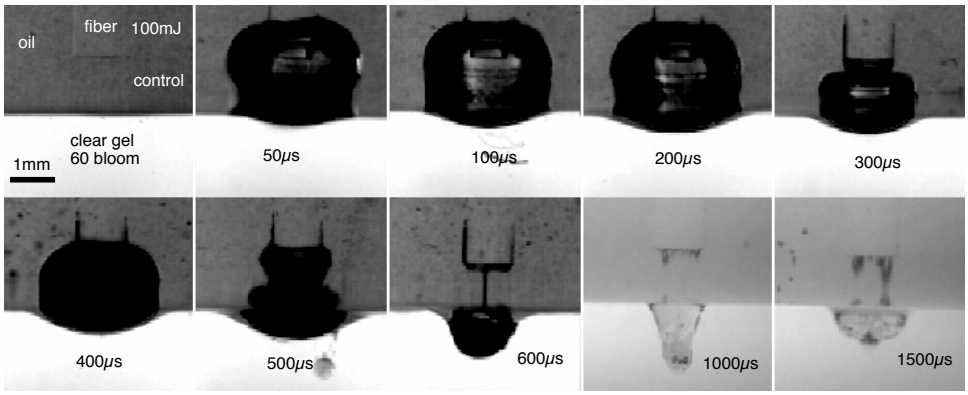

Figure 6.12: Side views of photomechanical drug delivery on gelatin (60 bloom) with a planar geometry. A single pulse of 100 mJ laser energy was delivered through a 1000 μm diameter fiber. The absorption coefficient was 300 cm^{-1}. The fiber was located 1 mm above the gel surface.

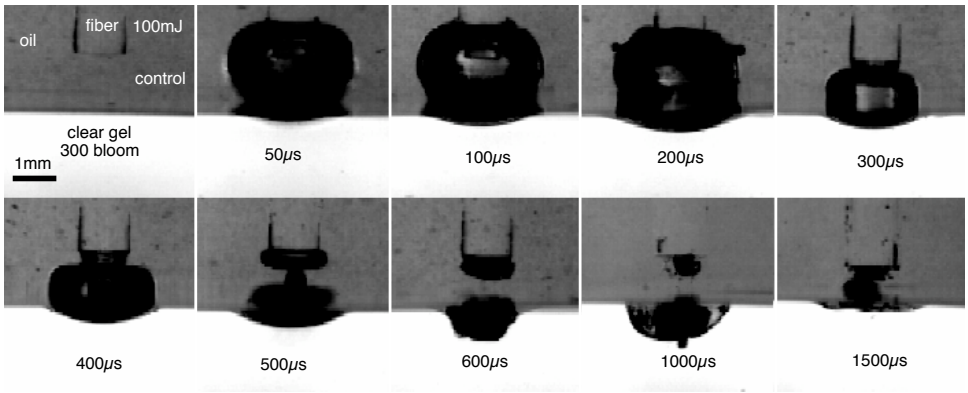

Figure 6.13: Side views of photomechanical drug delivery on gelatin (300 bloom) with a planar geometry. A single pulse of 100 mJ laser energy was delivered through a 1000 μm diameter fiber. The absorption coefficient was 300 cm^{-1}. The fiber was located 1 mm above the gel surface.

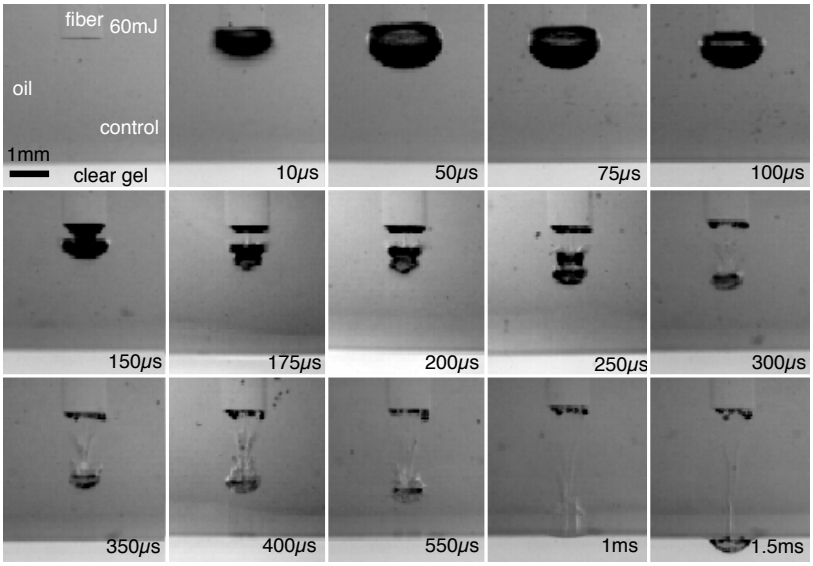

Figure 6.14: Side views of photomechanical drug delivery on gelatin (175 bloom) with a planar geometry. A single pulse of 60 mJ laser energy was delivered through a 1000 μm diameter fiber. The absorption coefficient was 300 cm^{-1}. The fiber was located 5 mm above the gel surface.

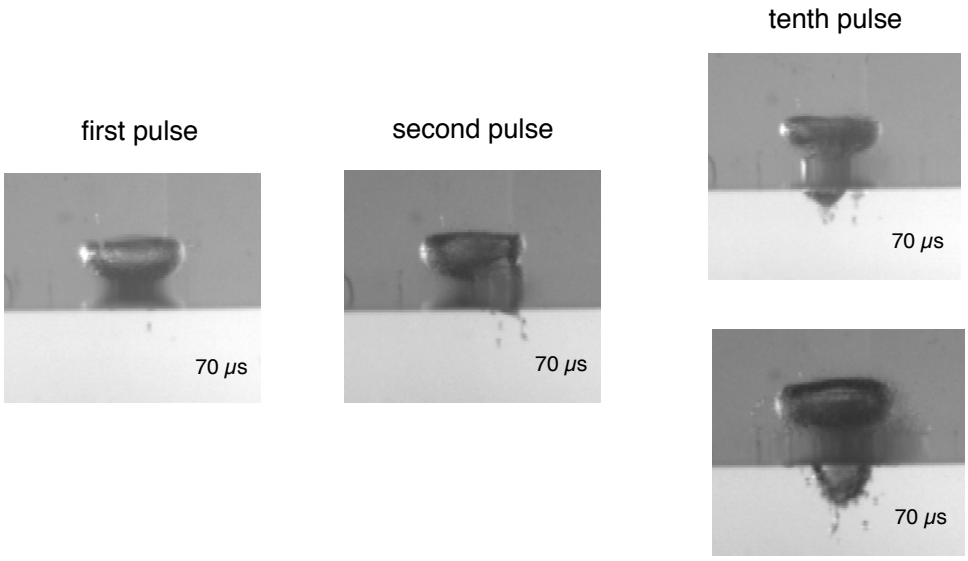

Figure 6.15: Side views of laser-induced cavitation bubble at a fiber tip placed 1 mm above the gel surface (1750 bloom). Single pulses of 60 mJ laser energy were delivered through a 1000 μm diameter fiber. The absorption coefficient was 300 cm^{-1}. The images were taken at the same exposure time, but after different pulses.

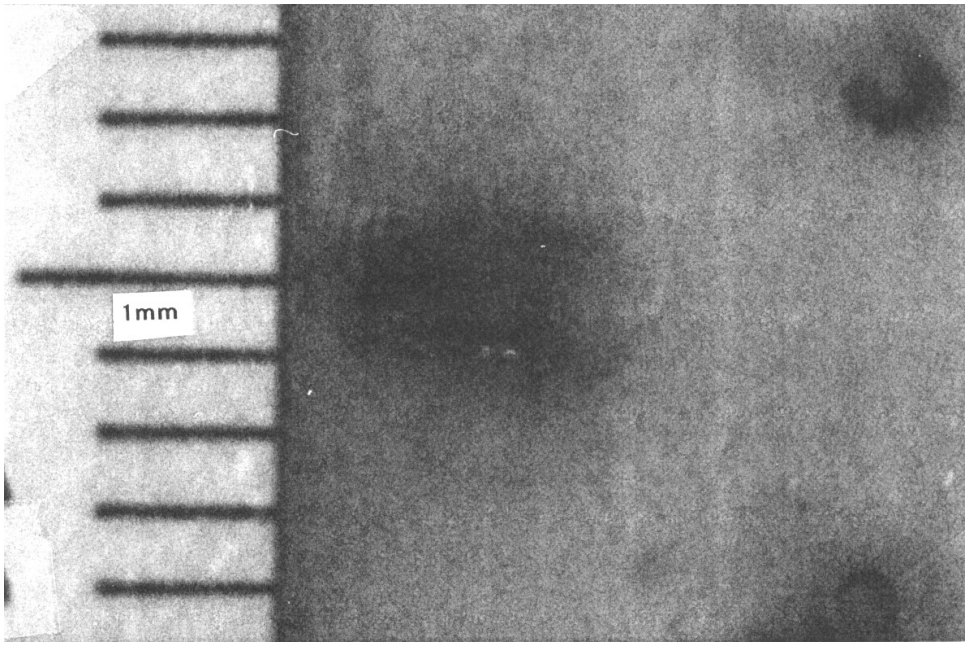

Figure 6.16: Inner surface of porcine aorta exposed to one hundred pulses of 90 mJ from a 1000 μm fiber placed 1 mm away from the surface.

Delivery Parameters							Measurements		
Energy (mJ)	Absorption Coefficient (cm^{-1})	Number of Pulses	Gelatin Strength (bloom)	Fiber Size (μm)	Fiber Position (mm)	Repetition Rate (Hz)	h_{mix} (mm) ± 0.05	h_{crack} (mm) ± 0.2	w (mm) ± 0.2
30→100	300	10	175	1000	1	3	0.12→0.18	0.1→0.5	2.0→2.3
60	50→300	10	175	1000	1	3	0.07→0.15	0.0→0.4	1.9→2.0
60	300	10→100	175	1000	1	3	0.15→0.53	0.4→1.9	2.0→2.8
60	300	10	60→300	1000	1	3	0.25→0.10	0.8→0.2	2.1→1.5
60	300	10	175	300→1000	1	3	0.18→0.15	1.0→0.4	3.2→2.0
60	300	10	175	1000	1→5	3	0.15→0.06	0.4→0.0	2.0→1.0
60	300	10	175	1000	1	1→10	0.13→0.16	0.1→0.4	1.8→2.1

Table 6.1: Spatial distribution measurements of colored oil in gels with planar geometry. All data are the average of five samples. The error estimates are standard deviations.

Chapter 7

Enhanced Thrombolysis with Photomechanical Drug Delivery: An *In vitro* Study

7.1 Introduction

Laser thrombolysis is a promising method of clearing arteries that are obstructed by thrombus and plaque [1]. It has potential advantages over bypass surgery, balloon angioplasty, and other forms of vascular interventions. Laser pulses can be delivered into arteries through fiber-optic catheters, thus avoiding major surgery. The thrombus is removed by the laser pulses rather than being displaced by them, thereby, potentially reducing the high rate of restenosis that occurs with balloon angioplasty. The laser energy is well absorbed by the thrombus and poorly absorbed by the adjacent tissue. Thus, the selective and safe thrombolysis using laser radiation can be achieved. The use of small fiber-optic catheters offers the possibility of removing thrombus in small vessels (e.g., brain vessels) or in larger vessels (e.g., bypass grafts), in which no effective therapies

are available [57]. However, one concern for laser thrombolysis is the mural blood clot left in arteries after the laser thrombolysis procedure, which may be a potential limitation for this therapy. I hypothesize that the combination of laser thrombolysis and localized intramural delivery of clot-dissolving drugs during the procedure may be a solution to the limitation, i.e., the majority of clots can be removed by laser pulses, whereas the mural clot is dissolved by the drugs. This study was motivated by this hypothesis.

Current techniques for localized drug delivery use balloon-based catheters to infuse thrombolytic agents into thrombus at an angioplasty site. The intramural deposition of therapeutic agents may provide prolonged thrombolytic action at infusion site [70]. Basically, two mechanisms are involved in these procedures: 1) displacement of thrombus due to the balloon dilation and 2) thrombolytic action by therapeutic agents. However, the primary problems with the modified balloon catheter designs are their cumbersome size and long inflation times required, as well as the risk of medial injury occurring during the balloon inflation process, thus potentially limiting the benefits of local drug delivery.

In Chapter 6 I demonstrated that drug could be delivered into thrombus by use of hydrodynamic pressures following the laser-induced bubble expansion and collapse. The bubbles were formed at the fiber tip due to the absorption of laser energy by the surrounding absorbing liquids. The spatial distribution of photomechanically delivered drug depended on parameters such as laser energy, absorption coefficient, fiber size, and material strength. The results of Chapter 5 also showed that the bubble formation on the thrombus surface due to the

absorption of laser energy by the thrombus could cause flow motion near the cavitation bubble at a speed of up to 12 m/s. I hypothesize that hydrodynamic flow resulting from the bubble formation during laser thrombolysis can be used as a driving force to facilitate drug delivery.

My objective in this *in vitro* study was twofold. First, I wished to quantitatively compare the effectiveness of thrombolysis by use of 1) constant infusion of drug; 2) laser thrombolysis, and 3) photomechanical drug delivery. Such a comparison is important to clearly establish any benefit that may be associated with photomechanical drug delivery. Second, I wished to identify the mechanism of photomechanical drug delivery during laser thrombolysis through visualization of bubble formation with flash photography and measurement of laser-induced pressure waves using a PVDF transducer. Solutions of fluorescent spheres were used as a drug model that allowed me to easily visualize the sphere distribution in thrombus under fluorescence microscopy. Gelatin-based thrombus phantoms were used to avoid the complicated biological variations of real thrombus.

7.2 Materials and Methods

7.2.1 Sample Preparation

Two types of gelatin targets were formed in 1 cm cuvettes. Drug delivery experiments used a uniformly absorbing gelatin made by adding Blue 15 dyes into liquid gelatin (3.5% 175 bloom) and curing in the 1 cm cuvettes. The blue gelatin samples had an absorption coefficient of 100 cm^{-1} at 577 nm. The cured gelatin samples were carefully removed from the cuvette and cut into ~5 mm thick

sections before the experiments. The samples for flash photography were made by pouring clear gelatin into 1 cm cuvettes to form 2–3 cm thick with cylindrical geometries. The channels were constructed about 2 mm in diameter to simulate blood vessels; the normal adult human artery is 2–4 mm in diameter. A piece of porcine clot was inserted into the channel and then was covered with distilled water at room temperature.

The solution seeded with fluorescent latex microspheres (Molecular Probes, Inc.) was used as a drug model. The microspheres consisted primarily of polystyrene chains, and were supplied as suspensions (2% solids with 1 μm diameter) in water plus 2 mM sodium azid. They were nonporous, hydrophobic, and photostable. The excitation and emission maxima were at 488 nm and 515 nm respectively. The concentration of the solution was about 7.5×10^{7}particles/ mL made by adding 0.5 mL of the suspensions with a concentration of 3×10^{10}particles/ mL into 200 mL of distilled water. No attempt was made to correlate to any specific drugs for this study.

7.2.2 Experiments

The effectiveness of thrombolysis was evaluated by comparing the sizes of lumen created by mechanical action due to manual manipulation of a fiber-optic flushing catheter or by laser ablation, and the areas stained by the fluorescent spheres. A basic assumption of this study was that the stained areas could potentially be dissolved by the delivered drug. Three experimental protocols were performed. First, drug was infused into thrombus through a fiber-optic flushing

catheter that was manually manipulated inside the thrombus during infusion of the drug. Second, drug was infused into the laser-created channel after laser thrombolysis. Finally, drug was delivered into the thrombus in coincidence with laser pulses. The drug was injected at a rate of 4 mL/min through the catheter for a similar time (∼30 seconds) in the three experiments. All samples were carefully washed with clear water before being frozen and sectioned. Frozen sections were examined under light and fluorescence microscopy. The areas and penetration of the spheres in the gelatins were measured. The penetration depth was measured from the edge of the lumen to the fluorescent spheres inside the gelatin sample.

A fiber-optic flushing catheter was used for drug delivery and light delivery. This catheter consisted of a 1 mm Teflon tube filled with a 300 μm optical fiber. The drug was infused into the thrombus through the tube connected with a syringe. The flow rate was 4 mL/min controlled by a syringe pump. Laser radiation was provided by a 1 μs pulsed dye laser emitting 577 nm light at 3 Hz. The laser pulses of 30–70 mJ were delivered via the flushing catheter onto the thrombus under clear liquids.

The laser interaction with porcine clot was visualized with a flash photography setup (Figure 7.1). Single pulses of 50 mJ were delivered onto porcine clot through a 300 μm fiber placed 1 mm above the surface of the clot. The laser-induced pressure waves were measured using a PVDF transducer (Figure 7.2). The transducer was positioned 16 mm away from the ablation site. The experiments were performed on thrombus phantoms with an absorption coefficient of

$100\,\mathrm{cm}^{-1}$ at 577 nm. The samples were immersed under water at room temperature.

7.2.3 Statistical Analysis

All data were reported as mean±standard deviation. The differences in the lumen size, stained areas, and penetration depth of the spheres in gelatin samples were compared. The statistical significance of differences was determined using a two-tailed Student's t-test. An unpaired t-test was used to analyze the data for constant infusion, laser thrombolysis, and photomechanical drug delivery. A value of $p < 0.05$ was considered to be significant.

7.3 Results

The sizes of lumen generated by mechanical manipulation catheter were smaller than those generated by laser ablation (Figure 7.3). The lumen areas (i.e., lumen area plus stained area) didn't increase significantly through drug delivery for either constant infusion or laser thrombolysis, while the areas increased after the photomechanical drug delivery procedure. The areas increased up to 25% by accounting the areas stained by the spheres as compared with the lumen generated by laser ablation alone.

The penetration measurements revealed that the maximal penetration was not correlated with the laser energy (Figure 7.4). When the laser energy increased greater than a value somewhere between 50–70 mJ the penetration depth decreased. However, the lumen sizes increased significantly with increasing the

laser energy (Figure 7.5). The pressure measurements also showed that the pressures increased as the laser energy increased (Figure 7.6) and the lumen sizes were proportional to the bubble expansion pressure (Figure 7.7).

Visualization of the interaction of a laser pulse with clot showed that a full size bubble was formed in the clot (Figure 7.8). The bubble dynamics on clots was similar to the dynamics on gelatin targets. Figure 7.9 shows the cavitation bubble growth and collapse produced by a 50 mJ laser pulse. The bright spot in the sixth frame was the flash of light from the strobe. The bubble expansion caused the dilation of the channel. The maximal dilation was reached after about 60 μs and amounted to 130% of the initial channel diameter. The subsequent bubble collapse induced an invagination of the channel wall. The minimal diameter was $\sim$ 88% of the initial value. No oscillation of the cavitation bubble was observed. The mass ejection followed the bubble collapse.

7.4 Discussion

Results presented in this study demonstrated the possibility of using photomechanical drug delivery to enhance the thrombolysis process by delivering drug into thrombus during the laser thrombolysis procedure. Evidently, the lumen areas generated by the constant infusion due to mechanically manipulating the catheter were smaller than those created by the laser ablation. The lumen areas could be increased by delivering drug into the thrombus during laser ablation. For example, the mean of fluorescent sphere area and the maximal penetration depth were greater in the gelatin samples with photomechanical drug

delivery: $0.24\pm.05\,\text{mm}^2$ for photomechanical drug delivery vs. $0.06\pm0.01\,\text{mm}^2$ ($p = 0.005$) for laser thrombolysis and $250\pm63\,\mu$m for photomechanical drug delivery vs. $46\pm16\,\mu$m ($p < 0.001$) for laser thrombolysis. A similar result was reported by Girsky *et al.* [125] for photomechanical drug delivery to porcine clot confined in carotid arteries. Similar parameters such as the laser energy, fiber size, and fluorescent microsphere solution were used for their experiments. The mean of fluorescent sphere area was: $0.13\pm.02\,\text{mm}^2$ for photomechanical drug delivery vs. $0.02\pm0.004\,\text{mm}^2$ ($p = 0.01$) for laser thrombolysis. The maximal penetration depth was $327\pm36\,\mu$m for photomechanical drug delivery vs. $164\pm20\,\mu$m ($p = 0.002$) for laser thrombolysis.

Flash photographs showed that cavitation bubbles were formed after the laser pulses interacted with the clot. The cavitation growth and collapse caused dilation and consequent invagination of the channel wall of the gelatin samples. The flow motion may generate the hydrodynamic pressure that could force drug into the thrombus. The thrombus ejection was observed following the collapse of the cavitation bubble.

The penetration depth of the spheres in gelatin samples was not correlated with the laser energy. The penetration increased at least before the laser energy reached 50 mJ, and started deceasing somewhere between 50–70 mJ. It seems there is a threshold effect. I hypothesize that the laser-induced pressure is not enough to blow off the material surrounding the cavitation bubble when the laser energies below a certain value (called threshold energy). However, at high energy the ablation process becomes more explosive, resulting in strong pressure waves

that blow off the material deeply. The drug is also driven more deeply at high energy if the penetration depth is measured from the center of the lumen rather than from the channel wall to the spheres. The experimental results showed that the lumen areas were correlated with the bubble expansion pressure, which agrees with the ablation efficiency study in Chapter 8.

The results of this chapter and Chapter 6 demonstrated that drug can be delivered into thrombus and arterial tissue using photomechanical drug delivery. The laser pulses were delivered through optical fibers with 300–1000 μm core diameters. However, no experiments were performed using a 100 μm fiber that may be suitable for light delivery to brain vessels and no study has been reported in literature. The interest of using small fibers for light delivery has arisen recently for stroke treatment, since one of the main challenges for performing laser thrombolysis in a cerebral vessel is the design of a delivery device small enough to safely negotiate the cerebral vessel.

Thus, I visualized the bubble formation on gelatin samples (3.5% 175 gelatin containing Direct Red 81 dye, 150 cm^{-1}). A 100 μm core diameter step-index quartz optical fiber was coupled to the laser with a 25 mm focal length lens. The fiber was contained inside a 1 mm flexible Teflon tube and the tip was 1 mm inside the catheter. The laser was operated at 520 nm with a repetition rate of 3 Hz. 90 pulses of 10 mJ were delivered onto the gelatin. The sample preparation was describe in detail in Chapter 4. The procedure of photomechanical drug delivery was the same as the above experiments of photomechanical drug delivery.

Figure 7.10 shows the flash photographs of cavitation bubble formation on

gelatin surface. The maximum size bubble (∼1.5 mm in width) was observed at 50 μs. The bubble expanded, collapsed, and the ejection of material from the surface was observed following the bubble collapse about 195 μs after the laser pulse. Photomechanical drug delivery did not significantly increase the lumen area by delivering drug using a 100 μm fiber at 10 mJ laser energy (Figure 7.5). However, transient displacement of the surrounding fluid may benefit the thrombolysis process. A study by Kandarpa *et al.* suggested that forceful local pulsatile infusion of fibrinolytic enzyme disrupts thrombi, increases clot surface area, and hastens enzyme action compared conventional constant infusion methods [126]. They used a reciprocating syringe pump to deliver small volumes of thrombolytic enzyme in short, rapid, frequent pulses at high exit-jet velocity (4.5 m/s) through a 4-F side-hole catheter. Pulsatile infusion lysed 61% of the thrombus by weight in an hour, whereas constant infusion lysed only 15%. The cavitation bubble expansion and collapse caused the surrounding fluid to move up to 12 m/s. A better result may be achieved using photomechanical drug delivery.

In conclusion this study demonstrated the thrombolysis process can be enhanced by delivering drug into thrombus during laser ablation. The lumen areas increased up to 25% if we consider the areas that may potentially be dissolved by the drugs. The penetration depths of the spheres in the gelatin samples were not correlated with the laser energy, but the lumen sizes increased with increasing laser energy. The lumen areas created by laser ablation were correlated with the bubble expansion pressures, and the pressures were proportional to the laser energy. Photomechanical drug delivery can be performed using a 100 μm fiber.

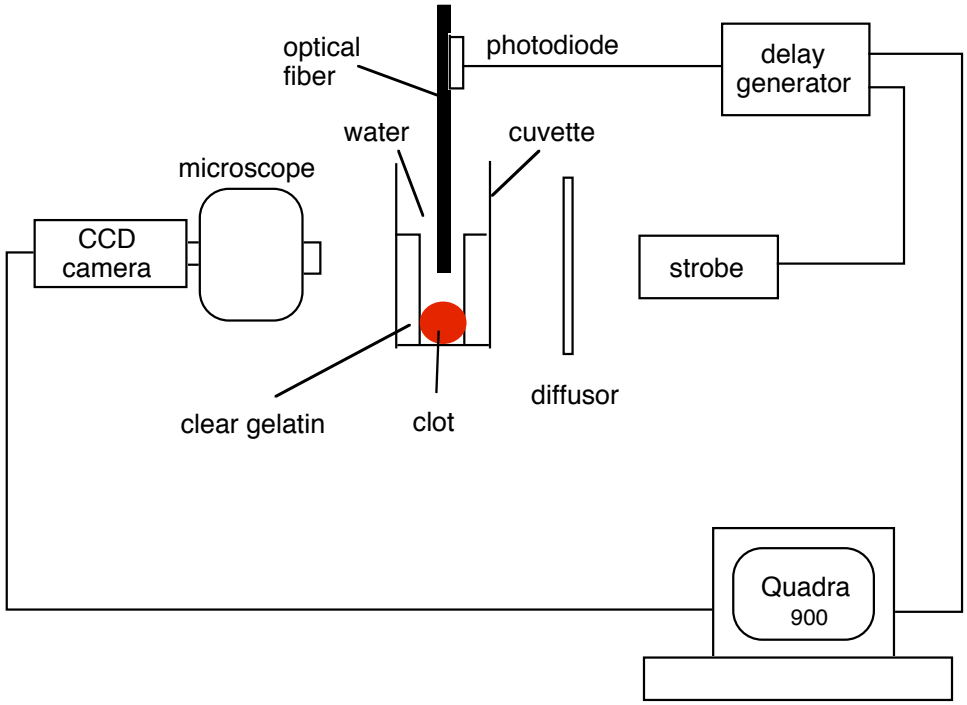

Figure 7.1: Schematic of experimental setup for visualizing the bubble formation on clot or gelatin.

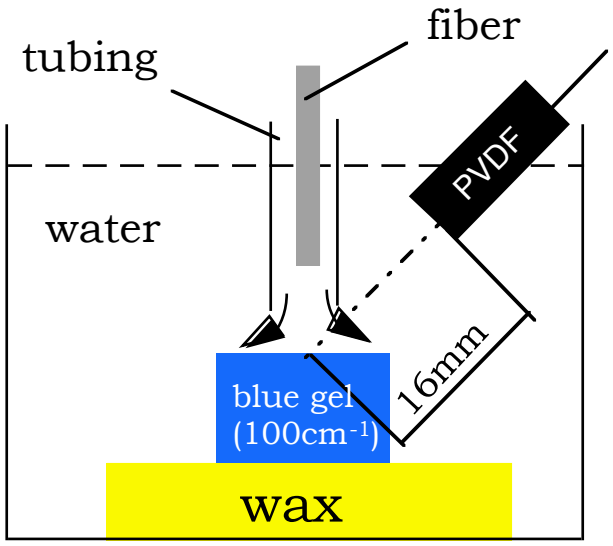

Figure 7.2: Schematic of apparatus for pressure measurement.

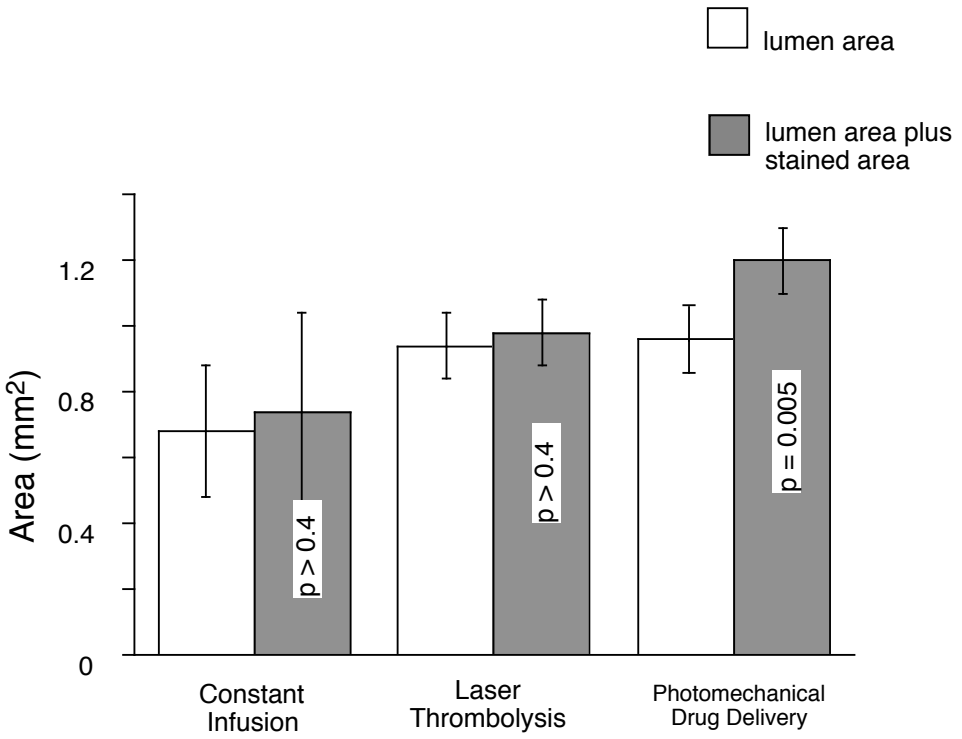

Figure 7.3: Comparison of lumen areas generated by three different methods: constant infusion, laser thrombolysis, and photomechanical drug delivery. 90 laser pulses of 50 mJ were delivered into gelatin samples with an absorption coefficient of 100 cm^{-1} for both laser thrombolysis and photomechanical drug delivery experiments. A flushing catheter with a 300 μm fiber was used for the light delivery.

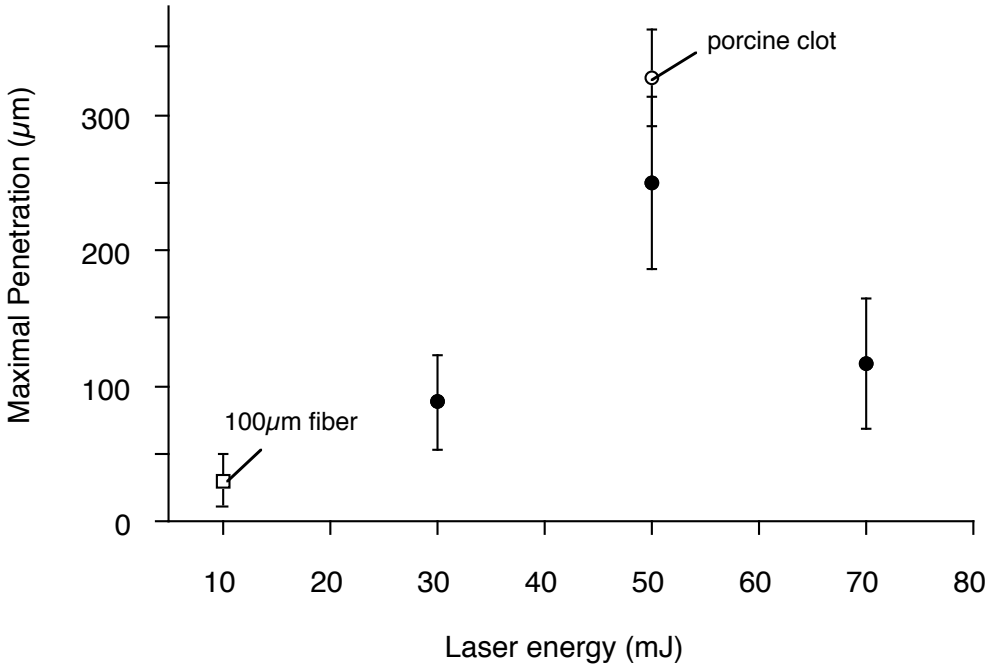

Figure 7.4: Maximal penetration of fluorescent spheres inside gelatin samples as a function of laser energy. The laser pulses were delivered via a flushing catheter with a 300 μm fiber. Error bars denote the standard deviation of four samples. The penetration of the fluorescent spheres inside porcine clots was measured by Girsky *et al.* .

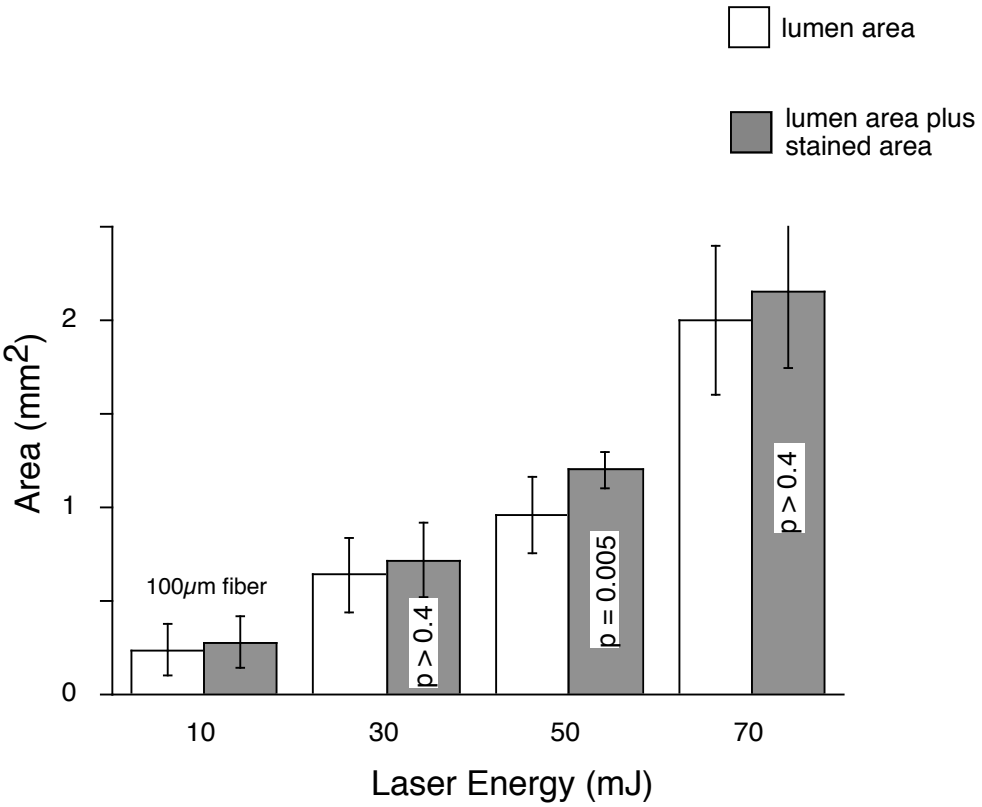

Figure 7.5: Areas including lumen areas created by laser ablation and stained areas due to the drug delivery as a function of laser energy. 90 laser pulses were delivered via a flushing catheter with a 300 μm fiber onto the gelatin samples with an absorption coefficient of 100 cm^{-1}. Error bars present the standard deviation of four samples.

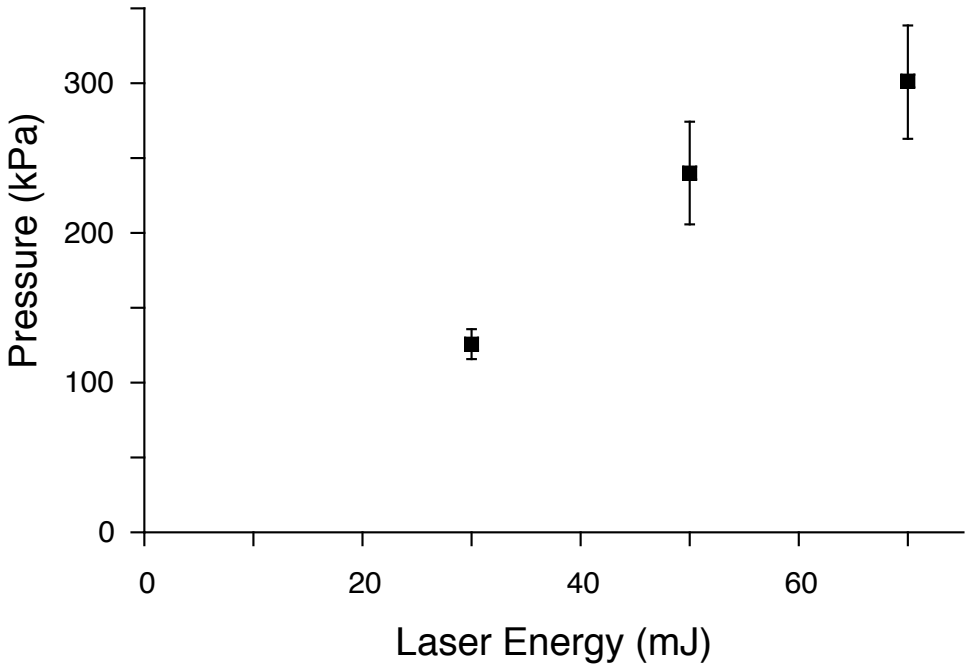

Figure 7.6: Bubble expansion pressure as a function of laser energy. The pressure signals were detected with a PVDF transducer placed 16 mm away from the ablation site under water. The absorbing gelatin samples had an absorption coefficient of $100\,\mathrm{cm}^{-1}$.

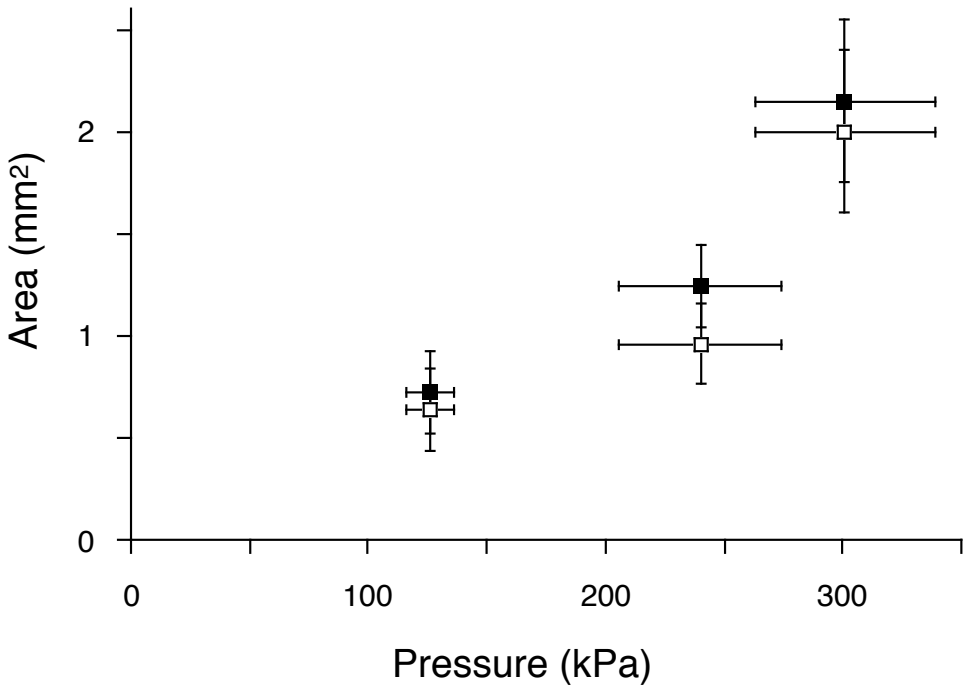

Figure 7.7: The areas produced by laser ablation (open squares) and drug delivery (filled squares) as a function of bubble expansion pressure on gelatin samples (Figure 7.6).

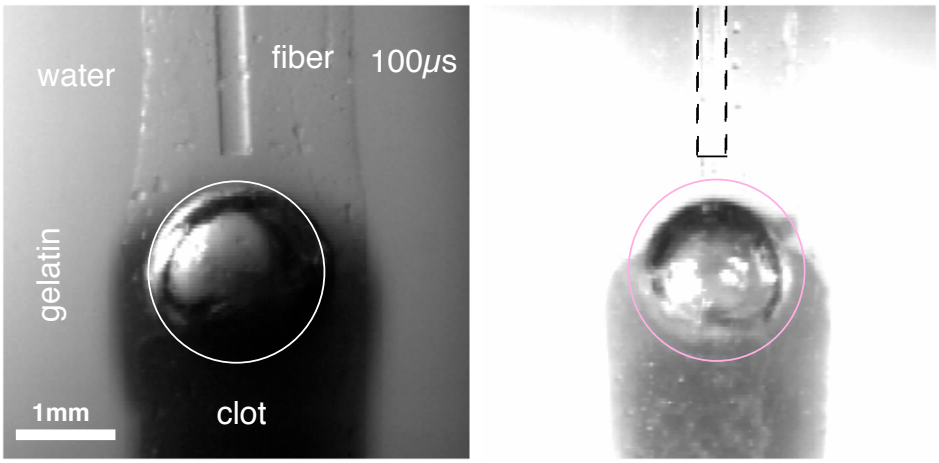

Figure 7.8: A laser-induced cavitation bubble formed in the clot. The right photo was taken to show the spherical shape of the bubble on the left.

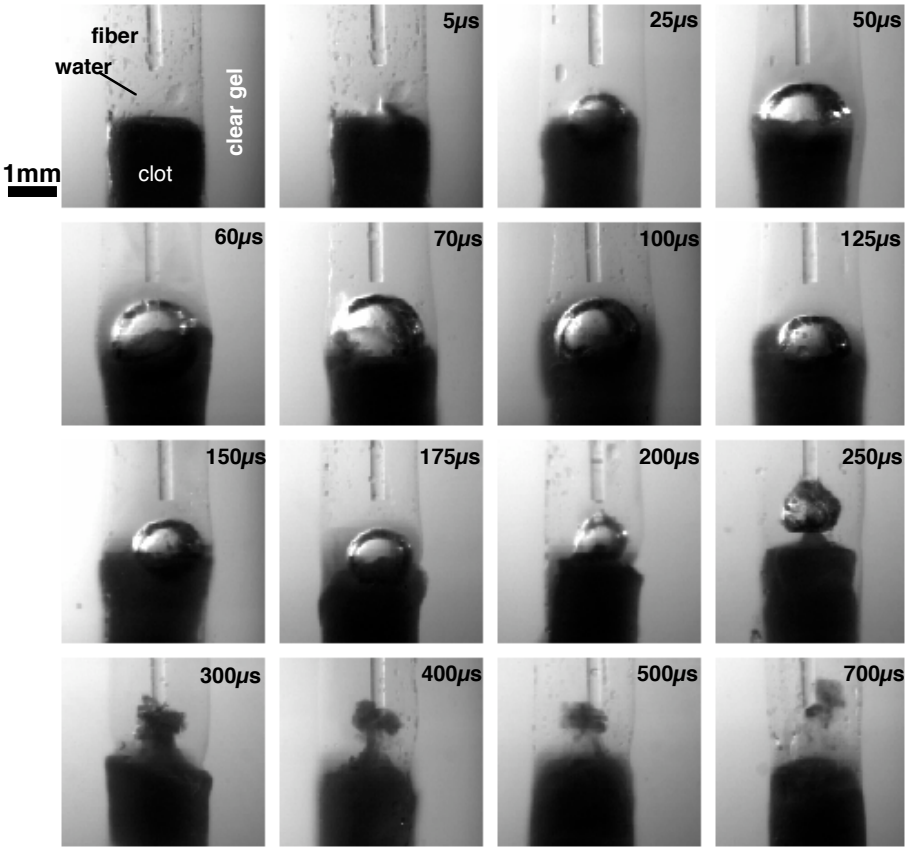

Figure 7.9: A series of flash photographs of cavitation bubble growth and collapse after the laser pulse. Single pulses of 50 mJ were delivered onto the clot via a 300 μm fiber. The clot was confined in a gelatin sample with a cylindrical channel at center. The fiber was placed 1 mm above the clot under water.

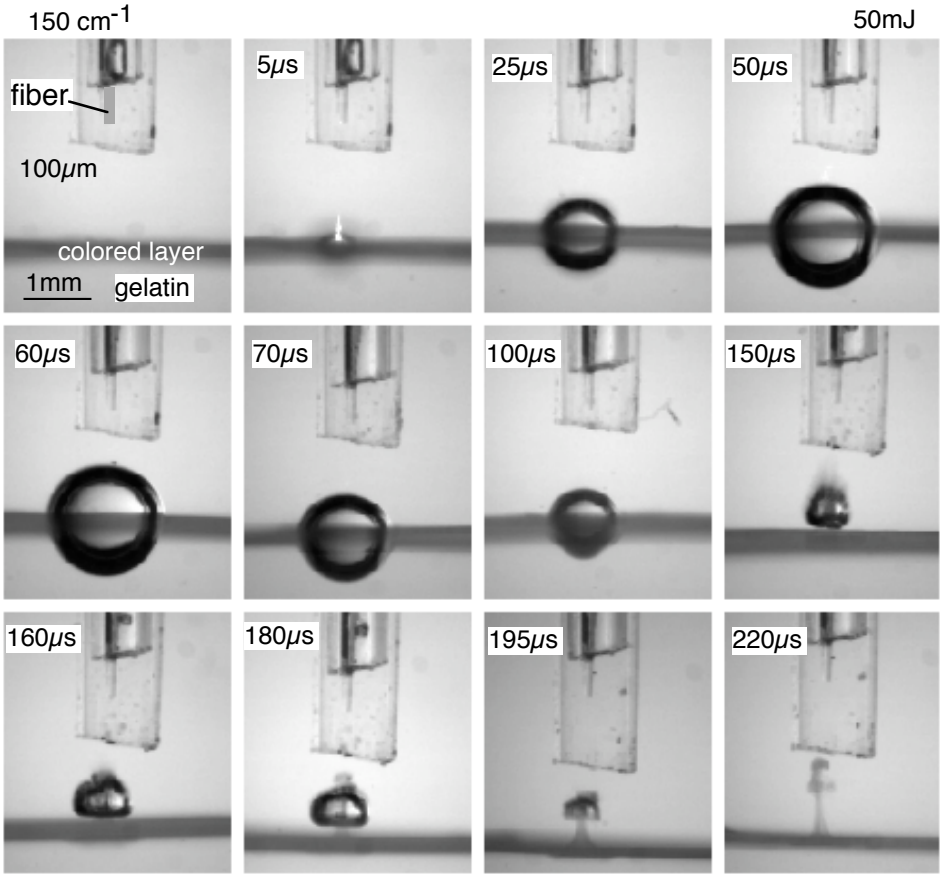

Figure 7.10: Flash photographs of bubble formation on gelatin surface.

Chapter 8

Microsecond Laser Ablation of Thrombus and Gelatin under Clear Liquids: Contact vs Non-contact

8.1 Introduction

Laser thrombolysis is a promising method for management of vessels blocked by thrombus such as occurs during acute myocardial infarction and stroke [1]. Laser thrombolysis uses laser pulses to clear arteries obstructed by thrombus (blood clots). The laser pulses generate cavitation bubbles in a blood vessel through the absorption of laser energy by a target (e.g., blood clot) or surrounding liquids (e.g., blood and saline). The bubbles expand and collapse within a millisecond of the delivery of the laser pulse and disrupt the thrombus. Safety is achieved by using laser wavelengths that are relatively strongly absorbed by the blood clot as compared to absorption by the vessel wall [37–39].

During laser thrombolysis, the laser pulses are delivered to the blood clot using an optical fiber whose tip either contacts or does not contact the clot. The contact method has been used with excimer lasers (308 nm) and mid-infrared lasers (2.1 μm) [106, 107]. Ablation occurs at the tip during such procedures. If a fluid-core optical catheter is used to wash away ambient blood, then visible wavelength laser pulses can ablate the clot in a non-contact manner [55].

Previous studies have demonstrated that the ablation processes are quite different for contact and non-contact methods [127–131]. Srinivasan *et al.* demonstrated that contact excimer laser ablation of plaque was more violent than non-contact ablation when the same energy was used [127]. Gijsbers *et al.* reported a dramatic increase in ablation efficiency when the optical fiber contacted porcine aortic tissue [128], and that the ablation depth increased with increasing force between the fiber face and the tissue [131]. Similar results have also been reported by Buchelt *et al.* [130]. No detailed study of contact and non-contact delivery on the ablation efficiency has been reported, although many studies have demonstrated that ablation efficiency depends on pulse energy [32, 39], radiant exposure [130, 132, 133], pulse duration [133], properties of the tissue [85], repetition rate [134], and fiber contact pressure [128, 130, 131].

It is difficult to precisely position the fiber-optic catheter *in vivo*, and this study investigated the consequences of inadvertent contact of the fiber with the thrombus. When the fiber does not contact the thrombus, the radiant exposure depends on the distance between the thrombus surface and the fiber end due to the divergence of the laser beam. The laser energy may also be attenuated by the

absorption of the surrounding medium. These effects are eliminated when the fiber end contacts the thrombus surface. Since contact ablation is more efficient than non-contact ablation, I measured the pulse energies required to achieve the same material removal for the two modalities.

I measured the ablation efficiency of one microsecond 577 nm laser pulses on porcine clot confined in a silicone tube. Laser energies ranging from 10–75 mJ were delivered through 200–400 μm optical fibers. The ablated mass was determined by weighing the samples before and after ablation. I visualized the bubble formation with flash photography and measured acoustic transients with a pressure transducer. These experiments were performed on gelatin-based thrombus models. The use of these thrombus models provided a reproducible substrate for modeling thrombus ablation. Finally, I also evaluated contact and non-contact methods for localized drug delivery.

8.2 Materials and Methods

8.2.1 Sample Preparation

Porcine Clot

Fresh non-heparinized blood was obtained from domestic swine and immediately placed into cylindrical glass tubes. The blood was allowed to clot at room temperature for 5 hours and then stored at 8°C for 24 hours. The durability of the clot varied from pig to pig; more white fibrin pieces were found in the most durable samples. The clots were cut into pieces ~10 mm long, ~2 mm wide, and

$\sim$2 mm thick. They were weighed using a digital balance with a precision of $\pm 100\,\mu$g (AE200, Mettler) and then confined in a silicone tube. The tube had a 3 mm inner diameter and a wall thickness of 0.4 mm. The mechanical properties differed from those of human arteries; the Young's modulus of the silicone tube was 8 N/mm^2, whereas it is 2–5 N/mm^2 for human vessels [135]. The clot samples from three different pigs were ablated to assess the intra-animal variation of clot on the ablation efficiency.

Gelatin Targets

A thrombus model consisted of 3.5% 175 bloom gelatin (Sigma). The percentage was determined by the weight ratio of gelatin to water. The bloom number is the standard method for indicating the toughness of gelatins and is a measure of surface tension. Higher bloom numbers indicate stronger gelatins. No attempt was made to correlate the bloom number with the strength of any specific clots in this study. The gelatin-water mixture was heated to 60°C with stirring until it became clear. Two types of gelatin targets were formed in 1 cm cuvettes. Flash photography used a clear gelatin substrate covered by a thin layer of absorbing gelatin. These were made by pouring clear gelatin liquid gelatin in 1 cm cuvettes and curing to form 2–3 cm thick targets with flat surfaces. A dye solution (0.07 g of Blue 15 from Sigma in 40 mL water) was placed on the gelatin surface for 5 minutes and a blue layer about 300 μm thick with an absorption coefficient of $\sim$100 cm^{-1} (at 577 nm) was formed. This blue layer allowed the boundaries of the cavitation bubble to be seen, even when they otherwise would have been

hidden by a light absorbing gelatin substrate (Figure 8.1). Both the pressure measurements and the drug delivery experiments used a uniformly absorbing gelatin target made by adding 0.07 g of Blue 15 to 40 mL of liquid gelatin and curing. The 100 cm^{-1} blue gelatins were carefully removed from the cuvettes and cut into ∼5 mm thick sections before the experiments.

8.2.2 Laser Delivery

All experiments used a flashlamp-pumped dye laser (Palomar Medical Technologies) operating at 577 nm. The pulse duration was 1.3 μs (full width at half maximum). The laser energy was determined using a joulemeter (Molectron). Contact experiments used 10–25 mJ/pulse; non-contact experiments used three times as much. Pulse-to-pulse energy variation was less than 5%. The repetition rate was 3 Hz for the ablation efficiency measurements. The laser pulses were delivered through a flushing catheter that consisted of a single 200–400 μm step-index fused-silica optical fiber contained inside a 1 mm flexible Teflon tube. The fiber tip extended 1 mm from the distal end of the catheter during contact delivery; the tip was 1 mm inside the catheter during non-contact delivery (see Figure 8.1). Distilled water or normal saline was injected through the Teflon tube with a syringe infusion pump (Harvard Apparatus) at a flow rate of 4 mL/min to wash away the removed clot or gelatin from the target site. The fiber tip always slightly contacted the targets (clot or gelatin) during contact delivery and was 2 mm from the target surfaces during non-contact delivery. The spot size on the target surface was obtained from the burn pattern on a deep-dyed polyester film.

The spot sizes were 200, 300, and 400 μm for contact ablation and 450, 480, and 520 μm for non-contact ablation. The laser beam profile on the target was nearly Gaussian for non-contact ablation, and had a flat profile for contact ablation. The laser energy and spot sizes used in this study are summarized in Table 8.1.

8.2.3 Ablation Efficiency Measurement

The experimental setup for the ablation efficiency measurement is shown in Figure 8.2. The ablation efficiency is the mass ablated per pulse per unit-of-laser-energy delivered. The ablated mass was determined by directly weighing the samples before and after ablation. Primary experimental results showed that a similar amount of clot could be removed using a 300 μm fiber either at 20 mJ during contact ablation or at 60 mJ during non-contact ablation. Consequently the non-contact experiments used three times the pulse energy that the contact experiments used. The pulse number varied from 180–395 depending on the removed mass that could be easily measured. The catheter was advanced manually during the procedure and five samples were ablated for each measurement. Non-laser controls were exposed to flowing water or saline for about 2 minutes without irradiating, so that the mass lost due to the flowing fluid and the mass loss caused by mechanical manipulation could be assessed.

8.2.4 Flash Photography

Vapor bubble formation was visualized using flash photography (Figure 8.1). Time zero corresponded to the rising edge of the signal from a photodiode attached to the laser delivery fiber. A digital delay generator (DG535, Stanford Research) was used to turn on a 5 μs strobe (MVS-2601, EG&G) at times ranging from 5–20,000 μs after the laser pulse. A triggerable CCD camera (CV-251, Protec) only recorded events illuminated by the strobe. The CCD image was captured with a video frame grabber (DT2255, Data Translation). Each picture recorded a single event and was repeated three times for each experiment. Single pulses of 20 mJ laser energy were delivered through a flushing catheter with a 300 μm diameter fiber for contact ablation. Non-contact ablation used 60 mJ laser pulses and the same fiber size.

8.2.5 Pressure Measurements

The pressure transients were measured with a piezoelectric polyvinlyidene-fluoride (PVDF) transducer (KP 117, Ktech). The active square area of the transducer was 1 mm ^{2}. The sensitivity was $\sim$32 mV/bar and the rise time was $\sim$400 ns. The transducer was factory calibrated in air to give absolute pressure amplitudes. However, the absolute pressures may be underestimated because the transducer was calibrated in air, but used in an aqueous environment. The acoustic signals were recorded on a digital storage oscilloscope (DSA 602A, Tektronix). The transducer was placed at a distance of $\sim$16 mm from the target site under distilled water. The 1 mm flushing catheter with a 300 μm fiber was placed in a

container filled with distilled water. The flow rate was 4 mL/min. Single pulses of 10–25 mJ were delivered onto the gelatin via a flushing catheter with a 300 μm fiber for contact ablation, and 30–75 mJ laser pulses were used for non-contact ablation.

8.2.6 Drug Delivery

Drug delivery using contact and non-contact methods was evaluated using 100 cm^{-1} gelatin targets. The gelatin samples were placed under distilled water at room temperature. A flushing catheter with a 300 μm fiber was used to deliver about 90 pulses with laser energies of 20 mJ (contact) and 50 mJ (non-contact) at 3 Hz perpendicularly onto the gelatins. The catheter was advanced by hand as a channel was ablated through the gelatin. A 7.5×10^7spheres/mL solution of 1 μm fluorescence spheres (Molecular Probes, Inc.) was infused at 4 mL/min during the ablation. The control samples were first ablated while water alone was infused at 4 mL/min. After a channel was created the control samples were infused with the sphere solution for about 30 seconds. The number of laser pulses delivered were 95±3 for contact and 93±4 for non-contact. All samples were carefully washed with clear water before being frozen and sectioned. Each frozen sample was cut into 4 or 5 sections with a thickness less than 100 μm. Frozen sections were examined under light and fluorescence microscopy. The penetration of the spheres in the gelatins was measured.

8.2.7 Statistical Analysis

All data is reported as mean±standard deviation. The statistical significance of differences was determined using a two-tailed Student's t-test. An unpaired t-test was used to analyze the data as each parameter was varied. A value of $p < 0.05$ was considered to be significant.

8.3 Results

8.3.1 Ablation Efficiency of Porcine Clot

During ablation of the clot, a popping sound accompanied each laser pulse, and a stream of red liquid erupted along with some small particulates. The particulate size was correlated with white fibrin found in the clot. Smaller particulates were associated with more fibrin pieces. The number of fibrin chunks and the mechanical strength of the clots varied from pig to pig. Less mass was removed from the most durable clots. The rate of thrombus removal slowed as the clot became less red (presumably due to hemolysis and loss of hemoglobin). Smoke could be smelled at the highest laser energies ($\geq 60\,\mathrm{mJ}$) during non-contact delivery. The ablation efficiency (mass removed per unit energy) of contact ablation was at least three times greater than that of non-contact ablation (Figure 8.3). There were no significant differences in the ablation efficiency at different spot sizes for either contact ablation or for non-contact ablation. Intra-animal variation significantly affected the ablation efficiency (Table 8.2). No significant difference in the ablation efficiency of porcine clot under distilled water or normal saline was

observed despite the fact that water can cause hemolysis.

8.3.2 Bubbles Evolution

Time-resolved flash photographs revealed that a laser pulse generated a cavitation bubble either at the fiber end or on the gelatin surface depending on where the laser energy was absorbed. Each picture was a single event and was repeated three times for each parameter set. The bubble size was reproducible to 5% before the bubble collapse. The appearance of cavitation bubbles varied widely after the bubble collapse.

Figure 8.4 shows a compilation of the bubble expansion and collapse sequence in water for contact ablation. The maximum width of the bubble was $\sim$2.8 mm and was reached at 75 μs. The bubble completely collapsed 250 μs after the laser pulse. Significant mass removal was observed at 275 μs and at 700 μs respectively. Figure 8.5 shows the bubble evolution in water for non-contact ablation. The maximum width of the bubble measured 3.6 mm at 95 μs. The bubble completely collapsed about 300 μs after the laser pulse. Material removal lasted from 300–900 μs. Figure 8.6 shows the bubble width measured from Figures 8.4 and 8.5.

8.3.3 Bubble Pressure

A representative pressure trace for a laser pulse of 30 mJ delivered onto gelatin under water in non-contact ablation is shown in Figure 8.7. The initial pressure peak was due to a thermo-elastic expansion wave. The second peak at 300 μs was generated by the collapse of the cavitation bubble. The times were corrected to

account for the time delay associated with the time it takes the acoustic signal to propagate from the ablation site to the transducer. I assume that the pressure signals travelled at 1500 m/s. The results of the acoustic transient measurements are summarized in Figure 8.8. The pressure amplitudes of the bubble expansion and collapse were nearly equal for any particular experiment. Pressure was generated during the contact delivery at a rate of about 12 kPa/mJ and during non-contact delivery at 4 kPa/mJ.

8.3.4 Drug Delivery

The greatest penetration of fluorescence spheres in the gelatins was $247\pm57\,\mu$m for contact delivery and $250\pm63\,\mu$m for non-contact delivery. The number of the spheres in the gelatins was similar for both contact delivery and non-contact delivery under fluorescence microscopy.

8.4 Discussion

Contact and non-contact ablation are remarkably similar when visualized using high speed photography (Figures 8.4 and 8.5). A well-defined cavitation bubble is formed whether or not the fiber contacts the surface. The cavitation bubble grows and collapses; no secondary bubble is observed. Material removal follows the collapse of the bubble. When roughly equal size bubbles are formed, then the bubble lifetimes are also similar for contact and non-contact ablation.

Contact and non-contact ablation differs in a few ways. Non-contact ablation forms a cavitation bubble that is half inside the gelatin and half in the ambient

liquid; the contact bubble creates a bubble that is nearly entirely contained within the gelatin. The shape of the non-contact bubbles (at maximum size) is more spherical than contact ablation bubbles. Finally, there is some visual evidence that the contact ablation removes material at two discrete times after the collapse of the cavitation bubble.

Quantitative measurements of the material removed during ablation indicate that the ablation efficiency is profoundly affected by whether or not the optical fiber tip directly contacts the thrombus. Non-contact ablation needed roughly three times as much laser energy to remove the same amount of clot as contact ablation needed (Table 8.1). Similarly, the bubble expansion pressures were nearly equal when the non-contact laser energy was three times the contact laser energy. A similar result was not observed for the maximum bubble size. Non-contact ablation bubbles (at three times the energy) were larger than the contact bubbles.

The mass removed per unit energy (the ablation efficiency) was relatively constant for either contact or for non-contact ablation (Figure 8.3). However, the ablation efficiency varied significantly when clots from different animals were ablated (Table 8.2). Furthermore, even the least efficient ablation (2.4 μg/mJ) was significantly greater than would be expected from a simple vaporization argument. The heat of vaporization of water is about 2.5 kJ/gm and so ablation that is solely due to vaporization would remove clot at a rate of 0.4 μg/mJ of laser energy. Consequently, the ablation process must be accompanied by mechanical disruption of the clot [85]. This was confirmed by flash photography.

Somewhat surprisingly, the mass removed per pulse did not depend on the spot size for either contact or non-contact ablation. The spot size plays an important role in ablation at pulse energies near the threshold for ablation [136]. In our experiments the ablation threshold was about $15\,\mathrm{mJ/mm^2}$. Since the lowest radiant exposure was about $80\,\mathrm{mJ/mm^2}$ or more than five times the ablation threshold, I must conclude that spot size plays only a secondary role at pulse energies significantly above threshold. In other words, it is not where the energy is deposited, but rather how much energy is deposited that affects the mass removal process.

Typically, a channel could be easily created through clot during either contact or non-contact laser ablation. The residual clot on the walls of the vessel (mural thrombin) was not so easily removed and white fibrin chunks always remained. This mural fibrin residue could be a potent stimulus for rethrombosis *in vivo*. Consequently, I measured the ability of the 50 mJ non-contact ablation and 20 mJ contact ablation to drive microspheres (to simulate a thrombolytic drug) into clot. The microspheres penetrated the mural clot the same distance for both ablation methods, and this suggests that either method might be used for localized drug delivery to enhance the thrombolysis process.

The expansion pressures generated by contact delivery (on gelatin) were similar to those during non-contact delivery at three times the pulse energy (Figure 8.8). Moreover, for a given expansion pressure the contact bubbles were slightly smaller than the non-contact bubbles (Table 8.1). This is evidently a consequence of non-contact bubbles being able to grow more easily in the less viscous fluid over

the gelatin. Contact ablation achieved higher bubble expansion pressures for a given pulse energy due to the presence of the boundary of the fiber tip [137]. The fiber tip constrains the direction that the initial cavitation bubble can travel—it must initially grow away from the fiber tip. This is sometimes called constrained vaporization or tamping and has been extensively exploited for the ablation of kidney stones [98].

To summarize, material removal increased with increasing bubble size, increasing energy, and increasing pressure. Material removal did not change with spot size. When mass removal is plotted as a function of bubble size and pulse energy, two distinct groups of data result: one for contact and one for non-contact. However, when the mass ablated (for clot) is plotted as a function of the bubble expansion pressure (for gelatin) the data for both contact and non-contact ablation is grouped together much more closely (Figure 8.9). Consequently, I am led to the conclusion that the most important parameter in microsecond ablation of soft materials in an aqueous environment is the expansion bubble pressure. A similar observation was made by Tomaru *et al.* who showed a weak correlation between shockwaves and mass removal during contact pulsed-dye laser ablation of aortic tissue [51].

This study demonstrated that the contact ablation efficiency of porcine clot was at least three times greater than the non-contact ablation efficiency. Furthermore, the mass removed per unit laser energy was relatively constant for both laser energy and fiber size. The mass ablated was correlated with the expansion pressure of the cavitation bubble. This result provides an important piece

of information for designing clinical clot ablation systems: pressure is the most important factor in establishing the ablation efficiency of a one microsecond laser pulse. For example, since the mass removed per pulse is (roughly) linearly related to the bubble expansion pressure, ten small laser pulses will remove the same amount as one large pulse with ten times the energy. This is important because previous studies have demonstrated that cavitation bubbles can structurally deform vessel walls and possibly lead to damage of the vessel walls [88, 97]. Since larger bubbles generate greater pressures, a greater number of smaller bubbles may allow safer, more controlled, laser ablation of clot in arteries.

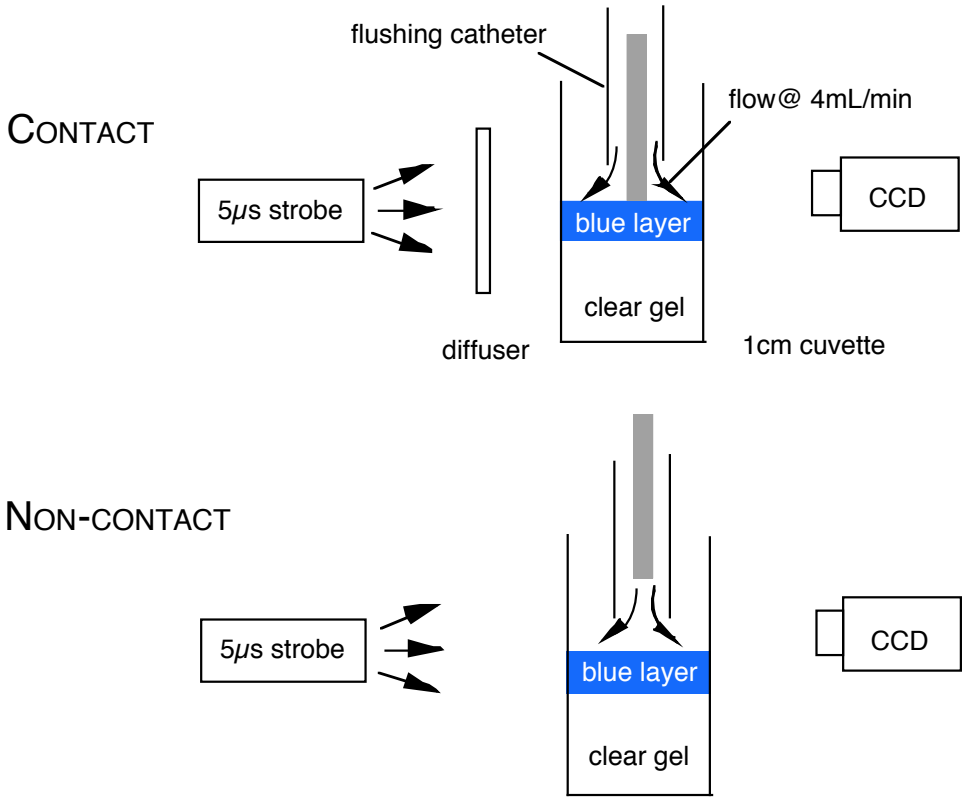

Figure 8.1: Experimental setup for the visualization of cavitation bubble formation. The blue layer was 300 μm thick and had an absorption coefficient of 100 cm^{-1}.

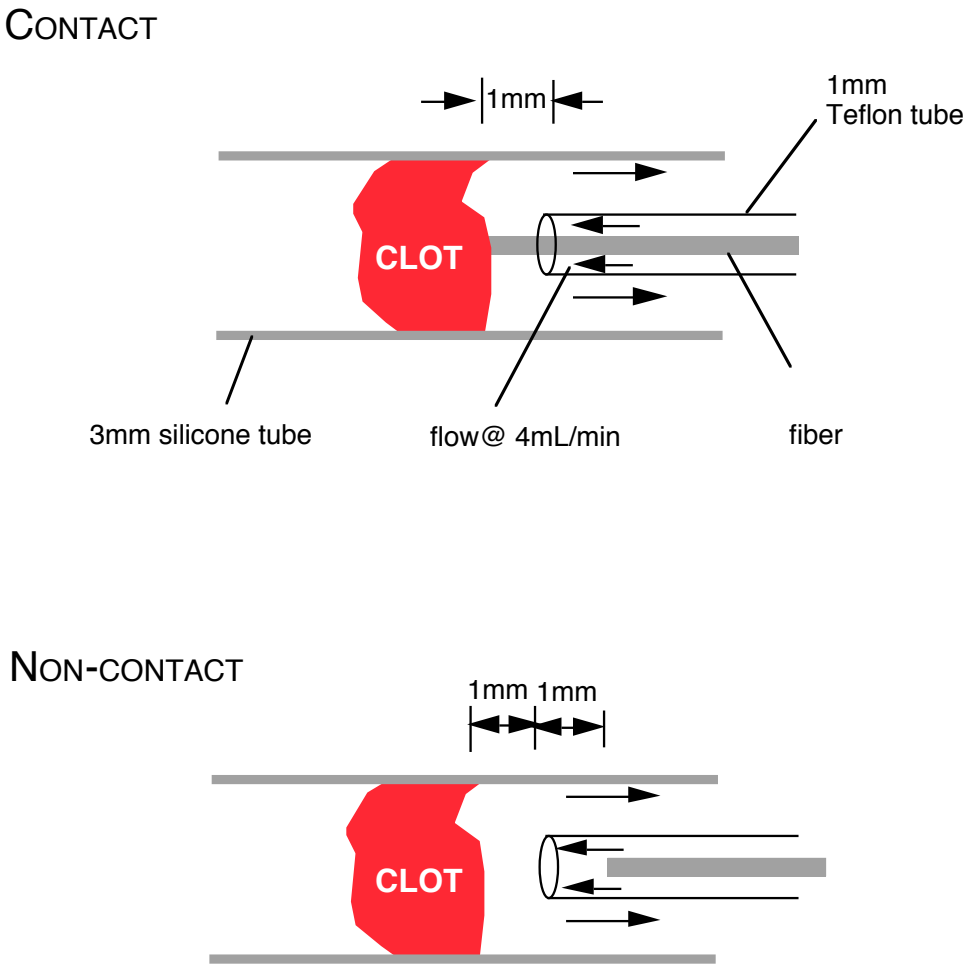

Figure 8.2: Schematic of contact and non-contact ablation experiment. In both cases clear fluid flows out of the catheter at 4 mL/min to wash debris away from the ablation site.

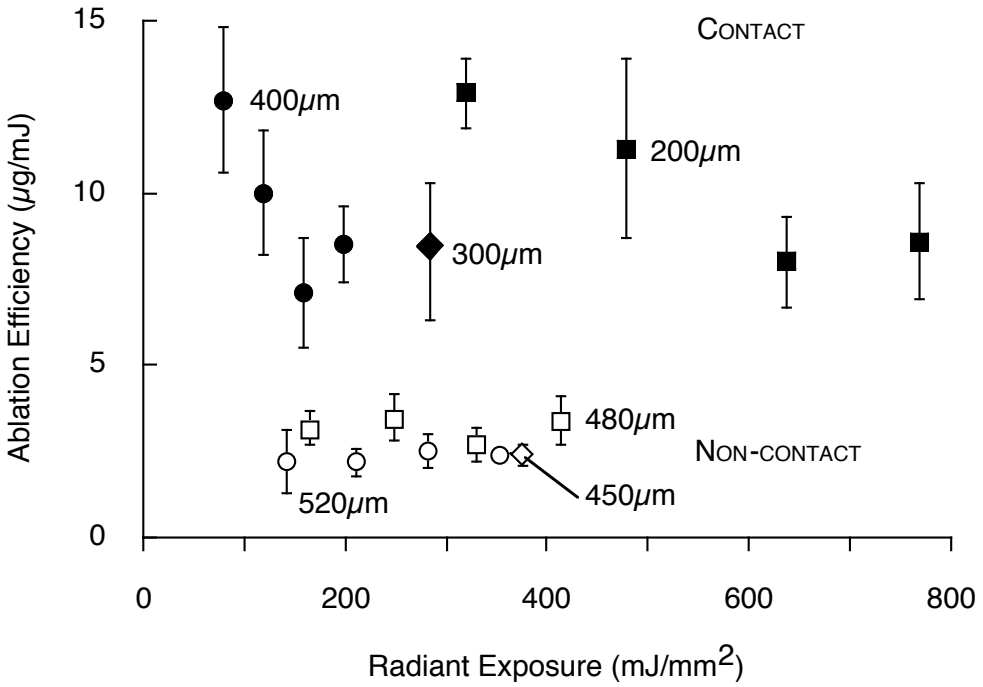

Figure 8.3: Ablation efficiency of 1 μs laser pulses on clots from Pig B in Table 2. The clot used was from a single pig. The filled markers are for contact ablation; non-contact ablation are presented with open markers. The laser spot sizes are labeled. All data are mean±standard deviation of five samples.

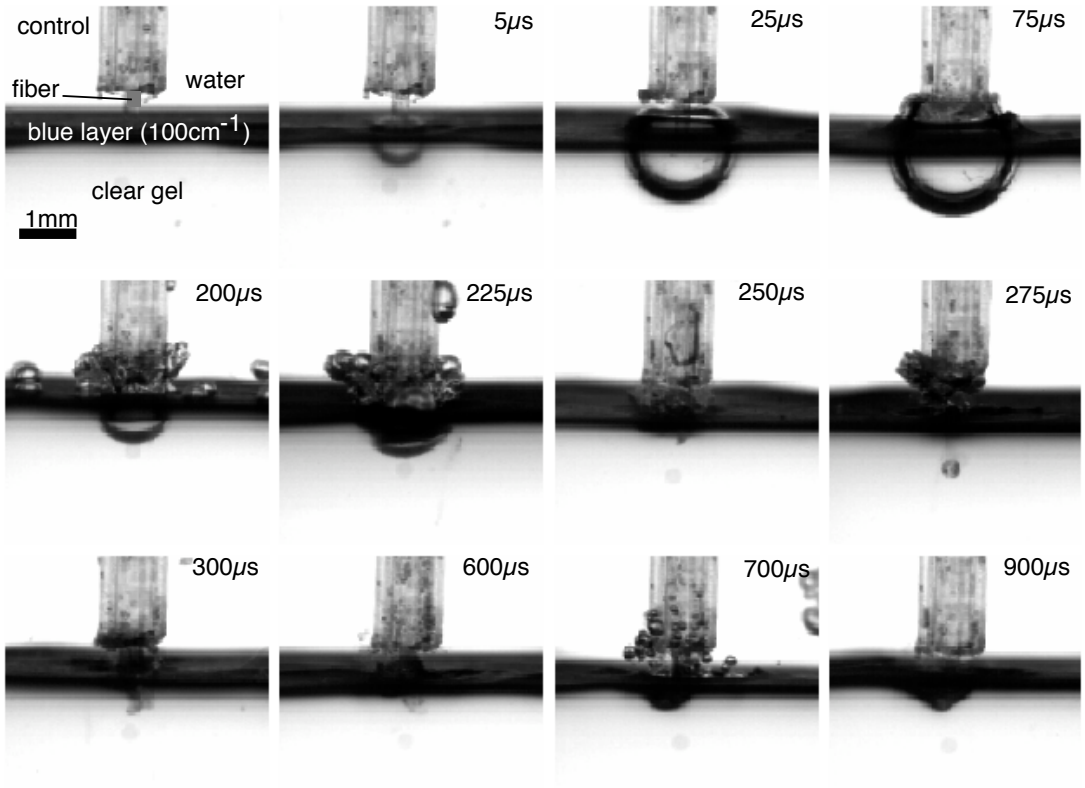

Figure 8.4: Bubble formation on gelatin when the optical fiber is in contact with the gelatin surface. The optical fiber is centered in a 1 cm cuvette. A single pulse of 20 mJ laser energy was delivered through a flushing catheter with a 300 μm diameter fiber. The colored layer was 300 μm thick, but appears thicker due to a slight curvature of the surface.

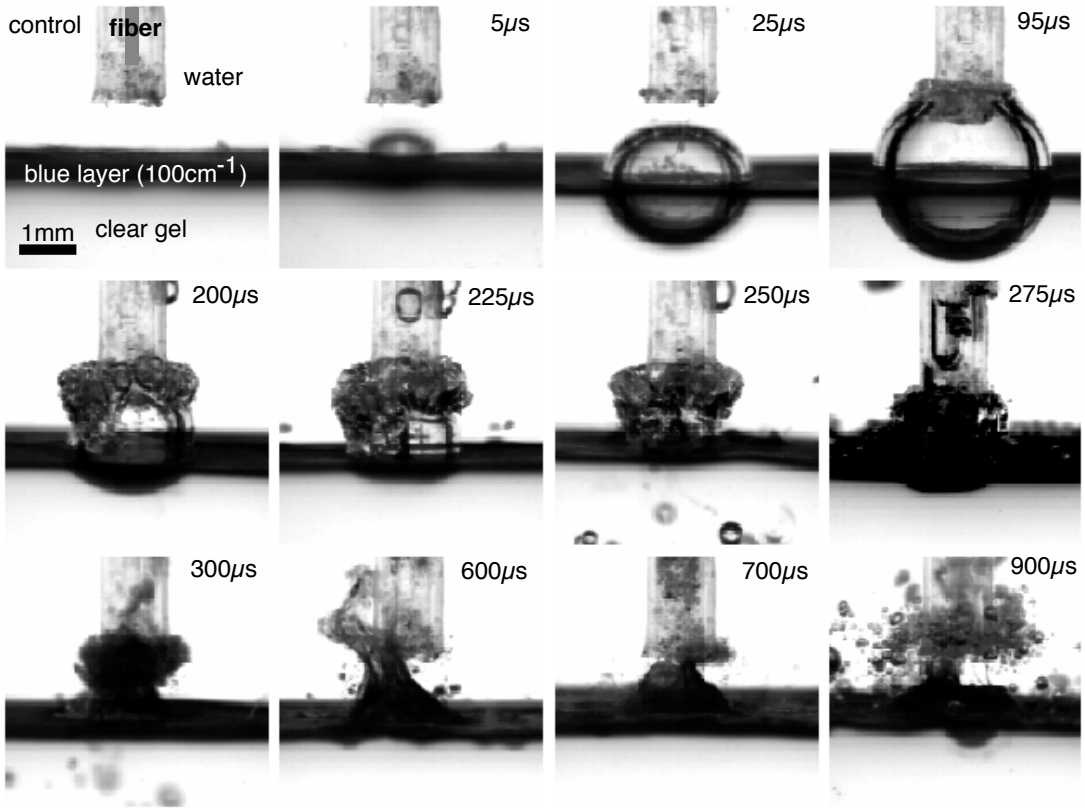

Figure 8.5: Bubble formation on gelatin when the optical fiber is 2 mm above the gelatin surface. The optical fiber is centered in a 1 cm cuvette. A single 60 mJ laser pulse was delivered through a flushing catheter with a 300 μm diameter fiber. The colored layer was 300 μm thick.

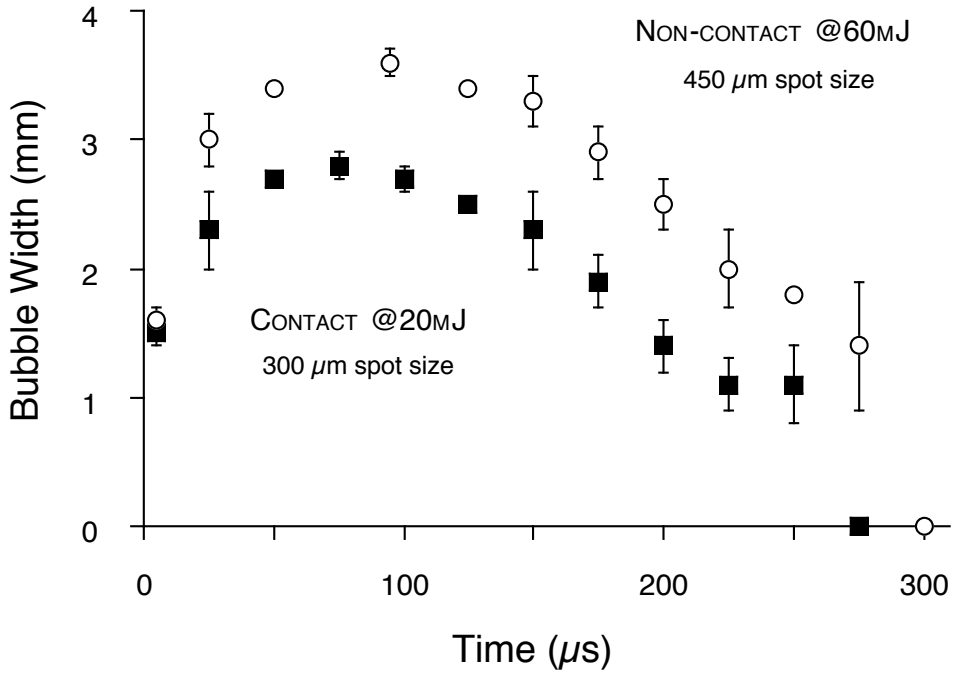

Figure 8.6: Bubble width as a function of time after the laser pulse for the contact and non-contact ablation, shown in Figures 8.4 and 8.5. Error bars represent the standard deviation of three measurements.

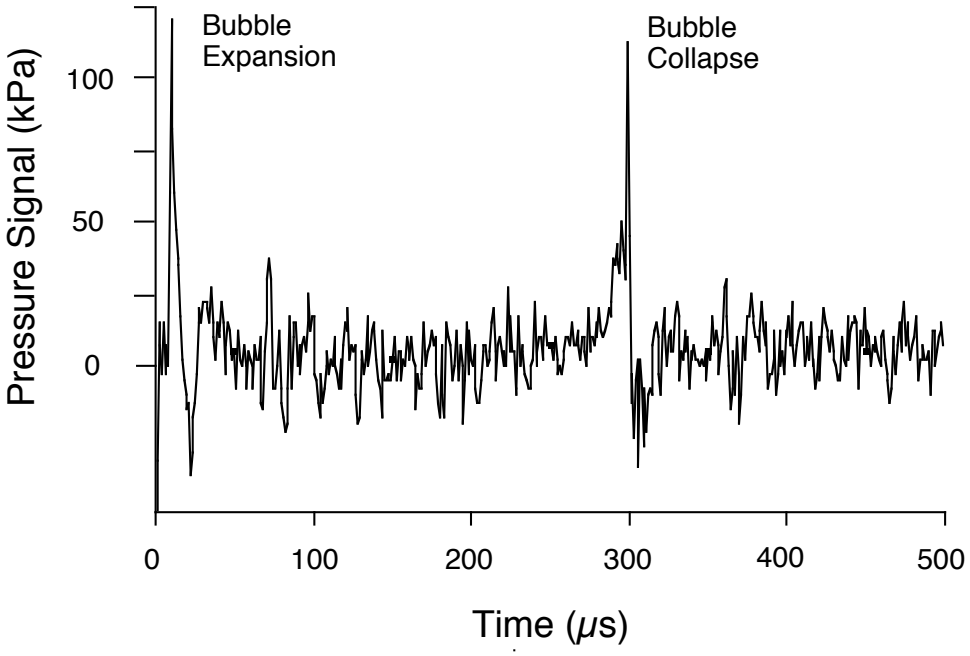

Figure 8.7: The pressures induced by the cavitation bubble following laser irradiation. The times have been corrected for the propagation delay of the pressure signals from the ablation site to the pressure transducer.

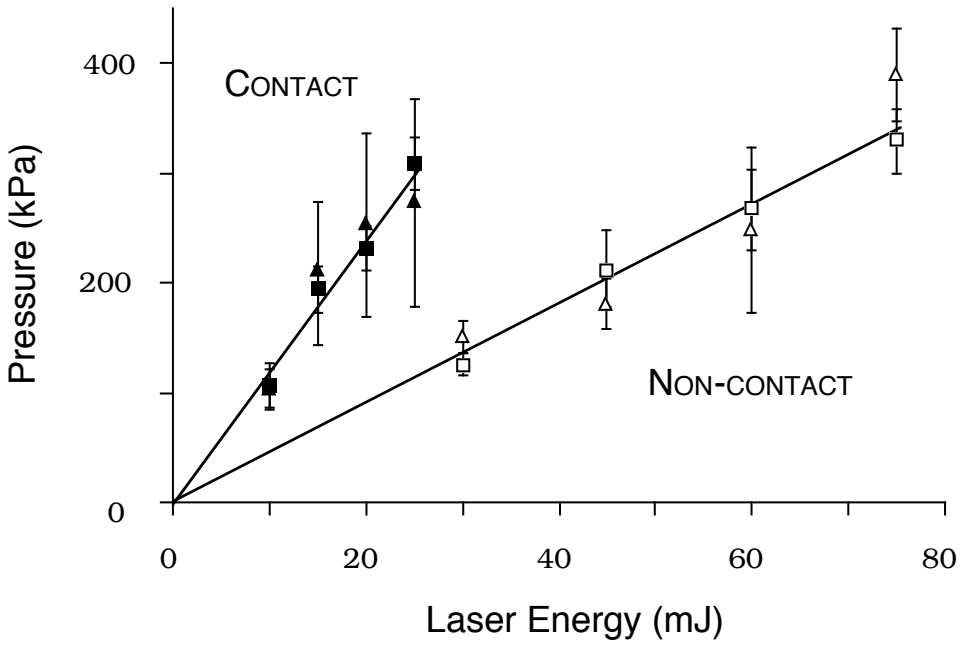

Figure 8.8: Amplitude of the expansion and collapse pressures at a distance of 16 mm from the ablation site. The laser pulses were delivered onto the gelatin via a flushing catheter with a 300 μm fiber. The filled square and triangle are the pressures for contact ablation due to the bubble expansion and collapse respectively. The corresponding non-contact data is represented using the open markers. Error bars represent the standard deviation of six measurements.

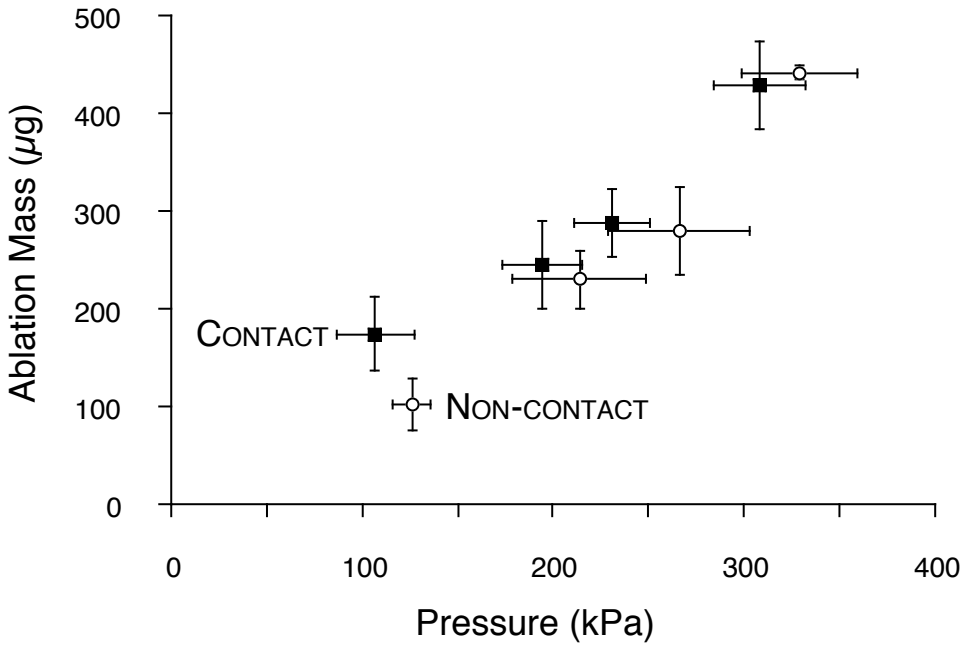

Figure 8.9: Ablation mass of clot as a function of bubble expansion pressure on gelatin. The pressures were measured from gelatin samples with an absorption coefficient of $100\,\mathrm{cm}^{-1}$. Single pulses of 10–25 mJ were delivered onto the gelatin samples via a $300\,\mu$m fiber for contact ablation, while non-contact ablation used energies three times those used for contact ablation. The ablation mass of clot from pig A in Table 2 was measured using the same laser and fiber parameters used for the gelatin experiments.

Contact Delivery					Non-Contact Delivery				
Pulse Energy (mJ)	Spot Size (μm)	Mass per Pulse (μg)	Bubble Size (mm)	Expansion Pressure (kPa)	Pulse Energy (mJ)	Spot Size (μm)	Mass per Pulse (μg)	Bubble Size (mm)	Expansion Pressure (kPa)
		±30	±0.1	±20			±30	±0.1	±30
10	200	130	—	—	30	450	—	—	—
	300	—	2.5	110		480	100	3.1	130
	400	130	—	—		520	70	—	—
15	200	170	—	—	45	450	—	—	—
	300	—	2.7	190		480	160	3.3	210
	400	150	—	—		520	100	—	—
20	200	160	—	—	60	450	140	—	—
	300	170	2.8	230		480	160	3.6	270
	400	140	—	—		520	150	—	—
25	200	210	—	—	75	450	—	—	—
	300	—	2.9	310		480	250	3.7	330
	400	210	—	—		520	180	—	—

Table 8.1: Contact and non-contact ablation experiments. The mass per pulse is the average amount of clot (from pig B in Table 8.2) removed in a single laser pulse. The bubble size and pressure measurements are from gelatin ablation experiments. The errors vary, but typical values are specified in the first row.

Pig	Ablation Efficiency	
	Contact (μg/mJ)	Non-contact (μg/mJ)
A	14±2	4.7±1
B	8±2	2.4±0.3
C	7±1	—

Table 8.2: Variability in porcine clot ablation efficiencies. The average of 180–350 20 mJ laser pulses delivered through a 300 μm fiber for contact ablation and 60 mJ laser pulses were used for non-contact ablation. All data are mean ± standard deviation of five samples.

Chapter 9

Kinetic Energy Generation During Microsecond Laser Ablation

9.1 Introduction

Two phenomena are observed after a intense laser pulse is delivered via an optical fiber into an absorbing liquid or onto an absorbing target under a clear aqueous medium: 1) cavitation or vapor bubble formation and 2) pressure wave generation. Recently the possibility of mechanical damage to the vicinity of the ablation site caused by laser-induced pressure waves has raised increasing concerns. Cavitation effects can cause damage to underlying endothelial cells after superficial irradiation of cornea with Q-switched mid-infrared laser pulses [105]. Dissections of the vascular tissue during holmium laser angioplasty have been reported [44]. A study by van Leeuwen *et al.* suggested that these dissections are caused by the bubble expansion and collapse in tissue [48].

The proceeding chapters demonstrated that laser-induced pressure plays an

important role in local drug delivery and laser thrombolysis. The penetration of drug into thrombus and the ablation efficiency are proportional to the pressures due to the bubble expansion and collapse. Similar pressures could be generated by either contact delivery at a lower laser energy or non-contact delivery at a higher laser energy (at least three times as much as that used in contact delivery). Gross physical displacement of the cuvette containing the irradiation targets was observed during the experiments as well. It seems that the magnitude of the displacement was correlated to the total energy delivered regardless of contact or non-contact delivery. Thus, this study was motivated by two concerns: first, does contact or non-contact delivery generate higher kinetic energy; second, do the impulsive pressures due to the kinetic energy generation cause tissue rebound in such a way that the catheter penetrates into the tissue.

Previous studies of laser-induced pressure waves have focused on the effects of the laser energy, pulse duration, absorption coefficient, fiber size, and material strength on the acoustic pressure generation [91, 109, 138]. The acoustic pressure waves are detected in early expansion phase and in the consequent collapse phase during bubble evolution. However, the mechanical effects of laser-induced kinetic energy generated under an aqueous medium after the bubble formation have not been reported. A relevant study by Snyder *et al.* demonstrated that the average impulse induced pressure of a free running Ho:YAG 2.1 μm in the fiber contact mode (i.e., fiber contacts the tissue) was 2–6 times greater than in the non-contact mode (i.e., the laser energy at the fiber tip was imaged onto the tissue) [139]. Their experiments were performed by ablating the porcine aorta sample mounted

on a pendulum in air. The impulse coupling coefficient was determined from the deflection of the pendulum based on the conservation of momentum.

The aim of this study was to investigate the effect of contact delivery and non-contact delivery on kinetic energy generation. Specifically, the questions to be answered are:

- Does the acoustic pressure correlate with the kinetic energy generation?
- How can the kinetic energy cause rebound of an ablation target?

9.2 Theory

The effects of contact and non-contact delivery on the impulsive pressure generation were investigated by comparing the kinetic energy of the cuvette after the laser pulse. Based on the conservation of the total energy, the change in kinetic energy is

$$K - K_o = mgh - mgh_o \tag{9.1}$$

where K_o and K are the kinetic energies of the cuvette before and after the displacement, respectively, m is the weight of the cuvette, h_o and h are the initial position and the final position of the cuvette, respectively.

In this study, the initial conditions were: $K_o = \frac{1}{2}mv_o^2$, $h_o = 0$, where v_o is the initial velocity before the cuvette takes off. When the cuvette reached its maximum height $K = 0$, $h = h_{max}$. The value of h_{max} was measured using flash photography. Thus, the kinetic energy generated by the laser pulse can be

estimated by

$$K_o = mgh_{max} \tag{9.2}$$

and the initial velocity of the cuvette before taking off is given by

$$v_o = \sqrt{2gh_{max}} \tag{9.3}$$

9.3 Methods and Materials

Two experimental protocols were performed. First, single pulses of 20 mJ were delivered through a flushing catheter with a 300 μm fiber onto gelatin samples under water for contact delivery, while 60 mJ pulses were used for non-contact delivery. The flow rate was 4 mL/min. The flow was stopped immediately after the laser pulse. The two irradiation configurations are shown in Figure 9.1. The m in equation (9.2) was determined by weighing the cuvette containing gelatin sample and water after irradiation. To ensure the weight for each experiment to be similar. The cuvette containing gelatin sample without water was also weighed before irradiation as a reference. The cuvette was placed loosely on a metal plate and the catheter was fixed. The maximum height was determined by varying the delay time (i.e., the period between the end of the laser pulse and the peak of the light from the strobe) until the h reached its maximum (Figure 9.2). Second, the cuvette was suspended using a rubber ring, so that the cuvette didn't contact the metal plate. This experiment used the same laser parameters as those used in the first experiment. The motion of the cuvette was monitored with the flash photography setup (Figure 9.2). The details of this flash photography setup is

described in Chapter 3.

Laser irradiation at 577 nm was provided by flashlamp excited dye lasers (Palomar Medical Technologies). The pulse duration was $\sim$1.3 μs (full width at half maximum). The laser pulses were delivered into absorbing liquids or through clear liquids onto thrombus phantoms via the fiber-optic flushing catheter. The energy per pulse was measured with an joulemeter (Molectron). Pulse-to-pulse energy variation was less than 5%.

The targets were 3.5% gelatin containing Blue 15 dye as the chromophore. Sufficient dye was added to achieve an absorption coefficient of 100 cm^{-1} at 577 nm. The gel preparation is described in detail in Chapter 3.

9.4 Results

Flash photographs revealed that a 20 mJ laser pulse caused a cuvette containing gel and water to rebound a maximum of 1.8$\pm$0.3 mm at 5 ms after the laser pulse using contact delivery. A 60 mJ pulse caused the cuvette to rebound 2$\pm$0.3 mm at 5 ms and reached 4.5$\pm$0.5 mm at 20 ms using non-contact delivery. This height might not be the maximum height that the cuvette could reach, since the image was out of the screen after 20 ms due to the limitation of this photography setup. The weight of the cuvette containing gelatin was 4.6$\pm$0.1 g before the irradiation and 6.5$\pm$0.1 g including gelatin and water after the irradiation for contact delivery. The weight of the cuvette containing gelatin was 4.57$\pm$0.1 g before the irradiation and 6.5$\pm$0.1 g including gelatin and water after the irradiation for contact delivery.

Thus, the differences in the kinetic energy between contact and non-contact delivery was about 1 to 2.5: contact vs. non-contact based on equation (9.2). Typical flash photographs are shown in Figure 9.3 for contact delivery and in Figure 9.4 for non-contact delivery. Five samples were measured for contact delivery, while six samples were used for non-contact delivery.

No displacement of the cuvette was observed when the cuvette didn't contact the metal plate regardless of contact or non-contact delivery, but the surface of the water contained in the cuvette vibrated.

9.5 Discussion

One concern for laser thrombolysis is whether the rapid displacement of fluid in an artery can cause the rebound of the artery wall. This study investigated the effect of contact and non-contact delivery on the kinetic energy generation and how the kinetic energy could cause target rebound.

Thrombus removal depended on the laser-induced pressure wave and similar mass could be removed using similar pressure (Figure 8.9). Contact delivery could generate pressure waves more efficiently than non-contact delivery. Roughly three times as much energy was needed for non-contact to create the same pressure as that created by contact. However, the experimental results in this study demonstrated that the kinetic energy generation strongly depends on the total energy delivered regardless of contact or non-contact delivery. This suggests that the kinetic energy generation is not directly correlated with the acoustic pressure wave.

In Chapter 6, I hypothesized that the delivered laser energy is mainly dissipated through heating, phase changes, acoustic transients, and hydrodynamic flow of liquid (ultimately converted to kinetic energy). The conservation of energy can be used to qualitatively understand the difference in kinetic energy between the contact and non-contact delivery. The incident laser energy is divided by the interaction into five parts:

$$E_{in} = E_{optical} + E_{thermal} + E_{acoustic} + E_{bubble} + E_{kinetic} \tag{9.4}$$

where $E_{optical}$ is the energy loss (i.e., reflection, absorption, and scattering). $E_{thermal}$ is the energy dissipated during heating, phase transitions, and incandescence. $E_{acoustic}$ is the energy used for acoustic radiation. E_{bubble} is the energy dissipated during bubble formation. $E_{kinetic}$ is the energy following the bubble collapse.

For the absorbing gelatin used in this study, the reflected and back scattered losses are negligible due to the high absorption of the gelatin ($100\,\mathrm{cm}^{-1}$). The acoustic transient measurements in Chapter 8 showed that the acoustic pressure waves were similar for both contact ablation and non-contact ablation when the ratio of the energy delivered was 1 to 3: contact vs. non-contact. Thus, $E_{acoustic}$ in equation (9.4) is equal for both of contact and non-contact ablation. The differences in E_{bubble} between both cases is about 20% (Figure 8.6) since the energy used for the bubble formation is proportional to the bubble diameter (width). The measurement in this present study showed that the kinetic energy for non-contact ablation was roughly three times greater than that for contact delivery. Thus, the thermal energy losses for both cases is similar. Furthermore,

this implies that the thermal energy depends on the absorption of the ablation target regardless of the light delivery, and excess energy would be dissipated as acoustic radiation, bubble formation, and kinetic energy.

No displacement of the cuvette was observed when the cuvette didn't contact the metal plate. This result is most likely because no force could be reflected from the rigid metal plate. It was also observed that the displacement of the cuvette decreased dramatically when a soft material (e.g., tissue paper) was put between the bottom of the cuvette and the metal plate. This suggests that the kinetic energy wouldn't cause the target rebound as long as there is no hard boundary that causes reflection of the pressure wave. However, the water contained in the cuvette vibrated. This is most likely caused by the flow motion following the bubble formation inside the cuvette. It is not clear whether the flow motion could cause the catheter to move.

In conclusion, this study demonstrated that the kinetic energy generation strongly depends on the total energy delivered regardless of the light delivery (e.g., contact and non-contact delivery) and that the kinetic energy generation is not directly correlated with the acoustic transients. The rebound of the ablation targets occurs only when the target is supported by hard boundary. In most cardiovascular applications, the obstructed vessels are surrounded by soft tissues, and it is unlikely that the rebound of thrombus due to the kinetic energy generation can cause the surrounding vessel to jump, so much that the catheter impinges on the vessel.

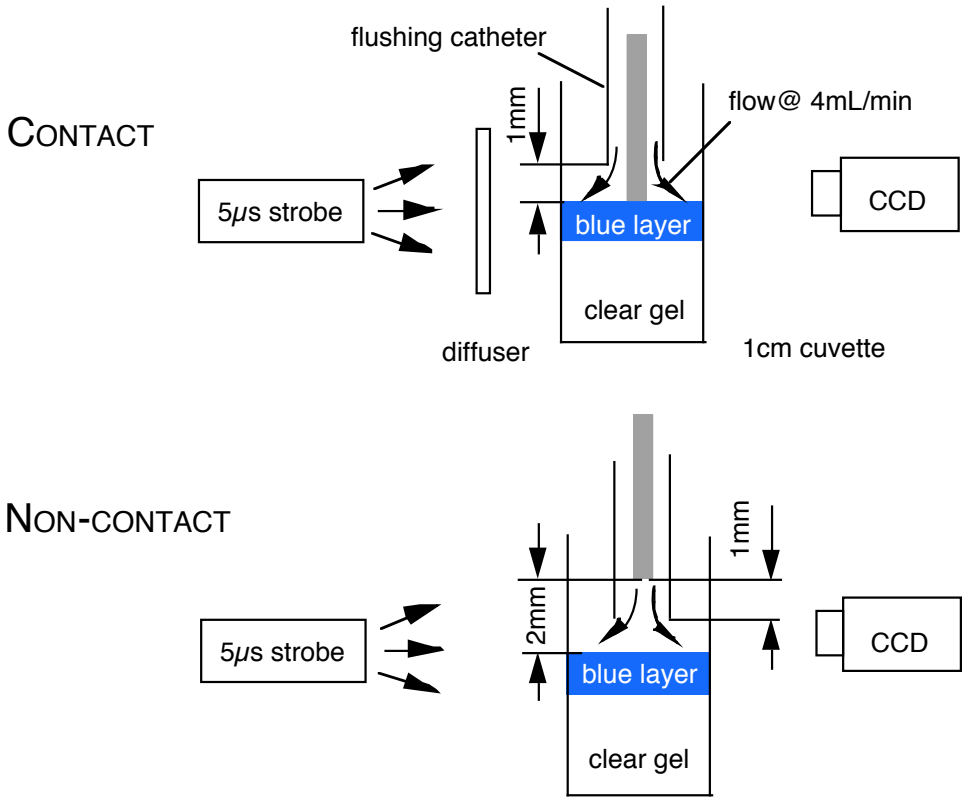

Figure 9.1: Schematic illustration of two irradiation configurations (contact and non-contact delivery).

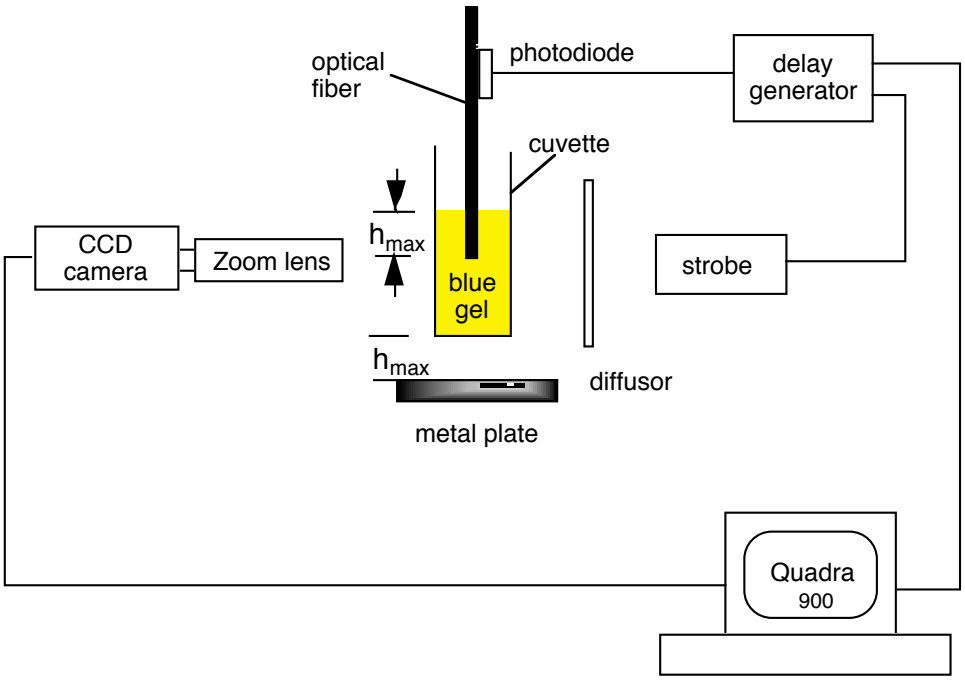

Figure 9.2: Experimental setup for the kinetic energy measurement.

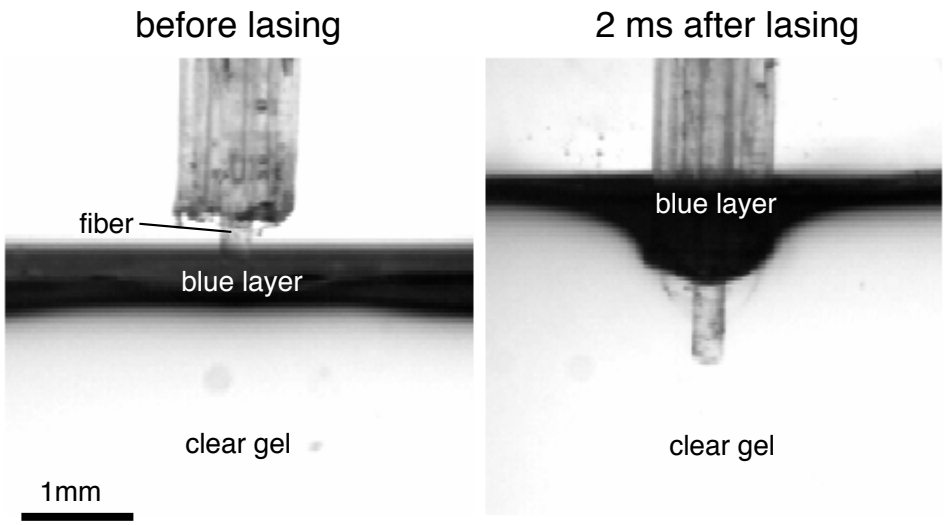

Figure 9.3: Side view of a flushing catheter before and after the laser pulse for contact delivery. A single pulse of 20 mJ was delivered onto the blue gel layer under water.

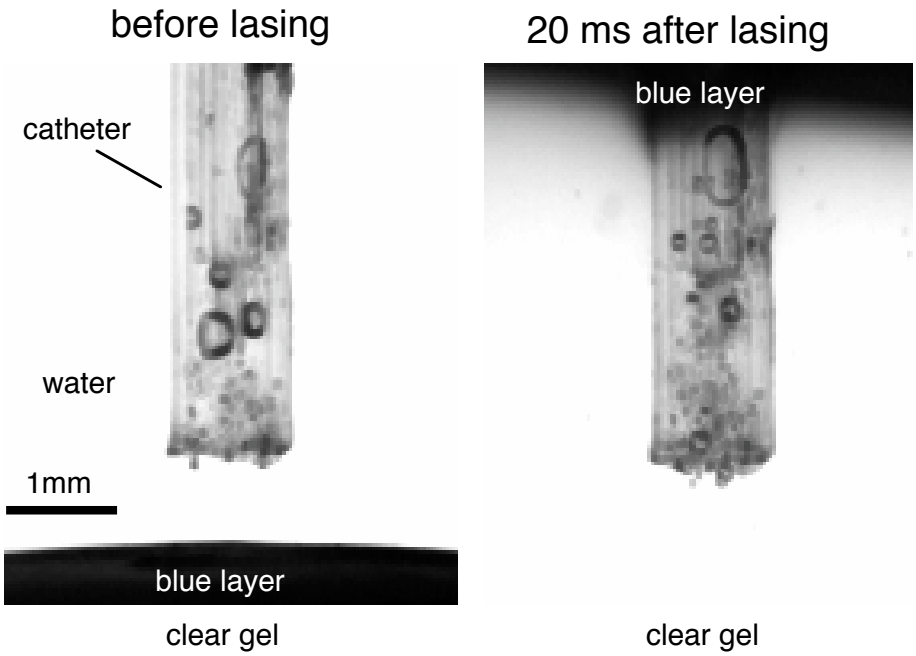

Figure 9.4: Side view of a flushing catheter before and after the laser pulse for non-contact delivery. A single pulse of 60 mJ was delivered onto the blue gel layer under water.

Chapter 10

General Discussion and Conclusions

The global goal of the *in vitro* studies presented in this dissertation was to investigate the possibility of photomechanical drug delivery as a new means of localized drug delivery to thrombus for enhancement of laser thrombolysis. Three broad subjects investigated were as follows:

- characterization of laser-induced cavitation phenomena that take place during photomechanical drug delivery,
- photomechanical drug delivery to thrombus,
- effects of contact and non-contact delivery on laser thrombolysis, drug delivery, and kinetic energy generation.

Most experiments were performed on controlled media such as absorbing liquids and gelatin under non-physiological conditions, although the target material of interest was blood clot. The processes that take place in these controlled

media provide insight into the phenomena that are taking place during photomechanical drug delivery *in vivo* without the biological variation of real clot. The underlying motivation for this study was that knowledge of the basic science involved in photomechanical drug delivery may make it possible to specify optimal laser parameters for the design of localized drug delivery systems. This chapter summarizes the most important observations and conclusions of this dissertation.

10.1 Laser-induced Cavitation Bubble Dynamics

10.1.1 Threshold Study

Photomechanical drug delivery uses the hydrodynamic pressures arising from the expansion and collapse of laser-induced cavitation bubbles as a driving force to deliver clot-dissolving drugs into thrombus during laser thrombolysis to enhance the thrombolysis process. To safely achieve photomechanical drug delivery in arteries, the threshold radiant exposure for bubble formation should be less than that required to ablate the arterial tissue. Previous studies have measured the ablation thresholds for lysed blood, thrombus, and atheroma under saline at 577 nm, 504 nm, 465 nm and 488 nm using pulsed-dye lasers [37, 53, 87, 136]. Several investigators also have extensively investigated the threshold for cavitation bubble formation in water using the ultraviolet excimer laser (XeCl at 308 nm, pulse duration = 115 ns) and the mid-infrared holmium:YAG laser (wavelength = 2.12 μm) [83, 84]. However, no parametric study of the threshold for bubble

formation in light absorbing liquids, especially in oil, using pulsed-dye lasers has been reported. The aims of this study were to establish the minimum laser energy to initiate the bubble formation in light-absorbing liquids with different physical properties (e.g., heat capacity, latent heat, and viscosity) using a pulsed-dye laser and to investigate the effects of absorption and radiant exposure on the thresholds.

The threshold study was presented in Chapter 3. The threshold radiant exposure was measured as a function of absorption coefficient ranging from 6–300 cm^{-1} and fiber size (diameter) ranging from 200–1000 μm. The thresholds for bubble formation in oil solutions were less than those in water solutions. The two proposed mechanisms for bubble formation in absorbing liquids are: 1) The onset of bubble formation (i.e., at threshold radiant exposure) depends on the physical properties of the liquids such as specific heat and absorption coefficient (equation 3.6) and 2) the volume expansion coefficient plays an important role for bubble formation at supra-thresholds (equation 3.19).

The results of temperature estimation showed that the temperature of a liquid layer under the fiber tip could reach the boiling point for both water and oil solutions with higher absorption coefficients (e.g., 300 cm^{-1}) and that the stress waves caused the decrease in thresholds, resulting in a lower temperature for the liquids with a lower absorption coefficient (e.g., 6 cm^{-1}). This suggests that the layer needs to be raised to just above the temperature at the boiling point. However, this is unnecessary for the solution with a lower absorption coefficient due to the effect of the stress waves [86].

The onset of bubble formation is initiated at a threshold radiant exposure (energy per unit area) rather than the total energy delivered because the temperatures of the absorbing layers depend on the radiant exposure and the absorption coefficient (equation 3.8). As a consequence, the extra energy above the threshold would be dissipated for the phase change and bubble expansion. The threshold radiant exposures for bubble formation have been established, which provide important information for investigating the dynamic behavior of cavitation bubbles at supra-thresholds. Furthermore, the thresholds for bubble formation in absorbing liquids were much less than those needed to ablate the normal tissue, which ensures the safe achievement of photomechanical drug delivery in fluid-filled vessels. For example, the threshold for bubble formation in water solution with an absorption coefficient of $300\,\mathrm{cm}^{-1}$ is $\sim$17 $\mathrm{mJ/mm}^2$, while the ablation threshold for normal rabbit femoral arterial tissue is $\sim$160 $\mathrm{mJ/mm}^2$ for twenty pulses under blood ($300\,\mathrm{cm}^{-1}$ at 480 nm) [55].

10.1.2 Dynamic Behavior of Cavitation Bubbles

Pulsed laser ablation of blood clot in a fluid-filled vessel is always accompanied by an explosive evaporation process. The resulting cavitation bubble rapidly expands and collapses to disrupt the thrombus (blood clot). The hydrodynamic pressures following the bubble expansion and collapse can also be used for photomechanical drug delivery. Although several studies have focused on the laser-induced cavitation or vapor bubble dynamics [90, 91, 98, 99], no detailed study has been done on the dynamic behavior of a laser-induced cavitation

bubbles in light absorbing liquids or on soft targets with different physical properties using a pulsed-dye laser. The aim of this study was to characterize the cavitation phenomena that take place in these two conditions (see Chapter 4). The experimental protocols were designed to address the following questions:

- What is the role of laser energy, radiant exposure, and absorption in the bubble formation at supra-threshold?
- How do the different liquids surrounding a fiber tip or on a target surface affect the bubble formation, and how does the mechanical strength of thrombus affect the removal process?
- What are the effects of the boundaries of the fiber and container on the bubble formation under clinically relevant boundary conditions?

Some portion of the extra laser energy above the threshold contributed to the bubble formation. The bubble volume depended on the laser energy, fiber size, and absorption coefficient, such that bubbles of the same size could be produced by suitable selection of these parameters. For example, a cavitation bubble 3.2 mm in diameter can be produced in unbounded colored oil ($300\,\mathrm{cm}^{-1}$) by a $300\,\mu$m fiber at 33 mJ, by a $600\,\mu$m fiber at 50 mJ, or by a $1000\,\mu$m fiber at 100 mJ, with an error estimate of less than 5%. However, the use of a small fiber produced small bubbles at constant radiant exposure (Figure 4.6). This observation suggests that there is a threshold effect, i.e., the bubble formation will be governed by laser energy below this threshold, while the radiant exposure dominates the bubble dimensions above this threshold.

The bubble formation in absorbing liquids was strongly affected by the physical properties of the liquids. The effects of the material properties of the liquids were not significant when the bubbles were formed on soft targets (thrombus phantom) under the liquids. This is because bubble formation depends on where the laser energy is absorbed. When the bubble is formed in absorbing liquids the physical properties of the liquids such as specific heat, latent heat, and volume expansion coefficient will dictate the bubble formation, while the properties of gelatin phantoms will dictate the bubble formation as the bubble is formed in absorbing gelatin as long as the bubble expansion pressure can overcome the static ambient pressure of the surrounding liquids. The observation that the mechanical strength of gelatin phantoms affected the bubble dynamics confirms this explanation. I developed a method to visualize the bubble formation on colored gelatin surface by forming a colored layer on the clear gelatin, and first showed that a spherical bubble was formed on the absorbing gelatin under clear liquids rather than a hemispherical bubble.

A theoretical model was used to estimate the bubble volumes formed in absorbing liquids. This model assumed vaporization of the entire disk of absorbing liquids under a delivery fiber, rather than vaporization of a fraction of the disk although some disturbances at nucleation sites were observed beneath the fiber tip when the laser energy was below the threshold. Good agreement was found between the model and experimental results.

10.1.3 Pressure Wave

Pressure waves were emitted upon expansion and collapse of a cavitation bubble [91]. The amplitude of these pressures are related to the bubble size. A bubble of same size generated by different laser parameters produces the similar pressures. The bubble oscillation was observed when the bubble was formed in absorbing liquids or on targets with higher mechanical strengths (e.g., 5% 300 bloom gelatin phantom). No re-expansion was observed when the bubble was formed on softer gelatin surface (e.g., 3.5% 60 bloom gelatin phantom) since the ejection of material followed the bubble collapse. The above mentioned pressures are likely the acoustic transients rather than the hydrodynamic pressure that caused the flow motion. It is unclear what the relationship between the hydrodynamic pressure and acoustic transient is.

10.2 Photomechanical Drug Delivery

Although rapidly expanding and collapsing bubbles and high pressure transients generation inside arteries have been shown to cause perforation and dissections of arteries [48], these forces might be harnessed under controlled conditions to produce therapeutic effects. It has been established that the bubbles can be generated by delivering laser pulses either into absorbing liquids or onto absorbing targets through fiber-optic catheters. It has also shown that the bubble expansion and collapse could cause the surrounding fluid to move at a speed up to 12 m/s (see Chapter 5).

The experiments in Chapters 6 and 7 showed that drug was most likely driven into the thrombus by hydrodynamic flow that was due to the cavitation bubble formation, inasmuch as the acoustic transients arising from the bubble formation since the acoustic transients passed through the sample and reached the transducer before the colored oil was forced into the gelatin. In this sense, the type of drug delivery described in this study has been termed as photomechanical drug delivery. However, it remains unclear whether the acoustic transients contribute to the delivery through other mechanisms that might weaken the gelatin before the onset of hydrodynamic flows.

The spatial distribution of drug in thrombus depends on the pressures arising from the bubble formation. Similar pressures resulted in the similar penetration. The results of using thrombus phantoms were comparable to those obtained using porcine clots. The drug deliver to arterial tissue may be achieved using photomechanical drug delivery since the fluorescence on the porcine aorta surface was enhanced after laser irradiation due to the penetrated dye.

10.3 Effects of Contact and Non-contact Delivery

The results of Chapter 8 demonstrated that the ablation process is profoundly affected by whether the optical fiber tip is inside a catheter or is in contact with the thrombus. The contact ablation efficiency of porcine clot was at least three times greater than the non-contact ablation efficiency. This is because contact ablation achieved higher bubble expansion pressures for a given pulse energy due

to the presence of the boundary of the fiber tip [137]. The 1 μm fluorescent microspheres penetrated the mural clot the same distance for both ablation methods, and this suggests that either method might be used for localized drug delivery to enhance the thrombolysis process.

The experiments in Chapter 9 demonstrated that the impulsive pressure due to the kinetic energy generation was proportional to the total delivered energy regardless of the delivery method. A simple model was presented to quantitatively analyze the energy balance after a laser pulse is delivered into an ablation target based on the hypothesis that laser energy is mainly dissipated through heating, phase changes, acoustic transients, and hydrodynamic flow of liquid (ultimately converted to kinetic energy).

10.4 Conclusions

In conclusion, this dissertation addressed several aspects of localized drug delivery with microsecond laser pulses and has demonstrated:

1. The threshold radiant exposures for bubble formation in absorbing oil solutions were less than for bubbles formed in absorbing water solutions. The volume expansion coefficient may play an important role in bubble formation at supra-threshold radiant exposure.

2. The laser-induced cavitation bubble dynamics depended on where the laser energy is absorbed. The effects of density and viscosity of liquids above the thrombus on the bubble formation are negligible when the laser energy

is absorbed by absorbing gelatin. The bubble dimensions are significantly different when the light is absorbed by the liquids. The mechanical strength of thrombus also affected the bubble formation. The bubble expansion and collapse could cause the surrounding flow motion at a speed of up to 12 m/s. A theoretical model was used to estimate the bubble volumes formed in absorbing liquids. This model assumed vaporization of the entire disk of absorbing liquid under a delivery fiber, rather than vaporization of a fraction of the disk. Good agreement was found between the model and experimental results.

3. The drug could be driven into thrombus several hundred micrometers and even a few millimeters in both axial and radial directions when the gelatin structures were fractured. The results of using gelatin were comparable to those obtained using porcine clots. The cavitation bubble formation (i.e., expansion and collapse) is the governing mechanism for photomechanical drug delivery. The bubble expansion and collapse produced high hydrodynamic pressures with an amplitude of several hundred kilopascals.

4. The ablation process was profoundly affected by whether the optical fiber tip was inside a catheter or was in contact with the thrombus when the laser light was delivered through an optical fiber to the thrombus. The contact ablation efficiency of porcine clot was at least three times greater than the non-contact ablation efficiency. Furthermore, the mass removed per unit laser energy was relatively constant for both laser energy and fiber

size. The mass ablated was correlated with the expansion and collapse pressure of the cavitation bubble. This result provides an important piece of information for designing clinical clot ablation systems: pressure is the most important factor in establishing the ablation efficiency of a one microsecond laser pulse. The microspheres penetrated the mural clot the same distance for both ablation methods and suggests that either method might be used for localized drug delivery to enhance the thrombolysis process.

5. The kinetic energy generation strongly depended on the total energy delivered regardless of the light delivery (e.g., contact and non-contact delivery). Kinetic energy generation was not directly correlated with the acoustic transients. The rebound of ablation targets occurred only when the target was supported by a hard boundary.

10.5 Implications

This study has demonstrated the possibility of using microsecond laser pulses for localized drug delivery to thrombus. The drug could be driven into thrombus several hundred micrometers and even few millimeters in both axial and radial directions when the gelatin structures were fractured. The lumen areas increased by 25% by accounting for the areas that may be potentially dissolved by the drugs. The results of using absorbing gelatin were comparable to those obtained using porcine clots. Therefore, the thrombolysis process may be enhanced through delivery of clot-dissolving drugs to thrombus *in vivo*.

It has been shown that the rapidly expanding and imploding bubble may cause mechanical damage [48]. Reducing the bubble dimensions has been proposed as a promising strategy for minimizing the photomechanical effect [89–91]. This study suggests that the bubble size may be reduced by using a liquid in which small bubbles are formed like oil rather than water.

Photomechanical drug delivery can be achieved selectively by use of different strategies to generate the laser-induced hydrodynamic pressures in fluid-filled vessels. One is to generate a bubble on the thrombus due to the absorption of laser energy by the thrombus in coincidence with injection of drug. In this case, the effect of drug with different physical properties on the bubble formation will be negligible. The other method is to create a bubble in the surrounding liquid (saline or blood), and the bubble dimensions can be controlled by either the properties of the fluid or by using different laser parameters.

Cavitation bubble formation in this study is similar to that observed when a Q-switched holmium laser is focused in water. The absorption coefficient of water at 2.1 μm is 30 cm^{-1}. The Q-switched pulse length is $\sim$1 μs and is therefore comparable with those used in this study. In this study and in those of Jansen *et al.* the cavitation bubbles are formed at the fiber tip after the laser pulse owing to the laser energy absorption by the liquid [84]. The Q-switched holmium laser can be used for photomechanical drug delivery, although the penetration will be half that of a 577-nm pulsed dye laser in blood (absorption coefficient of 300 cm^{-1}) (see Table 6.1).

This study also demonstrated that the contact ablation efficiency of porcine

clot was at least three times greater than the non-contact ablation efficiency. Furthermore, the mass removed per unit laser energy was relatively constant for both laser energy and fiber size. The mass ablated was correlated with the expansion pressure of the cavitation bubble. This result provides an important piece of information for designing clinical clot ablation systems: pressure is the most important factor in establishing the ablation efficiency of a one microsecond laser pulse. This is important because previous studies have demonstrated that cavitation bubbles can structurally deform vessel walls and possibly lead to damage of the vessel walls [88,97]. Since larger bubbles generate greater pressures, a greater number of smaller bubbles may allow safer, more controlled, laser ablation of clot in arteries.

Photomechanical drug delivery may be applicable for drug delivery to arterial tissue, since promising results of photomechanical drug delivery to porcine aorta have also been obtained, although further investigation is needed. Thus, this study is promising because it may help to advance photomechanical drug delivery from an experimental observation to a clinically useful therapeutic therapy.

Bibliography

[1] K. Gregory, "Laser thrombolysis," in *Interventional Cardiology* (E. J. Topol, ed.), vol. 2, ch. 5, pp. 892–902, W. B. Saunders Company, 1994.

[2] H. Shangguan, L. W. Casperson, A. Shearin, K. W. Gregory, and S. A. Prahl, "Photoacoustic drug delivery: the effect of laser parameters on spatial distribution of delivered drug," in *SPIE Proceedings of Laser-Tissue Interaction VI* (S. L. Jacques, ed.), vol. 2391, pp. 394–402, 1995.

[3] H. Shangguan, A. Shearin, and S. A. Prahl, "Visualization of photoacoustic drug delivery dynamics," *Lasers Surg. Med.*, vol. 57, pp. 4–5, 1995 (abstract).

[4] H. Shangguan, L. W. Casperson, and S. A. Prahl, "The effect of absorption coefficient and radiant exposure on the threshold of cavitation bubble formation in light absorbing liquids," *Proceedings of the Oregon Academy of Science*, 1995 (abstract).

[5] H. Shangguan, L. W. Casperson, A. Shearin, and S. A. Prahl, "Investigation of cavitation bubble dynamics using particle image velocimetry: implications for photoacoustic drug delivery," in *SPIE Proceedings of Lasers in Surgery: Advanced Characterization, Therapeutics, and Systems VI* (R. R. Anderson and A. Katzir, eds.), vol. 2671, pp. 104–115, 1996.

[6] H. Shangguan, L. W. Casperson, A. Shearin, K. W. Gregory, and S. A. Prahl, "Drug delivery with microsecond laser pulses into gelatin," *Appl. Opt.*, vol. 35, pp. 3347–3357, 1996.

[7] H. Shangguan, L. W. Casperson, and S. A. Prahl, "Microsecond laser ablation of thrombus and gelatin under clear liquids: Contact vs non-contact," *to be published in IEEE Quantum Electronics.*

[8] H. Shangguan, L. W. Casperson, A. Shearin, D. Paisley, and S. A. Prahl, "Effects of material properties on laser-induced bubble formation in absorbing liquids and on submerged targets," in *Proceedings of the 22nd International Congress on High-speed Photography and Photonics*, 1996 (in press).

[9] H. Shangguan, L. W. Casperson, K. W. Gregory, and S. A. Prahl, "Penetration of fluorescent particles in gelatin during laser thrombolysis," in *SPIE Proceedings of Diagnostic and Therapeutic Cardiovascular Interventions VII*, 1997.

[10] H. Shangguan, L. W. Casperson, and S. A. Prahl, "Effects of laser delivery on ablation efficacy of thrombus in liquids: In vitro study," *Lasers Surg. Med.*, 1997 (abstract).

[11] V. Fuster and e. M. Verstraete, *Thrombosis in cardiovascular disorders*. W. B. Saunders Company, 1992.

[12] F. Fuster, L. Badimon, J. J. Badimon, and J. H. Chesebro, "The pathogenesis of coronary artery disease and the acute coronary syndromes: part 1," *New Engl. J. Med.*, vol. 326, pp. 242–250, 1992.

[13] F. Fuster, L. Badimon, J. J. Badimon, and J. H. Chesebro, "The pathogenesis of coronary artery disease and the acute coronary syndromes: part 2," *New Engl. J. Med.*, vol. 326, pp. 310–318, 1992.

[14] V. J. Marder and S. Sherry, "Thrombolytic therapy: current status: part 1," *New Engl. J. Med.*, vol. 318, pp. 1512–1585, 1988.

[15] W. McBride, R. A. Lange, and L. D. Hillis, "Restenosis after successful coronary angioplasty," *The New England J. Medicine*, vol. 318, pp. 1734–1737, 1988.

[16] D. D. Sugrue, D. R. Holmes, H. C. Smith, G. S. Reeder, D. E. Lane, R. E. Vlietstra, J. F. Bresnahan, and J. M. Piehler, "Coronary artery thrombus as a risk factor for acute vessel occulusion during percutaneous coronary angioplasty: improved results," *Br Heart J.*, vol. 53, pp. 62–66, 1986.

[17] R. R. Arora, W. P. Platko, K. Bhadwar, and C. Simpfendofer, "Role of intracoronary thrombus in acute complications during percutaneous coronary angioplasty," *Cathet Cardiovasc Diagn.*, vol. 16, pp. 226–229, 1989.

[18] G. Lee, "Effects of laser irradiation on human thrombus: Demonstration of a linear dissolution-dose relation between clot length and energy density," *Am. J. Cardiol.*, vol. 52, pp. 876–877, 1983.

[19] F. Crea, A. Fenech, W. Smith, C. R. Conti, and G. S. Abela, "Laser recanalization of acutely thrombosed coronary arteries in live dogs," *J. Am. Coll. Cardiol.*, vol. 6, pp. 1052–1056, 1985.

[20] G. S. Abela, S. J. Normann, D. M. Cohen, D. Franzini, R. L. Feldman, F. Crea, A. French, C. J. Pepine, and C. R. Conti, "Laser recanalization of occluded atherosclerotic arteries *in vivo* and *in vitro*," *Circulation*, vol. 71, pp. 403–411, 1985.

[21] T. A. Sanborn, D. P. Faxon, and C. H. *et al.* , "Experimental angioplasty: Circumferential distribution of laser thermal energy with a laser probe," *J Am Cardiol*, vol. 5, pp. 934–938, 1985.

[22] H. Hussein, "A novel laser probe for treatment of occlusive vessel disease," *Opt. Tech. Med.*, vol. 605, pp. 59–66, 1986.

[23] A. J. Welch, A. B. Bradley, J. H. Torres, M. Motamedi, J. J. Ghidoni, J. A. Pearce, H. Hussein, and R. A. O'Rourke, "Laser probe ablation of normal and atherosclerotic human aorta *in vitro*: A first thermographic and histologic analysis," *Circulation*, vol. 76, pp. 1353–1363, 1987.

[24] G. L. LeCarpentier, S. Rastegar, A. J. Welch, S. A. Prahl, and H. Hussein, "Comparative analysis of laser ablation of plaque using direct laser irradiation and a metal contact probe," in *Phys. Med. Biol.* (J. W. Clark, P. I. Horner, A. R. Smith, and K. Strum, eds.), vol. 33, (San Antonio, TX), p. 17, 1988.

[25] J. D. Labs, P. L. Caslowitz, and G. M. Williams, "Experimental treatment of thrombotic vascular occlusion," *Lasers Surg. Med.*, vol. 11, pp. 363–371, 1991.

[26] T. Tomaru, G. S. Abela, J. Gonzales, P. Giacomino, S. E. Friedl, and G. R. Barbeau, "Laser recanalization of thrombosed arteries using thermal and/or modified optical probes; angiographic and angioscopic study," *Angiology*, vol. 43, pp. 412–420, 1992.

[27] P. C. Douek, R. Correa, R. Neville, E. F. Unger, M. Shou, S. Banai, V. J. Ferrans, S. E. Epstein, M. B. Leon, and R. F. Bonner, "Dose-dependent smooth muscle cell proliferation induced by thermal injury with pulsed infrared lasers," *Circulation*, vol. 86, pp. 1249–1256, 1992.

[28] J. T. Walsh Jr. and T. F. Deutsch, "Pulsed CO_2 laser tissue ablation: Effect of tissue type and pulse duration," *Lasers Surg. Med.*, vol. 8, pp. 108–118, 1988.

[29] S. L. Jacques, "Role of tissue optics and pulse duration on tissue effects during high-power laser irradiation," *Appl. Opt.*, vol. 32, pp. 2447–2454, 1993.

[30] R. R. Anderson and J. A. Parrish, "Selective photothermolysis: Precise microsurgery by selective absorption of pulsed radiation," *Science*, vol. 220, pp. 524–527, 1983.

[31] R. Linsker, R. Srinivasan, J. J. Wynne, and D. R. Alonso, "Far-ultraviolet laser ablation of atherosclerotic lesions," *Lasers Surg. Med.*, vol. 4, pp. 201–206, 1984.

[32] W. S. Grundfest, F. Litvack, J. S. Forrester, H. J. C. Swan, T. Goldenberg, L. Morgenstern, M. Fishbein, I. S. McDermid, D. M. Rider, T. J. Pacala, and J. B. Laudenslager, "Laser ablation of human atherosclerotic plaque without adjacent tissue injury," *J. Am. Coll. Cardiol.*, vol. 5, pp. 929–933, 1985.

[33] J. M. Isner, R. F. Donaldson, L. I. Deckelbaum, R. H. Clarke, S. M. Laliberte, D. M. Salem, and M. A. Konstam, "The excimer laser: Gross, light microscopic, and ultrastructural analysis of potential advantages for use in laser therapy of cardiovascular disease," *J. Am. Coll. Cardiol.*, vol. 6, pp. 1102–1109, 1985.

[34] L. I. Deckelbaum, J. M. Isner, R. F. Donaldson, R. H. Clarke, S. Laliberte, A. S. Aharon, and J. S. Bernstein, "Reduction of laser-induced pathologic tissue injury using pulsed energy delivery," *Am. J. Cardiol.*, vol. 56, pp. 662–667, 1985.

[35] F. Litvack, N. L. Eigler, and J. S. Forrest, "Insearch of the optimized excimer angioplasty system," *Circulation*, vol. 87, pp. 1421–1422, 1993.

[36] G. H. Pettit, I. S. Saidi, F. K. Tittel, R. Sauerbrey, J. Cartwright, R. Farrell, and C. R. Benedict, "Thrombolysis by excimer laser photoablation," *Lasers Life Sci.*, vol. 5, pp. 185–197, 1993.

[37] M. R. Prince, T. F. Deutsch, A. F. Shapiro, R. J. Margolis, A. R. Oseroff, J. T. Fallon, J. A. Parrish, and R. R. Anderson, "Selective ablation of atheromas using a flashlamp-excited dye laser at 465 nm," *Proc. Natl. Acad. Sci. USA*, vol. 83, pp. 7064–7068, 1986.

[38] M. R. Prince, T. F. Deutsch, M. M. Mathews-Roth, R. Margolis, J. A. Parrish, and A. R. Oseroff, "Preferential light absorption in atheromas *in vitro*," *J. Clin. Invest.*, vol. 78, pp. 295–302, 1986.

[39] G. M. LaMuraglia, R. R. Anderson, J. A. Parrish, D. Zhang, and M. R. Prince, "Selective laser ablation of venous thrombus: Implications for a new approach in the treatment of pulmonary embolus," *Lasers Surg. Med.*, vol. 8, pp. 486–493, 1988.

[40] G. M. LaMuraglia, M. R. Prince, N. S. Nishioka, S. Obremski, and R. Birngruber, "Optical properties of human arterial thrombus, vascular grafts, and sutures: Implications for selective laser thrombus ablation," *IEEE J. Quantum Electron.*, vol. 26, pp. 2200–2206, 1990.

[41] K. W. Gregory, M. R. Prince, G. M. LaMuraglia, T. J. Flotte, L. Buckley, J. M. Tobin, A. A. Ziskind, J. Caplin, and R. R. Anderson, "Effect of blood upon the selective ablation of atherosclerotic plaque with a pulsed dye laser," *Lasers Surg. Med.*, vol. 10, pp. 533–543, 1990.

[42] G. E. Kopchok, R. A. White, M. Tabbara, V. Saadatmanesh, and S. Peng,

"Holmium:YAG laser ablation of vascular tissue," *Lasers Surg. Med.*, vol. 10, pp. 405–413, 1990.

[43] H. J. Geschwind, J. L. Dubois-Rande, R. Zelinsky, J. F. Morelle, G. Boussignac, and F. Veyssiere, "Percutaneous coronary mid-infrared laser angioplasty," *Am. Heart J.*, vol. 122, pp. 552–558, 1991.

[44] W. Knopf, K. Parr, J. Moses, C. Cates, W. Groh, C. Stark, R. Johnson, E. Harlamert, A. Fiedotin, and D. Murphy-Chutorian, "Holmium laser angioplasty in coronary arteries," *J. Am. Coll. Cardiol.*, vol. 19A, p. 325, 1992.

[45] K. Rosenfield, A. Pieczek, D. W. Losordo, B. D. Kosowsky, K. Ramaswamy, J. O. Pastore, and J. M. Isner, "Excimer laser thrombolysis for rapid clot dissolution in lesions at high risk for embolization: A potentially useful new application for excimer laser," *J. Am. Coll. Cardiol.*, vol. 19 (suppl), p. 104, 1992.

[46] P. Estella, J. A. Bittl, J. M. Landzberg, and T. J. Ryan, "Intracoronary thrombus increases the risk of excimer laser coronary angioplasty," *Circulation*, vol. 86 (suppl), p. 654, 1992.

[47] R. Srinivasan and W. Leigh, "Ablative photo-decomposition action of far-ultra-violet (193 nm) laser radiation on poly (ethylene terophythalate) films," *J. Am. Chem. Soc.*, vol. 104, pp. 5784–5785, 1982.

[48] T. G. van Leeuwen, van Erven, J. H. Meertens, M. Motamedi, M. J. Post, and C. Borst, "Original of arterial wall dissections induced by pulsed excimer and mid-infrared laser ablation in the pig," *J. Am. Coll. Cardiol.*, vol. 19, pp. 1610–1618, 1992.

[49] O. N. Topaz, A. Eliezer, A. Rozenbaum, S. Battista, C. Peterson, and D. G. Wysham, "Laser facilitated angioplasty and thrombolysis in acute myocardial infarction complicated by prolonged or recurrent chest pain," *Cathet. Cardiovasc. Diagn.*, vol. 28, pp. 7–16, 1993.

[50] M. A. Pathak, T. B. Fitzpatrick, and J. A. Parrish, "Photosensitivity and

other reactions to light," in *Harrison's Principles of Internal Medicine* (K. J. Isselbaher, ed.), pp. 255–262, New York: McGraw-Hill, 9 ed., 1980.

[51] T. Tomaru, H. J. Geschwind, G. Boussignac, F. Lange, and S. J. Tahk, "Characteristics of shock waves induced by pulsed lasers and their effects on arterial tissue: Comparison of excimer, pulse dye, and holmium YAG lasers," *Am. Heart J.*, vol. 123, pp. 896–904, 1992.

[52] S. Hassenstein, H. Hanke, and S. Hanke, "Incidence of thrombotic occlusions in experimental holmium laser angioplasty compared to excimer laser angioplasty," *Circulation*, vol. 84(suppl. II), p. 124, 1991.

[53] G. M. LaMuraglia, S. Murray, R. R. Anderson, and M. R. Prince, "Effect of pulse duration on selective ablation of atherosclerotic plaque by 480- to 490-nanometer laser radiation," *Lasers Surg. Med.*, vol. 8, pp. 18–21, 1988.

[54] K. W. Gregory, P. C. Block, W. A. Knopf, L. A. Buckley, and C. M. Cates, "Laser thrombolysis in acute myocardial infarction," *Lasers Surg. Med.*, vol. (Suppl5), p. 13, 1993.

[55] K. W. Gregory and R. R. Anderson, "Liquid core light guide for laser angioplasty," *IEEE J. Quantum Electron.*, vol. 26, pp. 2289–2296, 1990.

[56] L. Deckelbaum, "Coronary laser angioplasty," *Lasers Surg. Med.*, vol. 14, pp. 101–110, 1994. Review.

[57] E. A. Chasteney, P. S. Ravichandran, D. Tuke-Bahlman, A. Shearin, and K. W. Gregory, "Rapid thrombolysis in experimental coronary artery bypass grafts," *J. Am. Coll. Cardiol.*, vol. Special issue, p. 348, 1995. Abstract.

[58] C. Korninger and D. Collen, "Studies on the specific fibrinolytic effect of extrinsic (tissue-type) plasminogen activator in human blood and in animal species *in vitro*," *Thromb Haemost*, vol. 46, pp. 561–565, 1981.

[59] M. A. L. Laskey, E. Deutsch, E. Barnathan, and W. K. Laskey, "Influence of heparin therapy on percutaneous transluminal coronary angioplasty: outcome of unstable angina pectoris," *Am J Cardiol*, vol. 65, pp. 1425–1429, 1990.

[60] A. T. Chapekis, B. S. George, and R. J. candela, "Rapid thrombus dissolution by continuous infusion of urokinase through an intracoronary perfusion wire prior to and following PTCA: results in natice coronaries and patent saphenous vein grafts," *Cathet. Cardiovasc. Diagn.*, vol. 23, pp. 89–92, 1991.

[61] P. T. Vaitkus, H. C. Herrmann, and W. Laskey, "Management and immediate outcome of patients with intracoronary thrombus during percutaneous transluminal coronary angioplasty," *Am Heart J.*, vol. 124, pp. 1–8, 1992.

[62] H. Shangguan, T. W. Haw, K. W. Gregory, and L. W. Casperson, "Noval cylindrical illuminator tip for ultraviolet light delivery," in *SPIE Proceedings of Diagnostics and Therapeutic Cardiovascular Interventions III* (G. S. Abela, ed.), vol. 1878, pp. 167–182, 1993.

[63] H. Wolinsky and M. B. Taubman, "Local delivery to the arterial wall: Pharmacologic and molecular approaches," in *Coronary Balloon Angioplasty* (R. E. Vlietstra, ed.), pp. 156–186, Boston: Blackwell Scientific Inc., 1994.

[64] A. M. Lincoff, E. J.Topol, A. Frieser, and S. G. Ellis, "Local drug delivery for prevention of restenosis," *Circulation*, vol. 90, pp. 2070–2084, 1994.

[65] B. Goldman, H. Blanke, and H. Wolinsky, "Influence of pressure on permeability of normal and diseased muscular arteries to horeseradish peroxidase," *Atherosclerosis*, vol. 65, pp. 215–225, 1987.

[66] C. R. Lambert, J. E. Leone, and S. M. Rowland, "Local drug delivery catheters: functional comparison of porous and microporous designs," *Cor Art Dis.*, vol. 4, pp. 469–475, 1993.

[67] E. C. Santoian, M. B. Gravanis, K. Anderberg, N. A. Scott, S. P. Karas, J. E. Schneider, and S. B. King, "Use of a porous infusion balloon in swine coronary arteries: low pressure minimizes arterial damage," *Circulation*, vol. 84, p. 591, 1991.

[68] M. A. Azrin, J. F. Mitchel, L. M. Bow, T. V. Albeerghini, R. P. D. B. Fram, D. Waters, and R. G. McKay, "Effect of local delivery of heparin on

platelet deposition during *in vivo* balloon angioplasty using hydrogel-coated balloons," *Circulation*, vol. 88 (suppl I), pp. I–310, 1993.

[69] W. C. Groh, B. P. Kurnik, W. H. Matthai, and W. J. Untereker, "Initial experience with an intracoronary flow support device providing localized drug infusion: The Scimed Dispatch Catheter," *Cathet Cardiovasc Diagn.*, vol. 36, pp. 67–73, 1995.

[70] J. F. Mitchel, D. B. Fram, F. D. P. II, R. Foster, J. A. Hirst, M. A. Azrin, L. M. Bow, A. M. Eldin, D. D. Waters, and R. G. McKay, "Enhanced intracoronary thrombolysis with urokinase using a novel, local drug delivery system: *in vitro*, *in vivo*, and clinical studies," *Circulation*, vol. 91, pp. 785–793, 1995.

[71] R. J. Siegel, M. Ariani, J. S. Foresster, Z. Hashemi, E. DeCastro, T. A. Don-Michael, and M. C. Fishbein, "Cardiovascular applications of therapeutic ultrasound," *J Invasive Cardiol*, vol. 1, pp. 219–229, 1989.

[72] U. Rosenschein, L. A. Rozenszajn, L. Kraus, C. C. Marboe, J. F. Watkins, E. A. Rose, D. Davia, P. J. Cannon, and J. S. Weinstein, "Ultrasonic angioplasty in totally occluded peripheral arteries: itnitial clinical, histological, and angiographic results," *Circulation*, vol. 83, pp. 1976–1986, 1991.

[73] C. G. Lauer, R. Burge, D. B. Tang, B. G. Bass, E. R. Gomez, and B. M. Alving, "Effect of ultrasound on tissue-type plasminogen activator-induced thrombolysis," *Circulation*, vol. 86, pp. 1257–1264, 1992.

[74] D. Harpaz, X. Chen, C. W. Francis, V. J. Marder, and R. S. Meltzer, "Ultrasound enhancement of thrombolysis and reperfusion *in vitro*," *J. Am. Coll. Cardiol.*, vol. 21, pp. 1507–1511, 1993.

[75] C. W. Francis, A. Blinc, S. Lee, and C. Cox, "Ultrasound accelerates transport of recombinant tissue plasminogen activator into clots," *Ultrasound in Medicine & Biology*, vol. 21, pp. 419–424, 1995.

[76] T. G. van Leeuwen, M. J. van der Veen, R. M. Verdaasdonk, and C. Borst, "Noncontact tissuue ablation by holmium:YSGG laser pulses in blood," *Lasers Surg. Med.*, vol. 11, pp. 26–27, 1991.

[77] T. J. Flotte, S. Lee, H. Zhang, D. MacAuliffe, T. Douki, and A. Doukas, "Laser-induce stress transients: Applications for molecular delivery," in *SPIE Proceedings of Laser-Tissue Interaction VI* (e. Jacques, S. L., ed.), vol. 2391, pp. 202–207, 1995.

[78] A. J. Welch, M. Motamedi, S. Rastegar, G. L. LeCarpentier, and D. Jansen, "Laser thermal ablation," *Photochem. Photobiol.*, vol. 53, pp. 815–823, 1991.

[79] H. F. Bowman, E. G. Cravalho, and M. Woods, "Theory, measurement and application of thermal properties of biomaterials," *Annual Review of Biophysics and Bioengineering*, vol. 4, pp. 43–80, 1975.

[80] E. D. Jansen, *Pulsed laser ablation of biological tissue: Influence of laser parameters and tissue properties on thermal and mechanical damage.* PhD thesis, University of Texas at Austin, 1994.

[81] J. T. Walsh and T. F. Deutsch, "Measurement of Er:YAG laser ablation plume dynamics," *Appl. Phys. B*, vol. 52, pp. 217–224, 1991.

[82] A. Vogel, P. Schweiger, A. Frieser, M. N. Asiyo, and R. Birngruber, "Intraocular Nd:YAG laser surgery: Light-tissue interaction, damage range, and reduction of collateral effects," *IEEE J. Quantum Electron.*, vol. 26, pp. 2240–2259, 1990.

[83] T. G. van Leeuwen, E. D. Jansen, M. Motamedi, C. Brost, and A. J. Welch, "Excimer laser ablation of soft tissue: a study of the content of rapidly expanding and collapsing bubbles," *IEEE J. Quantum Electron.*, vol. 30, pp. 1339–1345, 1994.

[84] E. D. Jansen, T. G. van Leeuwen, M. Motamedi, C. Brost, and A. J. Welch, "Partial vaporization model for pulsed mid-infrared laser ablation of water," *J. Appl. Phys*, vol. 78, pp. 564–571, 1995.

[85] J. T. Walsh Jr. and T. F. Deutsch, "Pulsed CO_2 laser ablation of tissue: Effect of mechanical properties," *IEEE Trans. Biomed. Eng.*, vol. 36, pp. 1195–1201, 1989.

[86] G. Paltaulf, M. Frenz, and H. Schmidt-Kloiber, "Influence of acoustic diffraction on laser-induced stress wave effects in absorbing media," in *Laser-Tissue Interaction II* (S. L. Jacques, ed.), vol. 2681, pp. 334–342, SPIE, 1996.

[87] R. de la Torre, "Intravascular laser induced cavitation: A study of the mechanics with possible detrimental and beneficial effects," Master's thesis, Harvard–M. I. T. Division of Health Sciences and Technology, Cambridge, MA, 1993.

[88] T. G. van Leeuwen, J. H. Meertens, E. Velema, M. J. Post, and C. Brost, "Intraluminal vapor bubble induced by excimer laser pulse causes microsecond arterial dilation and invagination leading to extensive wall damage in the rabbit," *Circulation*, vol. 87, pp. 1258–1263, 1993.

[89] A. Vogel, R. Engelhardt, U. Behnle, and U. Parlitz, "Minimization of cavitation effects in pulsed laser ablation - illustrated on laser angioplasty," *Appl. Phys. B*, vol. 62, pp. 173–182, 1996.

[90] T. G. van Leeuwen, E. D. Jansen, A. J. Welch, and C. Borst, "Excimer laser induced bubble: Dimensions, theory, and implications for laser angioplasty," *Lasers Surg. Med.*, vol. 18, pp. 381–390, 1996.

[91] E. D. Jansen, T. Asshauer, M. Frenze, M. Motamedi, G. Delacretaz, and A. J. Welch, "Effect of pulse duration on bubble formation and laser-induced pressure waves during holmium laser ablation," *Lasers Surg. Med.*, vol. 18, pp. 278–293, 1996.

[92] F. R. Young, *Cavitation*. McGraw Hill, 1989.

[93] Y. Tomita and A. Shima, "Mechanisms of impulsive pressure generation and damge pit formation by bubble collapse," *J. Fluid Mech.*, vol. 169, pp. 535–564, 1986.

[94] R. G. Brewer and K. E. Rieckhoff, "Stimulated brillouin scattering in liquids," *Phys. Rev. Lett.*, vol. 13, pp. 334–336, 1964.

[95] E. F. Craome, C. E. Moeller, and N. A. Clark, "Intense ruby-laser-induced acoustic impulse in liquids," *J. Acous. Soc. Am.*, vol. 40, pp. 1462–1466, 1966.

[96] W. Lauterborn, "Kavitation durch laserlicht," *Acustica*, vol. 31, pp. 51–78, 1974.

[97] A. Vogel, S. Busch, K. Jungnickel, and R. Birngruber, "Mechanisms of intraocular photodisruption with picosecond and nanosecond laser pulses," *Lasers Surg. Med.*, vol. 15, pp. 32–43, 1994.

[98] K. Rink, G. Delacrétaz, and R. P. Salathé, "Fragmentation process of current laser lithotriptors," *Lasers Surg. Med.*, vol. 16, pp. 134–146, 1995.

[99] A. Vogel, W. Lauterborn, and R. Timm, "Optical and acoustic investigations of the dynamics of laser-produced cavitation bubbles near a solid boundary," *J. Fluid Mech.*, vol. 206, pp. 299–238, 1989.

[100] S. L. Jacques and G. Gofstein, "Laser-flash photographic studies of Er:YAG laser ablation of water," in *SPIE Proceedings of Laser-Tissue Interaction II* (S. L. Jacques, ed.), vol. 1427, pp. 63–67, 1991.

[101] A. S. Silenok, R. Steiner, M. Fischer, K. Stock, R. Hibst, and V. I. Konov, "Bubble formation in light absorbing liquid," in *SPIE Proceedings of Laser-Tissue Interaction III* (S. L. Jacques, ed.), vol. 1646, pp. 322–337, 1992.

[102] A. Vogel, W. Hentschel, J. Holzfuss, and W. Lauterborn, "Cavitation bubble dynamics and acoustic transient generation in ocular surgery with pulsed neodymium:YAG lasers," *Ophthalmology*, vol. 93, pp. 1259–1269, 1986.

[103] J. T. Walsh, T. J. Flotte, and T. F. Deutsch, "Er:YAG laser ablation of tissue: Effect of pulse duration and tissue type on thermal damage," *Lasers Surg. Med.*, vol. 9, pp. 314–326, 1989.

[104] A. G. Doukas and T. J. Flotte, "Physical characteristics and biomedical effects of laser-induced stress waves," *Ultrasound in Medi. & Biol.*, vol. 22, pp. 151–164, 1996.

[105] J. M. Krauss and C. A. Pauliafito, "Lasers in ophthamology," *Laser Med. Surg.*, vol. 17, pp. 102–159, 1995.

[106] F. Litvack, "Excimer laser coronary angioplasty," in *Interventional Cardiology* (E. J. Topol, ed.), vol. 2, ch. 5, pp. 841–866, W. B. Saunders Company, 1994.

[107] O. Topaz, "Holmium:YAG coronary angioplasty: the multicenter registry," in *Interventional Cardiology* (E. J. Topol, ed.), vol. 2, ch. 5, pp. 867–891, W. B. Saunders Company, 1994.

[108] E. S. L. Beale, "Latent heat data for hydrocarbons, petroleum producsts, and miscellaneous substances," in *The science of petroleum* (A. E. Dunstan, A. W. Nash, B. T. Brooks, and S. H. Tizard, eds.), vol. 2, ch. 20, pp. 1257–1260, Oxford University Press, 1938.

[109] R. de la Torre and K. W. Gregory, "Cavitation bubbles and acoustic transients may produce dissections during laser angioplasty," *J. Am. Coll. Cardiol.*, vol. 19A, p. 48, 1992.

[110] Lord Rayleigh, "On the pressure developed during the collapse of a spherical cavity," *Phil. Mag.*, vol. 34, pp. 94–98, 1917.

[111] M. Oberhoff, S. Hassenstein, H. Hank, D. Y. Xie, E. Blessing, A. Baumbach, S. Hanke, K. K. Betz, and K. R. Karsch, "Smooth excimer laser coronary angioplasty (SELCA)-initial experimental results," *Circulation*, vol. 86(I), p. 800, 1992.

[112] F. Litvack, N. L. Eigler, and J. R. Margolis, "Percutaneous excimer laser coronary angioplasty," *Am. J. Cardiol.*, vol. 66, pp. 1027–1032, 1990.

[113] S. Kurada, G. W. Rankin, and K. Sridhar, "Particle-imaging techniques for quantitative flow visualization: a review," *Optics & Laser Technology*, vol. 25, pp. 219–233, 1993.

[114] W. Lauterborn and H. Bolle, "Experimental investigations of cavitation-bubble collapse in the neighborhood of a solid boundary," *J. Fluid Mech.*, vol. 72, pp. 391–399, 1975.

[115] W. Lauterborn and W. Hentschel, "Cavitation bubble dynamics studied by high speed photography and holography: part one," *Ultrasonics*, vol. 23, pp. 260–268, 1985.

[116] A. A. Oraevsky, R. Esenaliev, S. L. Jacques, and F. K. Tittel, "Laser flash photography of cold cavitation-driven ablation in tissues," in *Proceedings of Laser-Tissue Interaction VI* (S. L. Jacques, ed.), vol. 2391, pp. 300–307, 1995.

[117] A. Vogel and W. Lauterborn, "Time-resolved particle image velocimetry used in the investigation of cavitation bubble dyanmics," *Appl. Opt.*, vol. 9, pp. 1869–1876, 1988.

[118] D. A. Dichek, R. F. Neville, J. A. Zwiebel, S. M. Freeman, M. B. Leon, and W. F. Anderson, "Seeding of intravescular stents with genetically engineered endothelial cells," *Circulation*, vol. 80, pp. 1347–1353, 1989.

[119] E. G. Nabel, G. Plautz, and G. J. Nable, "Site-secific gene expression *in vivo* by direct gene transfer into the arterial wall," *Science*, vol. 249, pp. 1285–1288, 1990.

[120] H. Lin, M. S. Parmacek, G. Morle, S. Bolling, and J. M. Leiden, "Expression of recombination genes in myocardium *in vivo* after direct injection of DNA," *Circulation*, vol. 82, pp. 2217–2221, 1990.

[121] A. Fernández-Ortiz, B. J. Meyer, A. Mailhac, E. Falk, L. Badimon, J. T. Fallon, V. Fuster, J. H. Chesebro, and J. J. Badimon, "A new approach for local intravascular drug delivery: iontophoretic balloon," *Circulation*, vol. 89, pp. 1518–1522, 1994.

[122] R. C. Zeimer, B. Khoobehi, and R. L. Magin, "A potential method for local drug and dye delivery in the ocular vasculature," *Investigative Ophthalmology & Visual Sicience*, vol. 29, pp. 1179–1183, 1988.

[123] G. K. Batchelor, *Introduction to fluid dynamics*. Cambridge University Press, 1980.

[124] T. G. van Leeuwen, L. van Erven, J. H. Meertens, M. J. Post, and C. Borst, "Vapor bubble expansion and implosion: the origin of 'mille feuilles'," in *SPIE Proceedings of Diagnostic and Therapeutic Cardiovascular Interventions III* (e. Abela, G. S., ed.), vol. 1878, pp. 2–12, 1993.

[125] M. J. Girsky, K. W. Gregory, A. S. Shearin, and S. A. Prahl, "Photoacoustic drug delivery to arterial thrombus — a new method for local drug delivery," *Circulation*, 1996 (abstract).

[126] K. Kandarpa, P. A. Drinker, S. J. Singer, and D. Caramore, "Forceful pulsatile local infusion of enzyme accelerates thrombolysis: *in vivo* evaluation of new delivery system," *Radiology*, vol. 168, pp. 739–744, 1988.

[127] R. Srinivasan, K. G. Casey, and J. D. Haller, "Subnanosecond probing of the ablation of soft plaque from arterial wall by 308 nm laser pulses delivered through a fiber," *IEEE J. Quantum Electron.*, vol. 26, pp. 2279–2283, 1990.

[128] G. H. M. Gijsbers, R. L. H. Sprangers, M. Keijzer, J. M. T. De Bakker, T. G. van Leeuwen, R. M. Verdaasdonk, C. Borst, and M. J. C. van Gemert, "Some laser-tissue interactions in 308 nm excimer laser coronary angioplasty," *J. Interven. Cardiol.*, vol. 3, pp. 231–241, 1990.

[129] T. Tomaru, H. J. Geschwind, G. Boussignac, F. Lange, and S. J. Tahk, "Comparison of ablation efficiency of excimer, pulsed dye, and holmium-YAG lasers relevant to shock waves," *Am. Heart J.*, vol. 123, pp. 886–895, 1992.

[130] M. Buchelt, T. Papaioannou, M. Fishbein, W. Peters, C. Beeder, and W. S. Grundfest, "Excimer laser ablation of fibrocartilage: An *in vitro* and *in vivo* study," *Laser Surg. Med.*, vol. 11, pp. 271–279, 1991.

[131] G. H. M. Gijsbers, D. G. van den Brocke, R. L. H. Sprangers, and M. J. C. van Gemert, "Effect of force ablation depth for a XeCl excimer laser beam delivered by an optical fiber in contact with arterial tissue in saline," *Laser Surg. Med.*, vol. 12, pp. 576–584, 1992.

[132] F. Litvack, W. S. Grundfest, T. Goldenberg, J. Laudenslager, T. Pacala, J. Segalowitz, and J. Forrester, "Pulsed laser angioplasty: Wavelength

power and energy dependencies relevant to clinical application," *Lasers Surg. Med.*, vol. 8, pp. 60–65, 1988.

[133] R. S. Taylor, L. A. J. Higginson, and K. E. Leopold, "Dependence of the XeCl laser cut rate of plaque on the degree of calcification, laser fluence, and optical pulse duration," *Laser Surg. Med.*, vol. 10, pp. 414–419, 1990.

[134] E. H. Schallen, C. C. Awh, and E. de Juan, Jr., "Rate-dependent nonlinear photoablation of ocular tissue at 308 nm," *Lasers Surg. Med.*, vol. 15, pp. 99–106, 1994.

[135] Y. C. Fung, *Biomechanics- mechanical properties of living tissues.* Berlin: Springer, 2nd ed., 1993.

[136] U. S. Sathyam, A. Shearin, E. A. Chasteney, and S. A. Prahl, "Threshold and ablation efficiency studies of microsecond ablation of gelatin under water," *Lasers Surg. Med.*, vol. 19, 1996 (in press).

[137] R. S. Dingus, "Laser-induced contained-vaporization in tissue," in *SPIE Proceedings of Laser-Tissue Interaction III* (S. L. Jacques, ed.), vol. 1646, pp. 266–274, 1992.

[138] A. Vogel and W. Lauterborn, "Acoustic transient generation by laser-produced cavitation bubbles near solid boundaries," *J. Acoust. Soc. Am.*, vol. 84, pp. 719–731, 1988.

[139] W. J. Snuder, W. Q. Shi, S. G. Vari, and W. S. Grundfest, "Comparative study of pulsed Ho:YAG versus tm:yag: impulse induced presure in porcine aorta," in *Laser-Tissue Interaction IV* (S. L. Jacques, ed.), vol. 1882, pp. 153–161, SPIE, 1993.